

**Hochschule für Angewandte Wissenschaften Hamburg**

**Fakultät Life Sciences**

Evaluation of Flow Conditions at a Wind Turbine Spinner via  
CFD-Simulation

Master Thesis

Renewable Energy Systems – Environmental and Process Engineering

submitted by

**Raulf, Luka**

Matr. No: XXXXXXXXXX

Hamburg

27.12.2017

Advisor: Prof. Dr.-Ing. Rainer Stank (HAW Hamburg)

Advisor: Dr.-Ing. Harald Hohlen (ROMO Wind Deutschland GmbH)



# Table of Contents

<b>Table of Contents .....</b>	<b>I</b>
<b>Figures and Tables .....</b>	<b>III</b>
<b>Figures:.....</b>	<b>III</b>
<b>Tables:.....</b>	<b>V</b>
<b>Abbreviations, Symbols and Constants.....</b>	<b>VI</b>
<b>1. Introduction.....</b>	<b>1</b>
<b>1.1 Motivation for Flow Analysis over the Spinner .....</b>	<b>1</b>
<b>1.2 Thesis Objective .....</b>	<b>2</b>
<b>1.3 Wind Turbine and iSpin Sensor .....</b>	<b>3</b>
<b>1.3.1 Description of Wind Turbine and Rotor Blades.....</b>	<b>3</b>
<b>1.3.2 Description of iSpin Sensors.....</b>	<b>5</b>
<b>2. Modelling of the Geometry and Simulation Setup.....</b>	<b>8</b>
<b>2.1 Creating the Spinner Geometry.....</b>	<b>8</b>
<b>2.2 Modelling of Wind Turbine Rotor Blades .....</b>	<b>14</b>
<b>2.3 iSpin Sensor Geometry .....</b>	<b>16</b>
<b>2.4 Meshing of the Geometry.....</b>	<b>17</b>
<b>2.5 Simulation Models and Boundary Conditions.....</b>	<b>20</b>
<b>3. Simulation Strategies.....</b>	<b>24</b>
<b>3.1 Conducted Simulations.....</b>	<b>24</b>
<b>3.3 Macroinstructions for Current and Future Cases .....</b>	<b>25</b>
<b>4. Evaluation of Experimental and Measured Data .....</b>	<b>26</b>
<b>4.1 Met Mast Data .....</b>	<b>26</b>
<b>4.1.1 Verification of the Wind Profile Exponent Alpha .....</b>	<b>28</b>
<b>4.2 Plausibility of the Experimental Data.....</b>	<b>29</b>

4.2.1 Power Generation of the Simulated Wind Turbine .....	29
4.2.2 Angle of Attack and Pressure Coefficient over the Blade.....	30
4.2.3 Mass Flow Behaviour in Front of the Wind Turbine.....	33
<b>5. Discussion.....</b>	<b>36</b>
<b>5.1 Velocity Decrease and Air Flow Behaviour.....</b>	<b>36</b>
5.1.1 Velocity Decrease .....	36
5.1.2 Air Flow Behaviour.....	41
<b>5.2 Test and Reference Simulation with the WT from the DOWEC Study Project.....</b>	<b>48</b>
<b>5.3 Logarithmic Wind Profile .....</b>	<b>50</b>
5.3.1 k-Factor for Logarithmic Wind Profile .....	50
<b>5.4 Block Profile .....</b>	<b>52</b>
5.4.1 k-Factor for Block Profile .....	53
<b>5.5 Logarithmic Wind Profile with 5 Degree Inclination .....</b>	<b>54</b>
5.5.1 k-Factor for Logarithmic Wind Profile with 5 Degree Inclination .....	55
<b>5.6 Influence of Blades and Spinner on the k-Factor .....</b>	<b>56</b>
<b>5.7 k-Factor Estimate for all Cases.....</b>	<b>57</b>
<b>6. Conclusion .....</b>	<b>59</b>
<b>7. Outlook.....</b>	<b>62</b>
<b>8. References .....</b>	<b>64</b>
<b>9. Appendix.....</b>	<b>66</b>
9.1 MATLAB script for the Edge Transformation .....	66
9.2 MATLAB script for the Point Cloud Transformation .....	68
9.3 Ansys ICEM Global Mesh Setup .....	70
9.4 Global Mesh Parameters .....	71
9.5 iSpin Dimensions for the Technical Drawing .....	72
<b>Statutory Declaration.....</b>	<b>74</b>

# Figures and Tables

## Figures:

FIGURE 1: FRONT VIEW GE 2.5-120 CREATED IN AUTO DESK FUSION 360 [1] .....	3
FIGURE 2: SIDE VIEW GE 2.5-120 NACELLE AND HUB SECTION CREATED IN AUTO DESK FUSION 360 [1] .....	4
FIGURE 3: POWER CURVE GE 2.5-120 [2] .....	4
FIGURE 4: ANEMOMETRY-TIME OF FLIGHT THEORY [7] .....	5
FIGURE 5: LIDAR VIEW DISPLAY OF POINT CLOUD CREATED FROM XYZ-DATA [12] .....	8
FIGURE 6: EXCERPT FROM DEVELOPED MATLAB PICTURE EDGE TRANSFORMATION [14] .....	9
FIGURE 7: GEOMETRIES CREATED FROM PICTURE EDGE TRANSFORMATION [15] .....	10
FIGURE 8: EXCERPT FROM XYZ-DATA AS PROVIDED BY COPTERPROJECTS [12] .....	10
FIGURE 9: EXCERPT FROM DEVELOPED MATLAB SCRIPT POINT CLOUD TRANSFORMATION [14] .....	11
FIGURE 10: TRANSFORMED AND NORMALIZED POINT CLOUD FIGURES CREATED FROM MATLAB SCRIPT [14] .....	12
FIGURE 11: MATLAB SCRIPT POINT CLOUD WITH THE MODELLED GEOMETRY [15] .....	12
FIGURE 12: FRONT, SIDE AND TOP VIEW OF CAD GEOMETRY CREATED FROM MATLAB POINT CLOUD [15] .....	13
FIGURE 13: SURFACE RIPPLES IN CREATED SPINNER SURFACE [15] .....	13
FIGURE 14: FRONT, SIDE AND TOP VIEW DRONE PICTURES AS PROVIDED BY COPTERPROJECTS [12] .....	14
FIGURE 15: REDUCTION OF CREATED DOWEC BLADE LENGTH BY A FACTOR OF 0.9302 [15] .....	15
FIGURE 16: XY-DIMENSIONAL REDUCTION OF CREATED DOWEC BLADES BY A FACTOR OF 0.7064 [15] .....	15
FIGURE 17: ISPIN GEOMETRY RECREATED FROM TECHNICAL DRAWING AND CALLIPER MEASUREMENTS [15] .....	16
FIGURE 18: MESH QUALITY OF CREATED SPINNER AND ROTOR BLADE GEOMETRY [15] .....	19
FIGURE 19: MESH QUALITY OF CREATED SURROUNDING GEOMETRY [15] .....	19
FIGURE 20: LOGARITHMIC WIND PROFILE FOR DIFFERENT TERRAINS [21, P. 3] .....	21
FIGURE 21: POSITION OF MET MAST AND WIND TURBINES AT OFFENBACH AN DER QUEICH FROM INSTALLATION REPORT [24] .....	26
FIGURE 22: WIND SECTORS FOR WIND TURBINE AT OFFENBACH AN DER QUEICH [24] .....	27
FIGURE 23: CORRELATION OF ISPIN WIND SPEED TO MET MAST WIND SPEED FROM MET MAST DATA [25] .....	28
FIGURE 24: DISTRIBUTION OF A-VALUES FROM MET MAST DATA [25] .....	29

FIGURE 25: SEPARATION BUBBLE AT AIRFOIL DU30 FROM SIMULATION [26].....	30
FIGURE 26: PRESSURE COEFFICIENT $C_p$ AT AIRFOIL DU30 FROM SIMULATION [26].....	31
FIGURE 27: PRESSURE COEFFICIENT $C_p$ AT AIRFOIL DU30 FROM THE DOWEC 6 MW STUDY PROJECT [26] .....	31
FIGURE 28: WIND VECTOR AND RESULTING FORCES ON AIRFOIL [28] .....	32
FIGURE 29: POSITION OF THE ISPIN SENSORS – VIEW AT YZ PLANE FROM SIMULATION [26].....	33
FIGURE 30: POSITION OF THE ISPIN SENSORS SEEN FROM XY-PLANE FROM SIMULATION [26] .....	33
FIGURE 31: VELOCITY IN STATIONARY FRAME AT ISPIN POSITION FROM SIMULATION [26] .....	33
FIGURE 32: VELOCITY OVER SPINNER SURFACE IN STATIONARY FRAME U FROM SIMULATION [26] .....	34
FIGURE 33: VELOCITY IN STATIONARY FRAME U OVER CYLINDRICAL SURFACE AT SPINNER FROM SIMULATION [26].....	35
FIGURE 34: PRESSURE OVER CYLINDRICAL SURFACE AT SPINNER FROM SIMULATION [26] .....	35
FIGURE 35: ELONGATED MEASURING LINE FOR HORIZONTAL AXIS AND 4 DEGREE TILTED ROTATIONAL AXIS FROM POST-PROCESSING [26].....	36
FIGURE 36: VELOCITY DECREASE ALONG ELONGATED ISPIN POLY LINE FROM POST-PROCESSING FOR THE LOGARITHMIC WIND PROFILE 12 M/S [26] .....	37
FIGURE 37: VELOCITY DECREASE ALONG ELONGATED ISPIN POLY LINE FROM POST-PROCESSING FOR THE LOGARITHMIC WIND PROFILE 16 M/S [26] .....	38
FIGURE 38: VELOCITY DECREASE ALONG ELONGATED ISPIN POLY LINE FROM POST-PROCESSING FOR THE LOGARITHMIC WIND PROFILE 4 M/S [26].....	39
FIGURE 39: VELOCITY DECREASE CHECK DISKS FROM POST PROCESSING [26].....	40
FIGURE 40: DIAGRAM OF VELOCITY DROP CHECK DISKS [25] .....	40
FIGURE 41: VELOCITY IN STATIONARY FRAME AT ISPIN POSITION FROM SIMULATION WITH ROTATED BLADE [25].....	42
FIGURE 42: ROTATED AND ORIGINAL SPINNER COMPARISON OF THE SENSOR PATH SURFACE [26].....	42
FIGURE 43: VELOCITY IN STATIONARY FRAME U OVER ROTATION ANGLE FROM SIMULATION [25] .....	43
FIGURE 44: 10 HZ VELOCITY MEASUREMENT FOR INDIVIDUAL ISPIN SENSORS OVER ROTATION ANGLE AT WONNEGAU [25] .....	45
FIGURE 45: 10 MINUTE AVERAGE VELOCITY MEASUREMENT FOR INDIVIDUAL ISPIN SENSORS AT WONNEGAU [25].....	46
FIGURE 46: AVERAGE ISPIN VELOCITY MEASUREMENT OVER ROTATION ANGLE AT WONNEGAU [25].....	47
FIGURE 47: VELOCITY OVER SPINNER SURFACE IN STATIONARY FRAME U FROM SIMULATION FOR THE DOWEC WT [25].	48
FIGURE 48: VELOCITY DECREASE ALONG ELONGATED ISPIN POLY LINE FROM POST PROCESSING FOR WIND PROFILE 12 M/S DOWEC WT [26].....	49

FIGURE 49: VELOCITY IN STATIONARY FRAME U OVER ANGLE FROM SIMULATION FOR THE DOWEC WT [26] .....	49
FIGURE 50: WIND PROFILE INLET VECTOR FROM SIMULATION [26] .....	50
FIGURE 51: LOGARITHMIC WIND PROFILE AT INLET FROM SIMULATION [26] .....	50
FIGURE 52: BLOCK PROFILE INLET VECTOR WITH INCLINATION ANGLE $\phi=0^\circ$ FROM SIMULATION [26] .....	52
FIGURE 53: BLOCK PROFILE AT INLET FROM SIMULATION [26] .....	52
FIGURE 54: WIND PROFILE INLET VECTOR WITH INCLINATION ANGLE $\phi=5^\circ$ FROM SIMULATION [25] .....	54
FIGURE 55: LOGARITHMIC WIND PROFILE WITH INCLINATION ANGLE AT INLET FROM SIMULATION [25] .....	54
FIGURE 56: ISO VIEW OF THE WT WITH CYLINDRICAL BLADES [26] .....	56
FIGURE 57: K-FACTOR FROM MET MAST DATA AND K-FACTOR ESTIMATE FROM SIMULATIONS [25] .....	58

## Tables:

TABLE 1: INITIAL SIMULATION CONDITIONS FOR WIND TURBINE GEOMETRY .....	2
TABLE 2: LM 58.7 BLADE SPECIFICATIONS [3] .....	5
TABLE 3: WIND PROFILE EQUATION TABLE .....	23
TABLE 4: 10 Hz DATA FROM iSPIN MEASUREMENTS AT WONNEGAU [25] .....	44
TABLE 5: K-FACTORS FOR LOGARITHMIC WIND PROFILE [25] .....	51
TABLE 6: K-FACTORS FOR BLOCK PROFILE [25] .....	53
TABLE 7: K-FACTORS FOR LOGARITHMIC WIND PROFILE WITH 5 DEGREE INCLINATION ANGLE [25] .....	55
TABLE 8: INFLUENCE OF BLADE SHAPE ON THE K-FACTOR [25] .....	57
TABLE 9: K-FACTOR ESTIMATION OF ALL WIND PROFILES [25] .....	57

## Abbreviations, Symbols and Constants

WT	Wind turbine
met mast	Measurement tower equipped with meteorological instruments
CAD	Computer aided design
CFD	Computational fluid dynamics
macro	Macroinstructions
AoA	Angle of attack
rpm	Revolutions per minute
x, y, z	References to the axis in a coordinate frame
u, v, w	References to velocity components in respect to the coordinate frame
DOWEC	Dutch Offshore Wind Energy Converter
SCADA	Supervisory control and data acquisition
atm	Atmosphere, used as a measure of pressure
$\alpha$	Hellmann exponent
$\kappa$	Von-Karman constant
$\Psi$	Stability corrections factor
$L^*$	Monin-Obukhov length
$\varphi$	Inclination angle

# 1. Introduction

## 1.1 Motivation for Flow Analysis over the Spinner

Wind velocity is the most influential property when determining the power of the wind. Therefore, knowing the wind's velocity is crucial in operating a wind turbine. However, the classic concept of measuring wind velocities via cup anemometers or sonic anemometers bears some disadvantages: Since anemometers are traditionally installed behind the rotor blades they experience, and thus record a lot of turbulences. Therefore, the anemometers cannot measure wind speeds and directions precisely. The sonic iSpin technology, which will be explained and evaluated in this thesis, is a relatively new approach to measuring wind speeds and wind directions for a wind turbine while reducing the influence of the turbulences introduced by the blades. For this, the iSpin sensors are installed on the nose of the spinner in front of the blades, thus reducing the blades' effect on the sensor's measurements. However, for each turbine type some calibration values, such as the  $k_1$  and the  $k_\alpha$ -value, have to be known to allow the sensors to measure the wind vector correctly. The  $k_1$ -value is needed to map the measured values from the iSpin sensor to the actual wind speed, while the  $k_\alpha$ -value measures the flow angle. Both will further be explained in this thesis, while the  $k_1$ -factor will also be determined during the thesis and further also be referred to as k-factor. To determine both  $k_\alpha$ - and  $k_1$ -factor, initial measurements must be made. Usually this is done with the help of a measurement mast (met mast) which is positioned in front of a turbine or wind park and which records meteorological data.

The calibration of the iSpin sensors and the determination of the  $k_\alpha$ -values is done during operation or while the turbine is stopped. Stopping the turbine for calibration, even though it could produce energy, will take time and will impact the energy production. Calibration during operation takes longer than calibration with a stopped turbine. Either way, time is invested and energy that could be generated is lost. Further, depending on the wind site, a met mast or Lidar, a system, which is used to measure wind speed with laser impulses, or a combination of both is required.

With the help of the increasing possibilities available through computational fluid dynamics (CFD) and continuously increasing processing power, which allow the investigation of increasingly complex problems, the lengthy and costly process of stopping the turbine during

operation or the erection of met masts can be made redundant, when simulating the wind turbine to determine the calibration factor instead and in turn save costs. Further, the CFD-simulations can be adapted to each existing or planned turbine type as well as wind sites to give indications for unforeseen issues or improvements on the design, such as optimizing the geometry to reduce turbulences.

## 1.2 Thesis Objective

In the course of this thesis the airflow over the spinner of a wind turbine by General Electric (GE) will be simulated and discussed. Special focus is put on the wind velocities simulated at the spinner anemometers (iSpin sensors) and on their simulated behaviour compared to actual data recorded from a met mast. The simulations will be run with three different inlet velocities – 4 m/s, 12 m/s, 16 m/s - as well as three different wind profiles: a block profile with unchanging velocity in respect to height and two logarithmic wind profiles with changing velocities in respect to height, one of which will feature a horizontal inclination of 5 degrees.

**Table 1: Initial Simulation Conditions for Wind Turbine Geometry**

4 m/s	Block Profile	Logarithmic Wind Profile	Logarithmic Wind Profile with Inclination
12 m/s	Block Profile	Logarithmic Wind Profile	Logarithmic Wind Profile with Inclination
16 m/s	Block Profile	Logarithmic Wind Profile	Logarithmic Wind Profile with Inclination

Since the original equipment manufacturers of wind turbines are usually unwilling to provide the computer assisted design (CAD) models of their turbine types, these models are not publicly available. Therefore, in the course of this thesis, the wind turbine's geometry has to be recreated based on a point cloud generated, via photogrammetry from pictures taken by a drone. The drone pictures and point cloud (XYZ-data) were provided by the Hamburg-based firm Copterproject UG. The CAD model created for this thesis must include the spinner and the blade roots as they are subject to the flow analysis. The nacelle and tower are of less importance to the evaluation of the flow over the spinner but should be included in the geometry nevertheless.

The CAD model should be close to the actual geometry of the wind turbine and will be used with the different wind profile cases listed in table 1, to show how the model behaves. To ensure comparability between the different simulations, a macroinstructions (macro) file must be prepared to provide the same simulation setup and post-processing results for each case.

The different cases for inlet velocities and wind profiles allow the estimation of the k-factor.

The k-factor based on the simulations is compared to the k-factor available for the two GE-turbines, which are installed at Offenbach an der Queich and Wonnegau. The k-factor is based on measurements from the met mast and was used for the turbine's calibration. Further, the influences of the blades and of the spinner geometry on the k-factor are investigated by replacing the modelled rotor blades by a cylindrical shape.

## 1.3 Wind Turbine and iSpin Sensor

### 1.3.1 Description of Wind Turbine and Rotor Blades

Two wind turbines have been recorded with a remote-controlled drone by Copterprojects, both of the turbine type General Electric GE 2.5-120 which will further be referred to only as 'wind turbine' (WT). One WT is located at Offenbach an der Queich, the other one at Wonnegau. The simulations run for this thesis are based on the models generated with the help of the drone pictures and the point cloud, which is created from the drone's recordings. While the XYZ-data provided by Copterproject only includes the turbine at Offenbach an der Queich, the pictures taken by the drone from Wonnegau are used in the creation of the nacelle, as the nacelle was only partly included in the XYZ-data. As both WTs are of the same build, the pictures from Wonnegau can be used as a reference to finish the geometry. The model created for this thesis is the WT shown in figures 1 and 2.

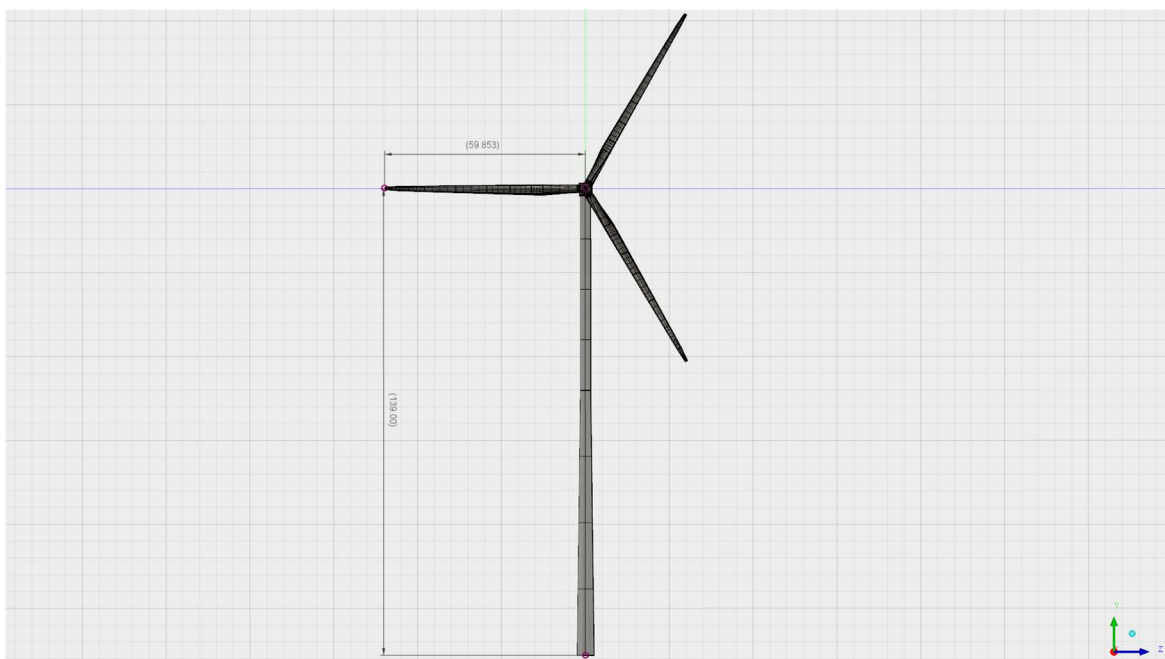


Figure 1: Front View GE 2.5-120 Created in Auto Desk Fusion 360 [1]

The WT has a hub height of 139 m and a rotor diameter of 120 m with which it can generate a nominal power of 2.5 MW at 12.5 revolutions per minute (rpm).

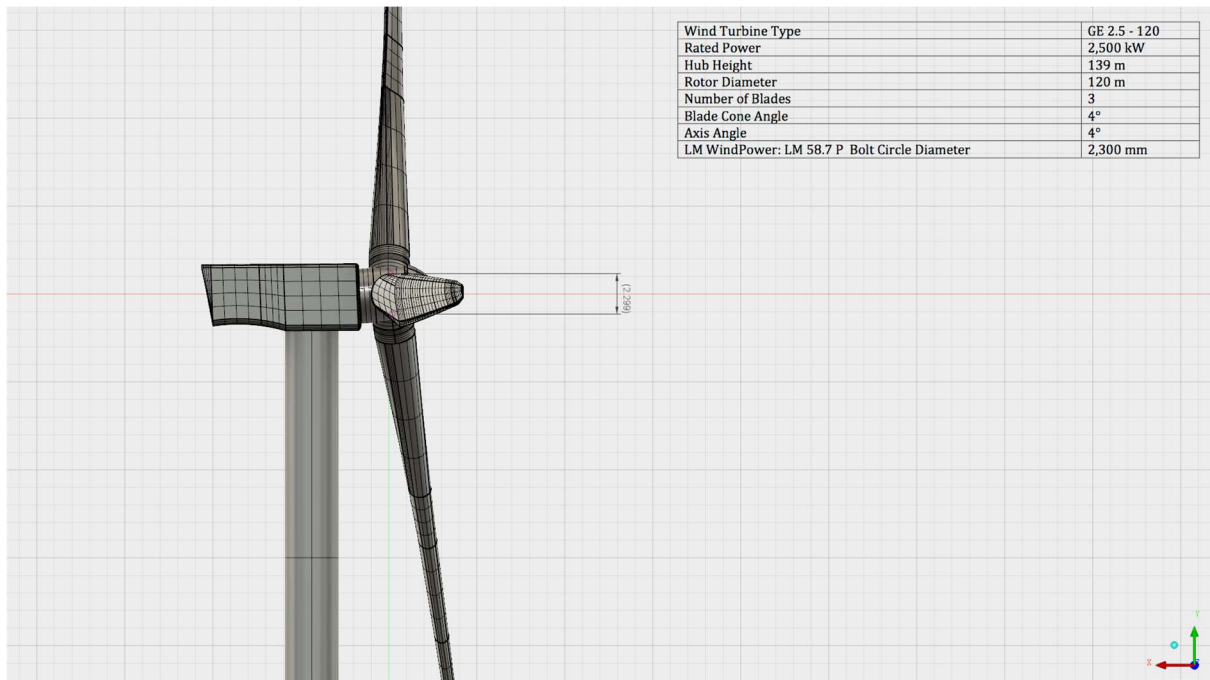


Figure 2: Side View GE 2.5-120 Nacelle and Hub Section Created in Auto Desk Fusion 360 [1]

The WT's cut-in wind speed is specified at 3 m/s, reaching its maximum power output at 11 m/s and the cut-out wind speed at 25 m/s as can be seen in the power curve in figure 3.

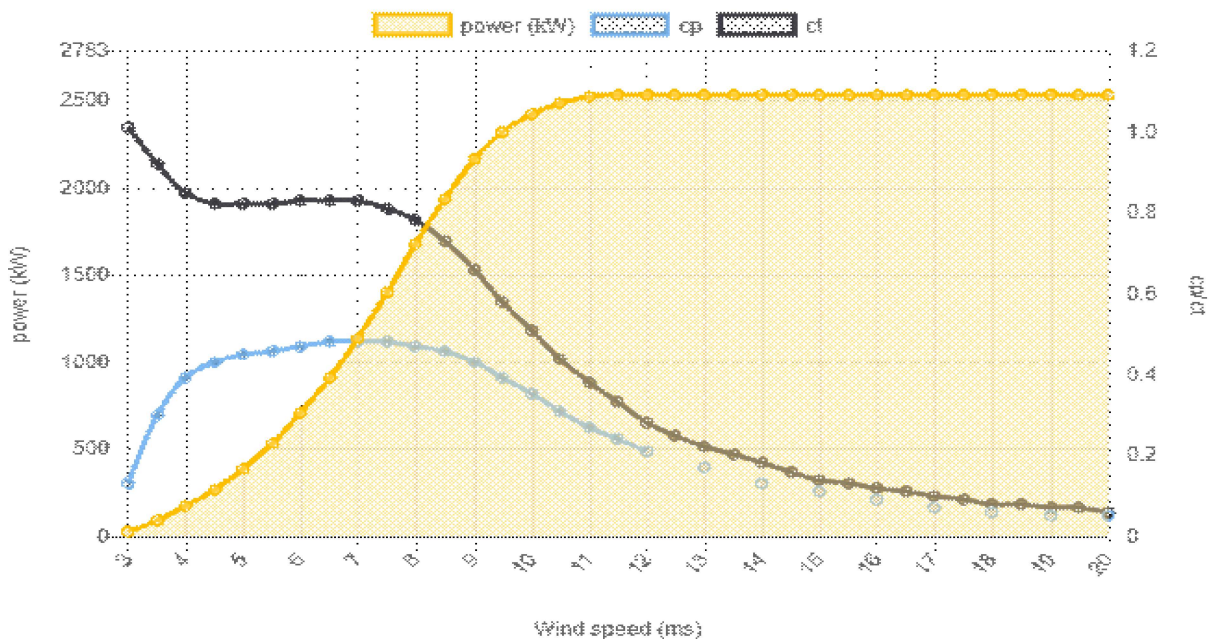


Figure 3: Power Curve GE 2.5-120 [2]

The rotor used on the WT is of the type LM 58.7 which is a blade manufactured by *LM WIND POWER BLADES*. The only data found on the LM 58.7 is the blade diameter of 120 m, as well as the bolt circle diameter, which is specified as 2300 mm as also shown in table 2.

**Table 2: LM 58.7 Blade Specifications [3]**

2.5 MW - 3.2 MW NOMINAL POWER OUTPUT							
BLADE TYPE	P	LM 48.8 P3	LM 48.8 P4	LM 53.2 P	LM 54.8 P	LM 58.7 P	LM 61.2 P
ROTOR (M)		100	100	109	112	120	125
BOLT CIRCLE DIAMETER (MM)		2300	2300	2300	2300	2300	2300
BLADE LENGTH (M)		48.7	48.7	53.2	54.8	58.7	61.2

Specifications about the dimensions, types and the arrangement of the airfoils used in the LM 58.7 are not publicly available. As the geometry for the LM 58.7 is unavailable and the blade roots are of cylindrical shape a substitute blade, described later in this thesis, with cylindrical blade roots replaces the LM 58.7 and is scaled down to fit the specifications.

### 1.3.2 Description of iSpin Sensors

The iSpin sensor is an anemometer which is installed at the spinner of a wind turbine with the aim of measuring “the virgin wind flow, almost undisturbed by the rotor and the nacelle” [4, p.2]. Further, it “uses sonic anemometry, which is a conventional and robust measurement principle, also under icing conditions” [5,6]. The iSpin sensors are based on standard sonic anemometry sensors. One pair of transducers form a 1D sensor. As the WT in question is a of a three-bladed design three 1D sensors are symmetrically mounted in plane to the rotation axis in a 120° angle towards each other [4, p.2] and with 180° to the opposing rotor blade as this will ensure that the flow can pass over them through the gap between the blades. The sensors measure wind speed by sequentially sending out ultrasonic pulses, which travel from transducer to transducer. The distance between the transducers is usually 10 to

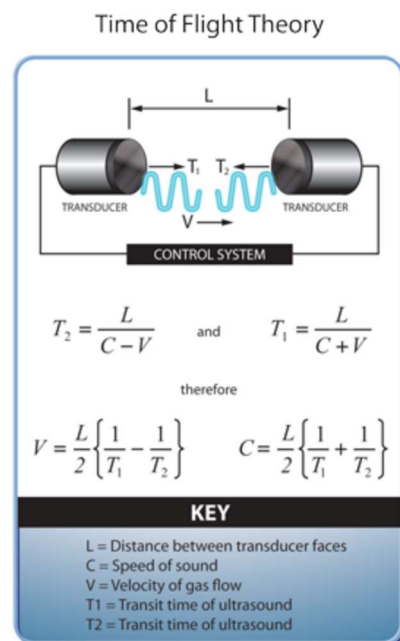


**Figure 4: Anemometry-Time of Flight Theory [7]**

20 centimetres [8]. The measuring process starts with the first transducer of sensor one, this is the sensor on the lee side, therefore, the iSpin sensors closer to the spinner. Transducer one sends a sonic pulse with the speed of sound  $c$ , to the second transducer of sensor one, which receives the pulse. As the incoming signal provokes an amplitude, transducer two needs a brief time to settle before sending a pulse itself. During this settlement phase, transducer one of sensor two sends its pulse to transducer two of sensor two. While the transducers from sensor one and two still settle, the third sensor's transducer one sends its pulse. After the third sensor has send its first pulse, the second transducer of sensor one sends its sonic pulse back to transducer one of sensor one, followed by sensor two and three completing one measurement. The reciprocal travel time needed from one transducer to the other is measured, and their difference is used to determine the velocity as depicted in figure 4 and described by equations 1 and 2 [8, p. 4].

$$t_{1,2} = \frac{\sqrt{c^2 - u_n^2 \pm u_d}}{c^2 - u^2} * d \quad (1)$$

$$u_d = \frac{2}{d} * \left( \frac{1}{t_1} - \frac{1}{t_2} \right) \quad (2)$$

Therefore, even if the wind speed varies locally in between the transducers, only a single value is recorded. Further, only the velocity parallel to the sensor path is measured. Therefore, the iSpin sensors are installed parallel the rotational axis. The frequency for sonic anemometers is usually around 10 – 20 Hz, although higher frequencies are possible. The iSpin anemometer records its data with a 10 Hz frequency, therefore recording 10 values per second. As the turbine rotates with 12.5 rpm a single rotation of the WT takes 4.8 s, during which 48 measurements are recorded. The 10 Hz data is not averaged at the sensor, but as the met mast provides only 10 minute means the 10 Hz data is also averaged over a period of 10 minutes.

Measuring the airflow over the spinner forms the basic physical principle of spinner anemometry. Therefore, the iSpin sensors are mounted in fixed positions above the boundary layer over the spinner surface, allowing them to measure changes in the wind speed at each of the three sensors. If the wind direction changes, one of the three 1D sensors will experience an acceleration in wind speed whereas another will experience a deceleration. The wind direction can thus be determined by the relative difference, which is a function of the angle of attack (AoA). Another feature of the sensors is that, over time, each sensor will measure the

same average values and therefore each sensor can be calibrated against another. This is due to the rotation of the spinner anemometer [4, p.3].

An algorithm converts the iSpin measurements into horizontal wind speed, the turbine's yaw misalignment and the inclination angle of the incoming flow.  $k_1$  and  $k_2$ , two constants specific to the spinner, blade root design and mounting position, are being utilized by the algorithm [9, p.1].  $k_1$  and  $k_\alpha$  need to be calibrated, to determine the constant  $k_2$ . The constant  $k_\alpha$  is needed for the calibration of the flow angle measurement and it can be expressed by the ratio of  $k_1$  to  $k_2$ . The 'd' in the indices marks the constants as default values, which are chosen either arbitrarily, or based on k-values from a similarly shaped spinner before starting the calibration.

$$k_\alpha = F_\alpha * k_{\alpha,d} \quad (3)$$

By relating the spinner anemometer's yaw misalignment to the yaw position, when yawing the turbine in and out of the wind repeatedly,  $k_\alpha$  is determined. With  $F_\alpha$  being the correction factor needed for correcting  $k_{\alpha,d}$ , to the calibrated  $k_\alpha$ -value.

$k_1$  is determined by the ratio of measured wind speed at the iSpin sensors to the wind speed measured at the met mast, times their respective inclination angle.

$$k_1 = F_1 * k_{1,d} = \frac{v_{iSpin} * \cos(\alpha_{iSpin})}{v_{MM} * \cos(\alpha_{MM})} \quad (4)$$

For unknown spinner shapes the defaults  $k_{1,d}$  and  $k_{2,d}$  are both set to 1. Therefore,  $k_1$  will equal the correction factor  $F_1$ . With  $k_1$  and  $k_\alpha$  having been determined,  $k_2$  can be defined as the product of both.

$$k_2 = k_\alpha * k_1 \quad (5)$$

The general procedures for determining the k-factors is, as previously mentioned, either to stop the WT at good wind speeds of 6 m/s or more for at least a day, or to measure during operation for several weeks according to IEC61400-12-2 [10], as wind speeds exceeding 15 m/s also need to be recorded. The met mast should be set at a distance of two to four times the rotor diameter to the WT, according to IEC61400-12-1 [11].

## 2. Modelling of the Geometry and Simulation Setup

### 2.1 Creating the Spinner Geometry

The 3D model is based on a point cloud or XYZ-file, recorded by a remote-controlled drone taking pictures from the wind turbines at Offenbach an der Queich and Wonnegau. The pictures of Offenbach an der Queich are converted to a point cloud and provided as a XYZ-data file. Figure 5 shows the spinner and blade roots of the WT as displayed by the point cloud in the so called “Lidarview” online tool. As can be seen on the lower left and right-hand side the software has problems to distinguish between the WT and its surroundings.

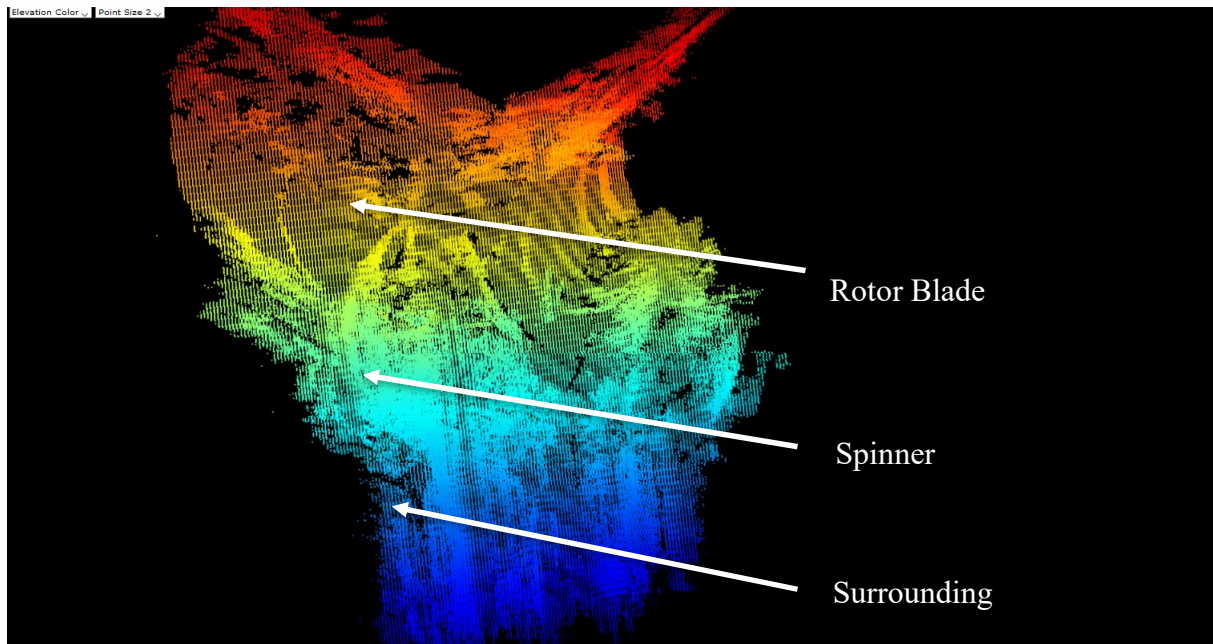


**Figure 5: Lidar View Display of Point Cloud Created from XYZ-Data [12]**

The XYZ-files are not compatible with ANSYS ICEM and must therefore be reformatted to a supported format. Different approaches are investigated in this thesis. First, the files are imported to AutoCAD and similar CAD programs to see whether they can be exported as formatted point data for ANSYS ICEM. This approach was without success. As a second attempt, the drone pictures are instead assessed in a MATLAB script, which can recognize edges in the drone pictures, if the pictures contrast is high enough. The MATLAB script converts the edges into dots, representing the spinner’s geometry. Since the translation of a three-dimensional object to a two-dimensional plane means a loss in spatial information [13, p.1] and further, the camera is influenced by the white reflective surfaces of the WT, the

resulting pictures will be distorted to certain degree. Also, the position of the drone in respect to the WT is unknown, which makes it difficult to determine the dimensions of the WT's geometries respectively.

Figure 6 shows excerpts from the Edge Transformation MATLAB script. The whole script is available in the appendix.

```
%% Edge Definition

bild = rgb2gray(imread('F:\WP Offenbach a.d. Queich_GE2.5-120\Photography\DSC09238.JPG'));
edges = edge(bild, 'canny', 0.2);

bild = rgb2gray(imread('F:\WP Offenbach a.d. Queich_GE2.5-120\Photography\DSC09022bb.JPG'));
edgesfront = edge(bild, 'canny', 0.2);

edgesfront2=edgesfront(1:end,475:2650);      % cutting of the unnecessary part
figure(1);
imagesc(edgesfront2);

edges2=edges(700:3000,1000:5000);          % cutting of the unnecessary part
figure(2);
imagesc(edges2);

%% Reconfiguration of matrix

j=1;

while j<=4001
i=1;
    while i<=2301

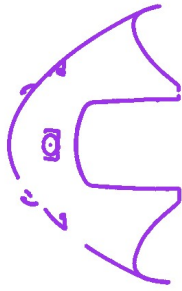
        if edges2(i,j)==1
            edges2trans(i,j)=i; %transformation of matrix edges to y-values
        end
        i=i+1;
    end
    j=j+1;
end
```

**Figure 6: Excerpt from Developed MATLAB Picture Edge Transformation [14]**

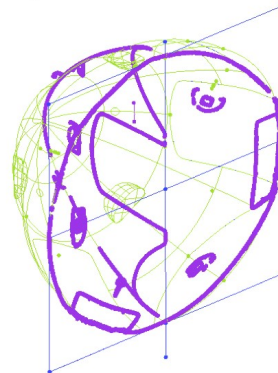
After having imported the picture into MATLAB, the function “edges” identifies and saves the outline of the geometry in a matrix. Some of the points in the matrix are removed as they are not part of the geometry and were falsely added from the surroundings by the drone's camera. An output file is written into a text file, which can be read into ANSYS ICEM.

The results shown in figure 6 are rather crude and of insufficient quality due to the already mentioned problems from transforming a 3D object to a 2D Image. Further, this approach requires formatting of the pictures so that the contrast allows the program to identify the edges. Besides the formatting the dimensions from the points for the side view compared to the top view are still off.

Edges-Transformation to Point Data



Edges-Transformation Iso-View



Edges-Transformation Side-View

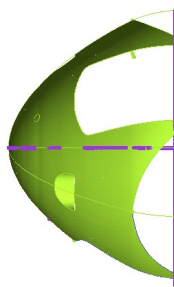


**Figure 7: Geometries Created from Picture Edge Transformation [15]**

Therefore, a second MATLAB script is written to improve the match between actual WT geometry and CAD geometry. This script allows the identification and extraction of the relevant data from the XYZ-file and thus allows for a more precise geometry in which the dimensions of the WT's geometries fit each other. To be able to do this, the XYZ-file is opened in a text file which shows a single array of numbers with no clear structure.

But the XYZ-file, as indicated by the circle in figure 8, shows a recurring pattern of six numbers. As the first three numbers show strong variations in magnitude they are suspected to represent the geometry.

```
442212.418 5502985.062 475.185 255 255 255 442212.427 5502985.061 475.180 255 255
255 255442212.475 5502985.009 475.171 255 255 255442212.479 5502985.005 475.170 2
053 255 255 255442212.502 5502985.111 475.066 255 255 255442212.504 5502985.122 4
087 475.062 255 255 255442212.519 5502984.973 475.169 255 255 255442212.519 55029
5502984.961 475.241 255 255 255442212.539 5502985.066 475.068 255 255 255442212.5
212.555 5502985.060 475.067 255 255 255442212.555 5502985.042 475.128 255 255 255
255442212.570 5502985.042 475.112 255 255 255442212.571 5502984.842 475.273 255 2
255 255 255442212.585 5502984.831 475.265 255 255 255442212.586 5502984.912 475.1
```

**Figure 8: Excerpt from XYZ-Data as Provided by Copterprojects [12]**

To extract the number group, assumedly representing the geometry, the groups of six elements are divided and sorted into a matrix. A first matrix containing all six elements is reduced to a three columned matrix, where each column represents either the x-, y- or z-axis. This matrix is stored as a sorted text file and imported to the MATLAB script shown in figure 9. Figure 9 shows excerpts from the MATLAB Point Cloud Transformation script, which is also available in the Appendix.

```

%% Input of XYZ-Files

XYZ=dlmread('romowind_w2_sorted.txt');
%% Separation of coordinates

xyz1=XYZ(1:end,4:end);

xyz2=XYZ(1:end,1:3);

%%
close all;
format long;

n=length(XYZ(1:end,1));
i=1;
x1=[];
y1=[];
z1=[];

while n>=i

    x1=[x1,xyz2(i,1)];
    y1=[y1,xyz2(i,2)];
    z1=[z1,xyz2(i,3)];

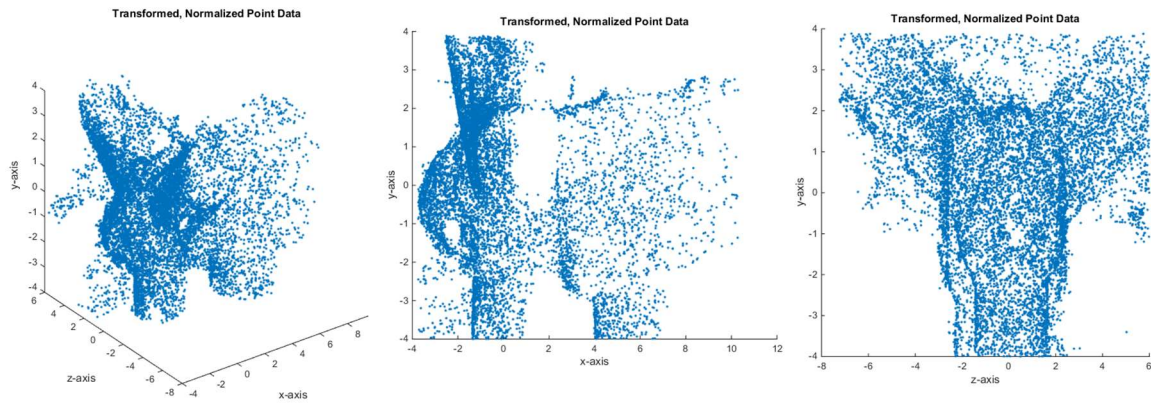
    i=i+10; %reducing number of points by 10
end

```

**Figure 9: Excerpt from Developed MATLAB Script Point Cloud Transformation [14]**

As mentioned, the x-, y- and z-axes show a large variation in their magnitudes, which leads to problems in displaying the points, which in turn prevents handling of the points in ANSYS ICEM. To avoid the displaying error, the script is modified to subtract the mean of each column from each value, thus normalizing the values. The normalization allows the points to be displayed in and to be worked with properly in ANSYS ICEM.

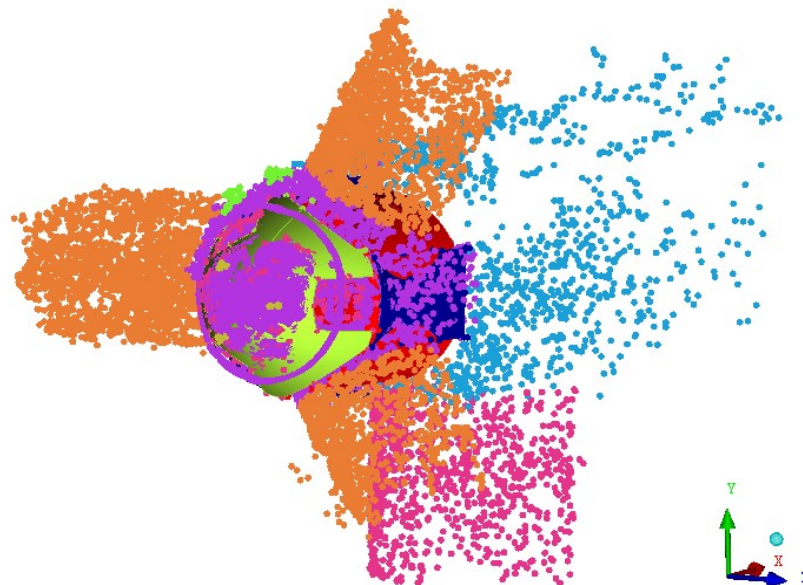
Since the drone recorded the turbine at an unspecified angle, a transformation is also conducted to turn the turbine, so that the rotational axis of the spinner correlates with the x-axis as shown in figure 10. As the angle remains unknown, only an approximation is possible.



**Figure 10: Transformed and Normalized Point Cloud Figures Created from MATLAB Script [14]**

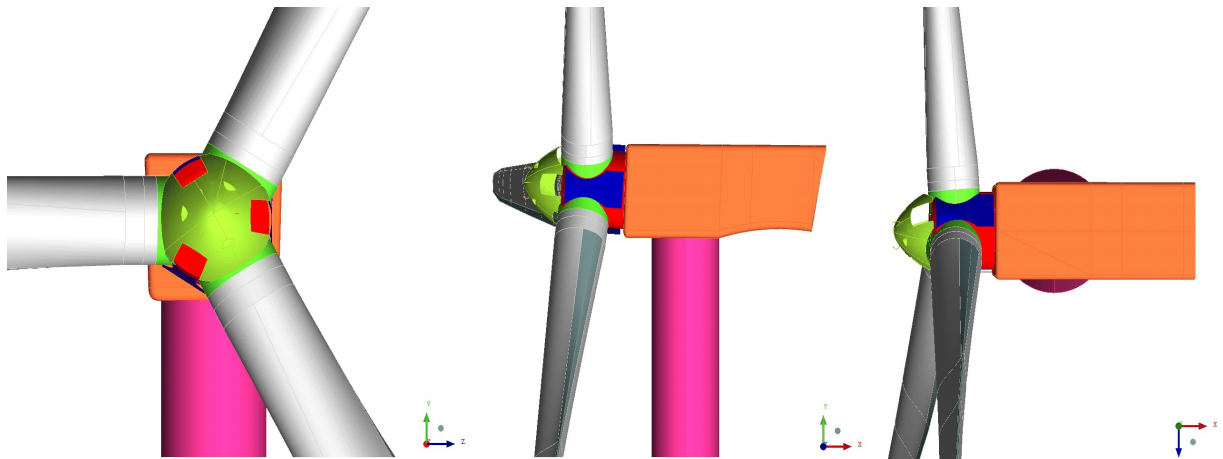
Further, the amount of points is reduced by a factor of 1,000 to improve computational speed as well as loading time. As the points are used as references for the geometry, reducing the number of points has no effect on the accuracy for the simulations, but simplifies the process of creating the geometry. In addition, residual points from the drone in front of the turbine which are not part of the turbine itself but from its surroundings, are removed. The resulting reduced matrix is plotted and written into a text file as formatted point data.

This point cloud is used as a reference to construct the nacelle, hub, blade roots and spinner. Enhancing the density of the point cloud allows for modelling finer details such as the mounting brackets and the recess clearance in the front of the spinner.



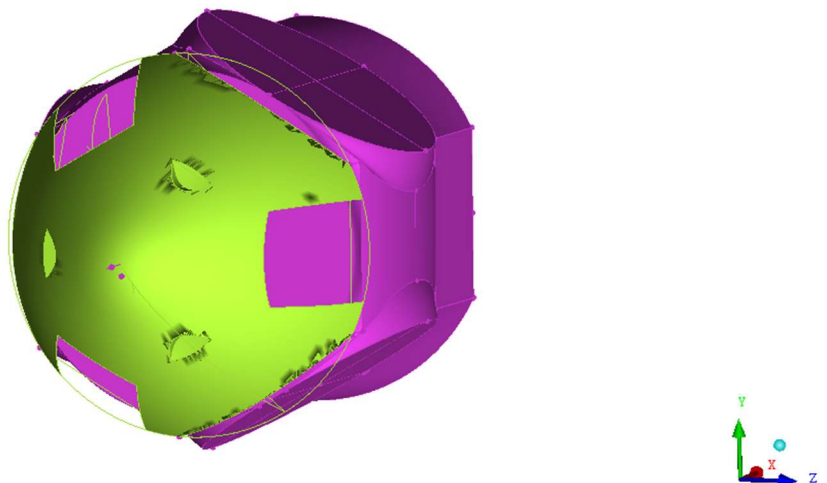
**Figure 11: MATLAB Script Point Cloud with the Modelled Geometry [15]**

Figure 11 shows the match of the formatted point cloud and the resulting geometry for the spinner. The geometry of the WT is constructed from the nacelle towards the spinner in order to provide straight lines which allow the geometry to be rotated onto the x-axis. The centre of the blades is located at the origin of the x, y and z coordinates, and the spinner faces in the negative x-direction on the y-z-plane.



**Figure 12: Front, Side and Top View of CAD Geometry Created from MATLAB Point Cloud [15]**

Picture one in figure 12 shows the spinner of the WT. As can be seen, the spinner's surface is divided into multiple parts. This is required when a surface created in ANSYS ICEM is modified; as ANSYS ICEM tries to ensure the perfect fit for the surface, it creates ripples in the surface, as shown in figure 13. This can be prevented by dividing the surface.



**Figure 13: Surface Ripples in created Spinner Surface [15]**

When compared to the actual pictures taken by the drone, the shape of the spinner appears slightly distorted. This might be related to the mentioned distortion from creating a 3D image from multiple 2D images as well as from the reflection of the white surfaces. In general, an ‘egg shape’ is to be expected when cutting parts off a parabolic shape. Further, the drone images are not shot with a direct angle, as can be seen in the first picture of figure 14.



**Figure 14: Front, Side and Top View Drone Pictures as Provided by Copterprojects [12]**

The first picture in figure 14 shows the frontal view, which also depicts the reflection of light from the white colour as well as the described ‘egg-shape’.

Since the focus of this thesis lies on the spinner, the additional equipment on the nacelle as well as the finer contours of the nacelle have been neglected. Further, the bottom of the nacelle was not sufficiently recorded by the drone and therefore the shape had to be reconstructed based on the pictures provided from Copterprojects. However, as the nacelle has a negligible effect on the incoming flow, this general shape of the nacelle will suffice and the smaller structures on the nacelle can be neglected.

## 2.2 Modelling of Wind Turbine Rotor Blades

Due to the lack of further information regarding the LM 58.7 blade, an existing blade from a previous study project at the Hamburg University of Applied Sciences is used as a better substitute for the blade’s missing geometry information. The blades were constructed according to the Dutch Offshore Wind Energy Converter (DOWEC) project as described by H.J.Z Kooilman et al. [16]. The blade was originally designed for a length of 64.5 m, consisting of six commonly used airfoils from the ‘Delft University’ and the ‘National Advisory Committee for Aeronautics’.

Thus, the DOWEC blade is adapted to replace the LM 58.7 blade and fitted to the WT, which is achieved by scaling the blade geometry down by the ratio of the actual to the desired blade

length, of approximately 0.9302 in the XYZ-dimensions. This reduces the DOWEC blade with an initial radius of 64.5 m to a radius of 60 m.

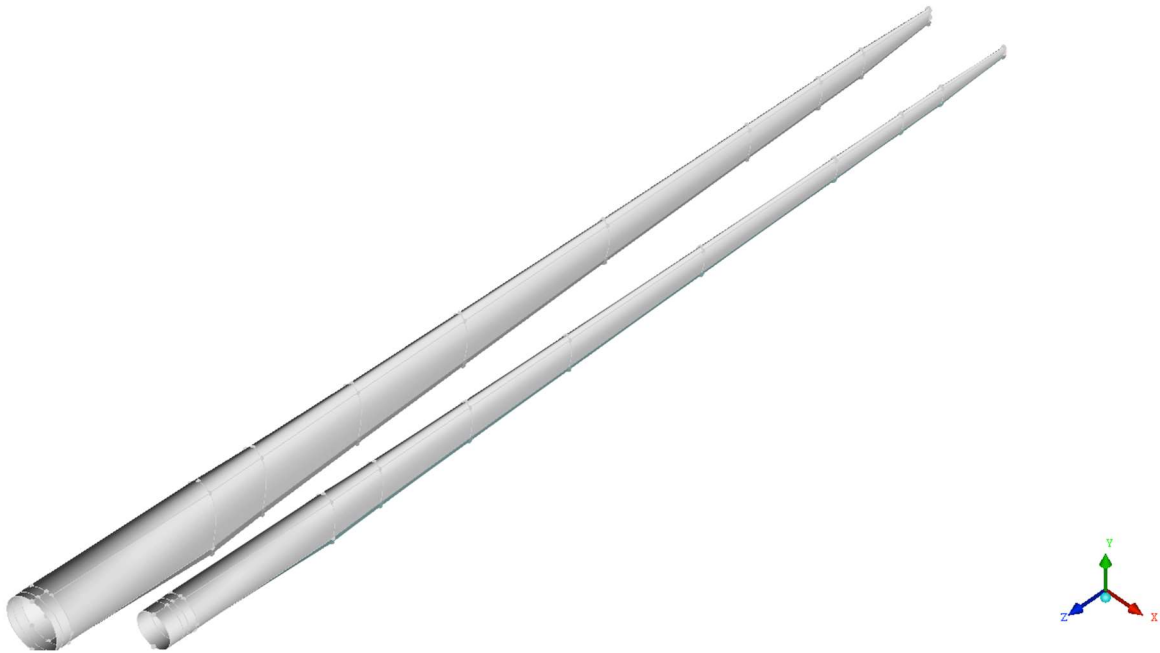


**Figure 15: Reduction of created DOWEC Blade Length by a Factor of 0.9302 [15]**

As listed in table 2 the diameter of the LM 58.7 blade roots is 2.30 m. Therefore, the DOWEC blade has to be reduced further in the XY-dimension, as the blade roots diameter is 3.26 m. The reduction factor of 0.7064 scales the blade's XY-dimension to fit the WT's geometry.

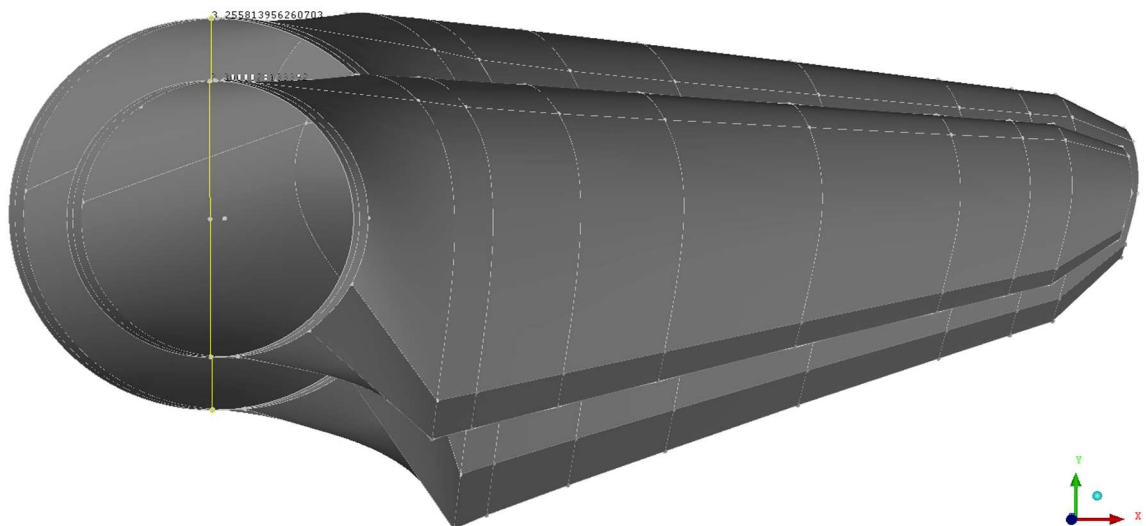


**Figure 16: XY-Dimensional Reduction of Created DOWEC Blades by a Factor of 0.7064 [15]**

The blade is created on the z-axis and tilted by 4 degree in negative x-direction with the y-axis being the axis of rotation. This forms a conical shape after the blade is copied and rotated twice by 120 degrees. After creating all three blades, the rotor is tilted 4 degrees backwards as can be seen in figure 2. The now tilted and scaled rotor fits the dimensions and the rotor axis required by the WT.

## 2.3 iSpin Sensor Geometry

Even though the size of the iSpin sensors is negligible compared to the WT's geometry, the sensor positions are helpful during post-processing for positioning and retrieving the simulated velocities. Therefore, the iSpin sensors are also remodelled in ANSYS ICEM. The dimensions for their geometry are taken from a technical drawing which served as a basis, and which is provided in the appendix. Missing dimensions such as the rod's and the sensor head's diameter are added with the help of a calliper taken from a demonstration model.

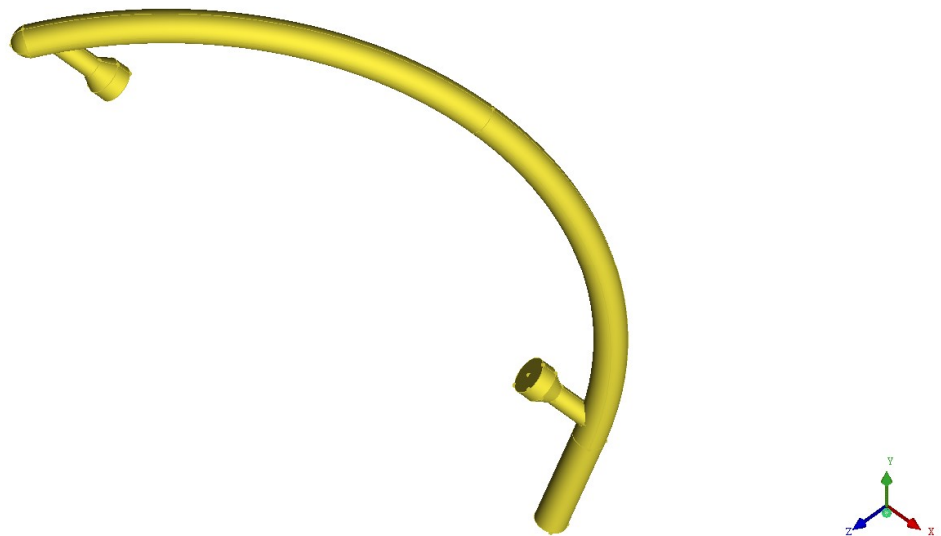


**Figure 17: iSpin Geometry recreated from Technical Drawing and Calliper Measurements [15]**

Figure 17 shows the geometry of the iSpin sensor. The sensors bushing was not modelled, as the bushing is fitted in plane to the spinner's surface to avoid displacements and maintaining the surfaces shape.

## 2.4 Meshing of the Geometry

A good mesh is the basis for reliable results. Depending on the method, it divides the geometry or area of interest into a finite number of mesh cells at whose intersections nodes are generated. At each node the governing equations, specific to the simulation usually differential equations, are solved. The quality of the results depends directly on the quality of the mesh. The mesh is created onto the geometry. However, elements for complex or small geometries can sometimes be too large, and will therefore not fill gaps or create elements above the actual surface. The more the mesh and the geometry match, the better the results [17, s.23]. Therefore, investing time into finding a mesh that fits the geometry well and does not deviate much from the geometry itself is vital.

Two main forms of meshes exist – the structured and unstructured mesh. While the structured mesh either consists of rectangular cells in two-dimensional space or hexahedrons in three-dimensional space, the unstructured mesh can consist of a mix of tetrahedrons or hexahedrons. More complex structures are also possible but seldom used. The unstructured mesh can be generated automatically with the functions for mesh generation provided by ANSYS ICEM. This requires more capacity and computational power than generating a structured mesh, but in turn renders a more flexible mesh for complex geometries and flow conditions and thus allows a better fit for these [17, s.24ff]. As the geometry for the WT's spinner is rather complex the unstructured mesh is chosen over the structured mesh.

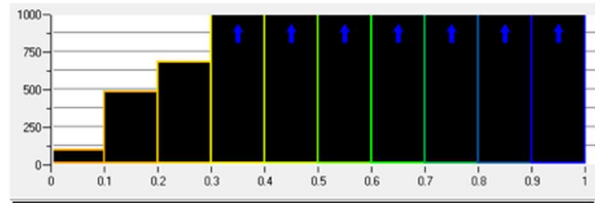
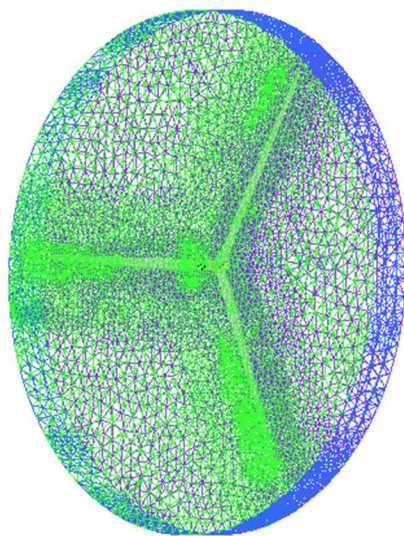
ANSYS ICEM allows for refining the mesh on a global and on a local scale. Whereas the global settings influence the physics and the type of meshing for the entire mesh, the local settings only focus on the actual area of interest, allowing for a variation of mesh-sizes over the geometry, allowing to mesh parts with a more complex geometry with a smaller mesh size.

For the WT, a volume meshing approach with the unstructured mesh type “Tetra/Mixed” is chosen for meshing the geometry. In volume meshing the interior volume of an object is meshed rather than just the surface. ANSYS ICEM identifies volumes by declaring them as a body, closed surfaces in these volumes will not be meshed, therefore distinguishing solid objects that are unaffected by flow. For the WT two bodies or volumes are selected, the surrounding and the airfoil.

The edge criterion splits elements, close to surfaces or between intersections which are greater than the selected value. This allows for a better capture of the geometry. The edge criterion of 0.075 is selected, as it achieved the best result among tested criterion settings. The scale factor in the global mesh setting allows to reduce the number of nodes quickly by increasing the locally selected mesh refinements simultaneously. This in turn makes a quick check possible to verify that the chosen settings are adequate and produce a mesh with a good fit to the geometry or whether further refinements of the mesh are needed. If a generally good fit is found, the mesh can be refined further by using the function Curvature/Proximity Based Refinement. All mesh settings selected for the WT are listed in the appendix.

As the spinner has a more complex geometry due to recesses on the spinner's nose and openings on its base, the mesh for the spinner geometry is finer than the rest of the WT's geometry. The local settings vary from 0.005 m at the iSpin sensors and 0.01 m at the spinner to 25 m at the walls of the surroundings. Since the spinner and blade roots are the object of interest, the finer mesh makes sense, as the tower is of less interest during this thesis, the mesh size is limited to 1 m. The nacelle's surfaces were difficult to close, therefore a finer mesh size of 0.08 was selected.

Although a finer mesh was available for the geometry, the mesh was scaled down to a coarser mesh, since the number of simulations and the amount of time required to run all simulations with the finer mesh exceeded the available capacities. However, the coarse mesh should already deliver a good approximation of the actual results: ANSYS ICEM provides a mesh quality check, which subjects the mesh elements to geometry checks amongst others on maximum angles, warpage, and skewness. This option allows to check the overall quality of the mesh. According to the 'ANSYS ICEM CFD Tutorial' by David Ryan [18, p.7], the mesh should have a mesh quality of above 0.35-0.4. If that is not the case, the mesh should be smoothed further to improve its quality. As the histograms in figure 18 of the spinner geometry and figure 19 of the surrounding geometry show, 99.8 % of the spinner and rotor blade geometry elements, and for the surrounding geometry even 99.9 % of the elements, are above 0.4. Therefore, the mesh quality appears to be acceptable.



Histogram of Quality values  
 0.9 -> 1.0 : 732412 (45.955%)  
 0.8 -> 0.9 : 245940 (15.432%)  
 0.7 -> 0.8 : 180596 (11.332%)  
 0.6 -> 0.7 : 154826 (9.715%)  
 0.5 -> 0.6 : 157127 (9.859%)  
 0.4 -> 0.5 : 119725 (7.512%)  
 0.3 -> 0.4 : 1858 (0.117%)  
 0.2 -> 0.3 : 684 (0.043%)  
 0.1 -> 0.2 : 481 (0.030%)  
 0.0 -> 0.1 : 96 (0.006%)

Log  Save  Clear



Figure 18: Mesh Quality of Created Spinner and Rotor Blade Geometry [15]

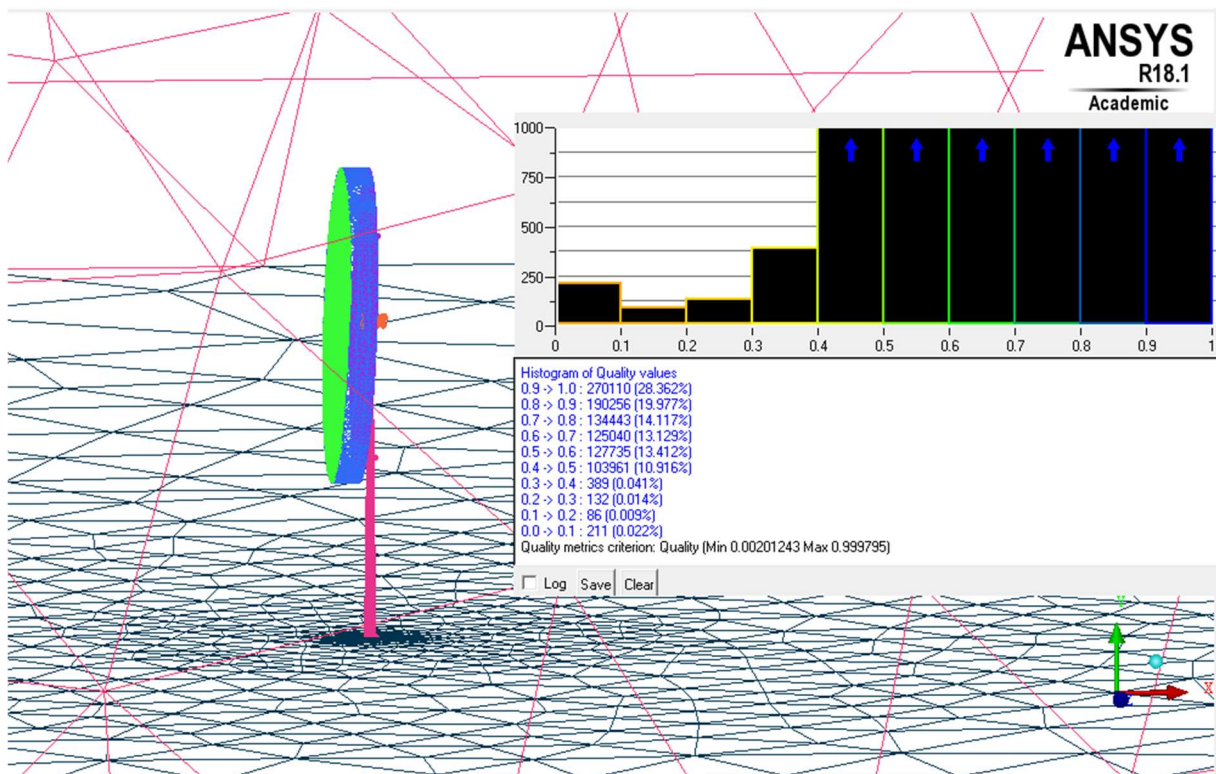


Figure 19: Mesh Quality of Created Surrounding Geometry [15]

## 2.5 Simulation Models and Boundary Conditions

Since CFD simulations were introduced to engineering when capacities of computers and storage were still limited, simplifications were introduced to minimize the impact of the available resources. With the increase of computational capacities as well as storage space, more complex CFD simulations became more and more applicable.

Nevertheless, some of the early implemented models are still used whenever computational efforts required for a simulation need to be reduced. These models represent different approaches to problems.

One of these models is the ‘Frozen Rotor’ or ‘moving reference frame model’, which is one of three frame change / mixing models, the others being the ‘stage’ model, which is used for multi-staged machines, and the ‘transient’ model, which can replace both the frozen and the stage model. The reason against using the transient model in this study is the required simulation time and disk space [19, p.161], both of which are too high for the scope of the present thesis.

The frozen rotor model is needed for general connections, allowing to connect regions with interfaces. Occurring for example, between a stationary and a rotating frame of reference, such as present with a WT. Here the nacelle and tower are part of a stationary frame, while the rotor blades are rotating. As the name suggests, the interfaces are kept in a fixed position throughout the calculation. Due to this, the frozen rotor model requires the least amount of computational effort amongst the frame change / mixing models. As the frozen rotor produces a steady state solution, the transient effects that would occur at the interfaces are not modelled. The same goes for the losses which incur through the flow mixing between stationary and rotating components these are also not modelled and thus introducing a small error. Additional modelling errors may occur, if the through flow speed is small relative to the rotor speed at the interface [19, p.161]. As this is not the case for the WT these can be ignored.

The frozen rotor model can be seen as equivalent to a rotational simulation, with the difference that a ‘snapshot’ during the rotation is observed, at which the results of the model in the geometry defined position inside the moving reference frame, are provided [20]. Therefore, the rotor will not change its position in the frozen rotor model, while the flow is

simulated to move around the blade, thus creating a similar effect to a rotating rotor. This in turn has another drawback, as it only shows one rotor position and will not allow to see effects such as the blades moving over the tower which would only be possible for a transient run.

Despite the listed drawbacks and with the incurring losses due to having a steady state run instead of a transient run, the frozen rotor model was selected for this thesis, since the focus lies on finding the  $k_1$ -factor for the WT and the frozen rotor model allows for a good approximation of this.

CFD allows to solve the governing equations that define fluid dynamics, such as Newton's second law and the conservation of mass and energy, which are described by differential equations whose solutions depend on the chosen initial and boundary conditions. The boundary conditions for the simulation are based on the measurement data of the met mast. Temperature, air density and pressure are kept constant whereas the wind velocity is variable. To study their effects, three different flow profiles are implemented, as listed in table 1, chapter one. The influence of the terrain surrounding a wind site on the wind's velocity is shown in figure 20.

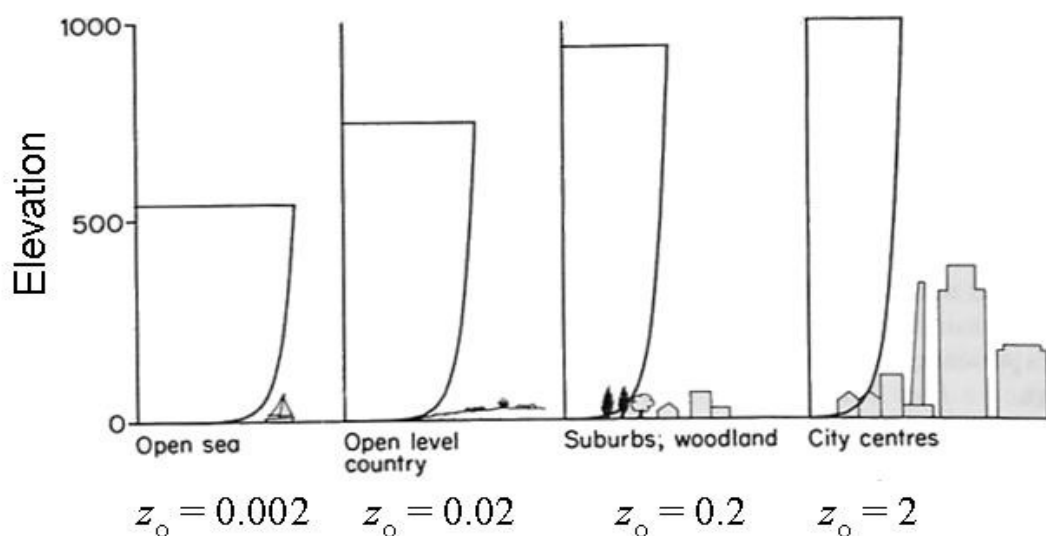


**Figure 20: Logarithmic Wind Profile for Different Terrains [21, p. 3]**

Figure 20 describes the dependency of the logarithmic wind profile on the roughness length  $z_0$ . The roughness length is a measure for the terrain roughness which influences the slope of the logarithmic wind profile. The theoretical logarithmic wind profile as described by equation 4 uses the roughness length  $z_0$  with the stability corrections  $\Psi$  and the

Monin-Obukhov length  $L^*$  to calculate velocities at higher altitudes.

$$u(y) = \left(\frac{u_1}{\kappa}\right) * \left(\ln\left(\frac{y}{z_0}\right) - \Psi * \left(\frac{y}{L_1}\right)\right) \quad (6)$$

Neither the roughness length for the terrain surrounding the WT and the correction factor nor the Monin-Oberov length are known for the wind site studied in this thesis. The logarithmic wind profile's slope and curvature are approximated well by the wind profile described by the empirical power law. For certain roughness's and unstable conditions, the empirical power or Hellmann exponential law can describe the logarithmic wind profile. The empirical power law is also often used for wind energy applications due to its mathematical simplicity [22, p. 61]. The empirical power law will be referred to as logarithmic wind profile henceforth. The Hellmann exponent  $\alpha$  must be determined from the available met mast data.

$$u(y) = u_1 * \left(\frac{y}{y_1}\right)^\alpha \quad (7)$$

$$\alpha = \frac{\ln\left(\frac{u(y)}{u_1}\right)}{\ln\left(\frac{y}{y_1}\right)} \quad (8)$$

Based on the met mast data, the mean Hellmann exponent for the WT at Offenbach an der Queich is 0.197 with a standard deviation of  $\pm 0.147$ . To exclude interferences from other WT in the wind park, only values for a wind corridor of 200 to 250 degree facing the direction of the met mast are considered. Further, negative values are not considered as that would imply a decrease in wind speed with increasing height. Therefore, the  $\alpha$ -value is set to 0.2 for all simulations.

The cut-in velocity is 3 m/s and the nominal power is reached at 11 m/s. Cut-off wind speed is reached at 25 m/s [2]. From experience with the k-factor calibration the range between the cut-in speed and the nominal wind speed are affected by rotor induction. Rotor induction describes the effect of non-linearity between the met mast data and the expected velocities measured by the iSpin sensors. Therefore, the inlet wind velocities 4, 12 or 16 m/s are entered as the initial value  $u_0$  and then split up into a three-dimensional wind vector denoted as  $v_u$ ,  $v_v$  and  $v_w$  representing the wind velocities in x, y and z direction. The angle  $\varphi$  defines the inclination of the logarithmic wind profile towards the wind turbine, which is set to 5 degrees as a larger malposition is unusual. For the block wind profile, the  $\alpha$ -value is zero as well as the inclination angle  $\varphi$ . The following equations 7-10 define the initial conditions for the simulation.

$$v_{profile} = u_0 \left( \left( \frac{y + y_{hub\ height}}{y_0} \right) \right)^\alpha \quad (9)$$

$$v_u = \cos(\varphi) * v_{profile} \quad (10)$$

$$v_w = \sin(\varphi) * v_{profile} \quad (11)$$

$$v_v = 0 \text{ m/s} \quad (12)$$

Therefore, the wind velocity for the block profile over the whole air column is constant. For the logarithmic wind profile, the velocity increases with increasing height. The same applies to the 'logarithmic wind profile with inclination angle' with the exception that  $\varphi$  is set to 5 degrees. The resulting formulas are shown in table 3.

**Table 3: Wind Profile Equation Table**

	Block Profile	Logarithmic Wind Profile	Inclined Logarithmic Wind Profile
$v_u =$	$1 * u_0$	$1 * u_0 \left( \left( \frac{y + y_{hub\ height}}{y_0} \right) \right)^\alpha$	$\cos(5^\circ) * u_0 \left( \left( \frac{y + y_{hub\ height}}{y_0} \right) \right)^\alpha$
$v_v =$	0	0	0
$v_w =$	$0 * u_0$	$0 * u_0 \left( \left( \frac{y + y_{hub\ height}}{y_0} \right) \right)^\alpha$	$\sin(5^\circ) * u_0 \left( \left( \frac{y + y_{hub\ height}}{y_0} \right) \right)^\alpha$

The boundary conditions, set in pre-processing for the simulation's inlet and outlet are set to a subsonic flow regime, as the velocities experienced in this thesis are below the speed of sound, further the turbulences are set to a medium value of 5 %, since it gives a good approximation when levels are unknown [23]. The sides' boundary conditions are set to symmetry, which defines the flow on both faces of the sides planes as mirrored, therefore extending the flow field to the sides without increasing computational effort. The top is defined as opening, which is a valid setting if no information about a boundary. As the bottom boundary represents the ground, it is set to 'wall', which is impermeable and therefore air cannot pass through, it is also defined as a 'no slip wall', which will set the flow close to the bottom boundary to zero velocity. Further, the initial conditions defined in pre-processing, and needed to start the simulation, are the gaseous environment, which is simulated as ideal gas with an air density  $\rho$  set to  $1.2253 \text{ Kg} \cdot \text{m}^{-3}$ , the air pressure, which is set to 1 atm the inlet, and the air temperature, which is set to 288 K. Further, the nominal design of the WT allows the rotor to rotate at 12.5 rpm as specified by the installation report of the WT, therefore 12.5 rpm is set as the rotational speed in pre-processing [24].

## 3. Simulation Strategies

### 3.1 Conducted Simulations

While the geometry for the GE-Spinner and for the turbine is created from the photogrammetry, a first simulation, to test the logarithmic wind profile with an adapted blade from the DOWEC study project is run, in which the blade and respectively the geometry are downscaled to fit the description for the GE 2.5-120 as described in chapter 2.2 “Wind Turbine Rotor Blades”.

The first simulation is run to check plausibility of the general setup and as a reference as well as a test for the created wind profile. The nacelle’s and the spinner’s geometries were kept relatively simple, the nacelle was modelled as a simple cylindrical geometry and the spinner was modelled as half a sphere.

The process of creating a mesh was described in chapter 2.3 “Meshing of the Geometry” and shows that generating a quality mesh with a high node count can be a lengthy process. Further, a fine mesh requires much more loading and computation time than a coarser mesh. Therefore, a coarse mesh with about 440 thousand nodes was chosen to allow for quick simulations with sufficient iterations, although suffering some losses in mesh quality.

The number of iterations was defined to 4198, since the test simulation with the DOWEC turbine was stopped at that iteration count. Otherwise a step count of 4000 iterations is a sufficient number for coarse meshes.

For each of the three wind velocities three simulations with the previously described wind profiles are conducted. As will be discussed further below, two additional simulations are introduced. One of which replaces the airfoils from the DOWEC rotor blades by cylindrical cross sections. This will show how the blade shape influences the  $k_1$ -factor. The other simulation rotates the blade by 180 degrees. As the spinner should have rotational symmetry, the rotated geometry should deliver similar values to the original simulation.

### 3.3 Macroinstructions for Current and Future Cases

Due to the high number of simulations conducted and to provide comparability between the simulations, all simulations are based on the same pre-file. Therefore, setting up a new simulation for a different wind profile includes only changing the value of the  $\alpha$ -value or the inclination angle as well as changing the inlet velocity.

The same is done for post-processing: the finished simulation's result-file from the solver are imported into one macro file. The macro file will ensure that for each case the same report structure is generated to allow for quick comparability. As some of the contour plots show a scale e.g. for velocity and as some of the scales are defined by user input, these scales need to be updated by hand.

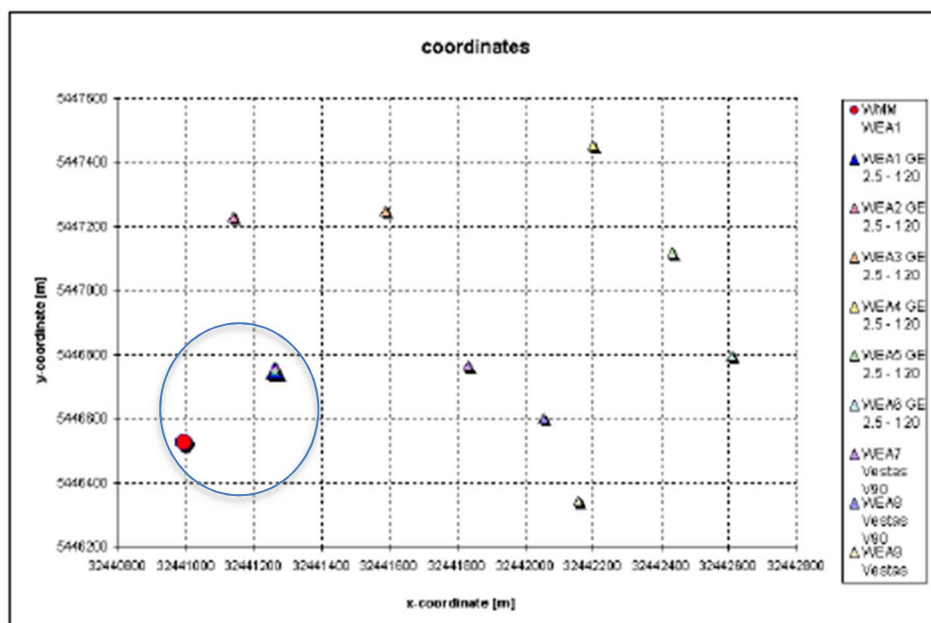
## 4. Evaluation of Experimental and Measured Data

### 4.1 Met Mast Data

The met data and the supervisory control and data acquisition (SCADA) data available for the WT at Offenbach an der Queich are combined in an excel file allowing to filter out unwanted parameters from both. The SCADA data is averaged over 10 minutes to match the iSpin data, which is also averaged over 10 minutes based on the 10 Hz data as described in chapter 1.3.2.

Certain values must be excluded from the measurements, as the data includes data points, which are outside the wind speed interval of interest. Additionally, the data is filtered for blade angles bigger than 6 degrees, as this removes all values affected by rotor induction for this turbine type.

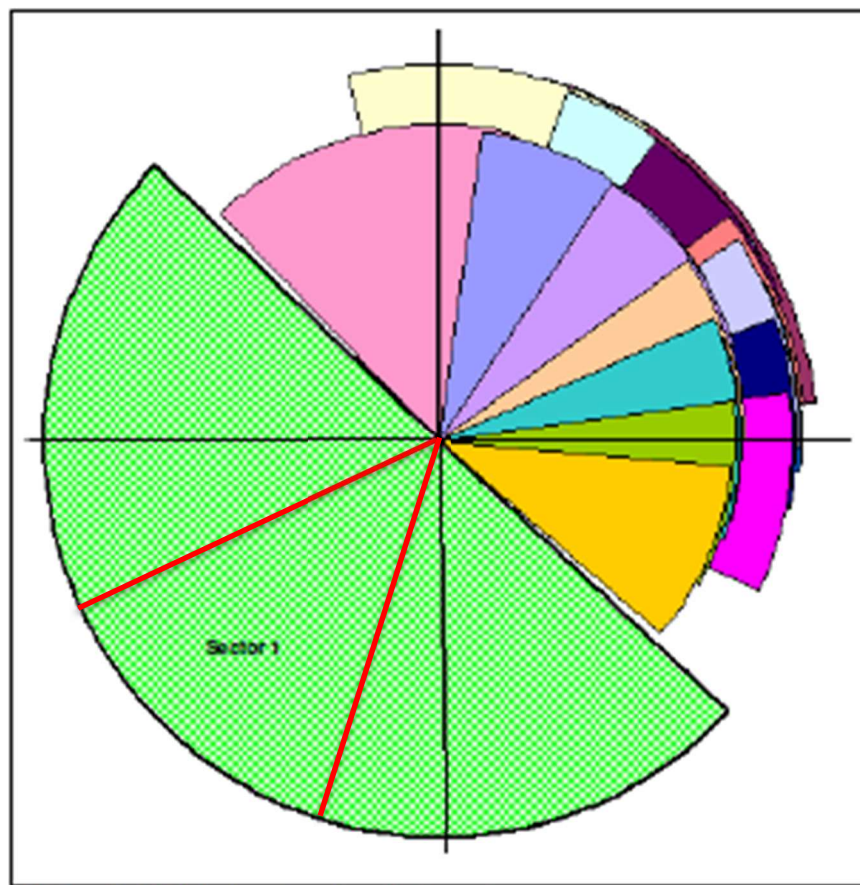
In order to determine the described Hellmann-Exponent  $\alpha$  for the logarithmic wind profile a wind corridor is used as a filter that removes all measured data for cases where the wind first passes the WT and then the met mast. Figure 21 shows the positioning of other wind turbines at Offenbach an der Queich. The circled markers show the WT being examined in this thesis in blue and its met mast in red.



Picture 3-2 Sector of evaluation - 2

Figure 21: Position of Met Mast and Wind Turbines at Offenbach an der Queich from Installation Report [24]

As the wakes of the other turbines would corrupt the measurement of the examined WT and met mast for determining the  $\alpha$ -value, a corridor of 50 degree is set as a filter. Figure 22 shows the wind sectors for the WT at Offenbach an der Queich with sector 1 being unobstructed by other turbines. As the installation report defines the sector between 133.1 and 316.4 degrees, the resulting 50 degree corridor, marked in red, coincides with the position of the met mast ruling out obstacles that might influence the unhindered development of the logarithmic wind profile.



Picture 3-1 Original sector of evaluation - 1

**Figure 22: Wind Sectors for Wind Turbine at Offenbach an der Queich [24]**

As the wind speeds of interest range from 3 to 16 m/s, another filter for said range is implemented. Figure 23 shows the measured wind speeds from met mast and from the iSpin sensors plotted against each other. A regression line allows to display the slope. The slope of the regression line is the k-factor for the WT as described in chapter 1.3.2, as it is the ratio of wind speed at the met mast to the wind speed measured by the iSpin sensors. The k-factor for the WT is 0.553 for the valid met mast data selected.

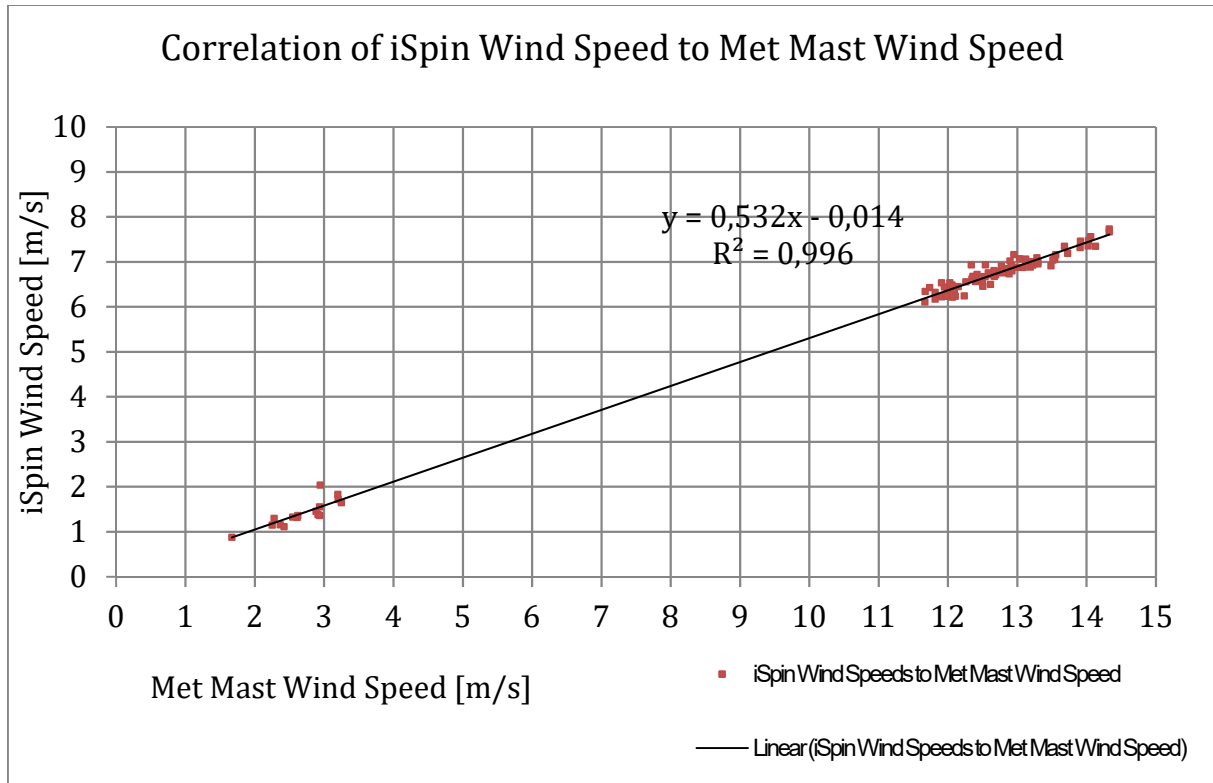


Figure 23: Correlation of iSpin Wind Speed to Met Mast Wind Speed from Met Mast Data [25]

### 4.1.1 Verification of the Wind Profile Exponent Alpha

In the first attempt of creating a ‘logarithmic wind profile’ the exponent  $\alpha$  was assumed at 0.2 as it is a value that describes open country rather well. To verify the value for the wind site in question the met mast data is taken into consideration.

The corridor described in chapter 4.1 “Met Mast Data”, is used to exclude influences on the met mast’s measurements. This ensures that only met mast data is used to recreate the  $\alpha$ -value. The value was already described in chapter 2.4 “Simulation Models and Boundary Conditions” by equation five. Equation six is used to recreate the value from the measured data. Taking into account the corridor filter described previously, the removal of negative values and values above 1.0, 718 values remain.

The average of the 718 values is, as also described previously, 0.197 with a standard deviation of  $\pm 0.147$ . The distribution of the calculated  $\alpha$ -values is depicted in figure 24. Therefore, the assumed value selected for the first simulation with the DOWEC simulation matches the actual value. According to the  $\alpha$ -value the terrain in front of the WT is open country. Figure 24 shows the distribution of the single  $\alpha$ -values.

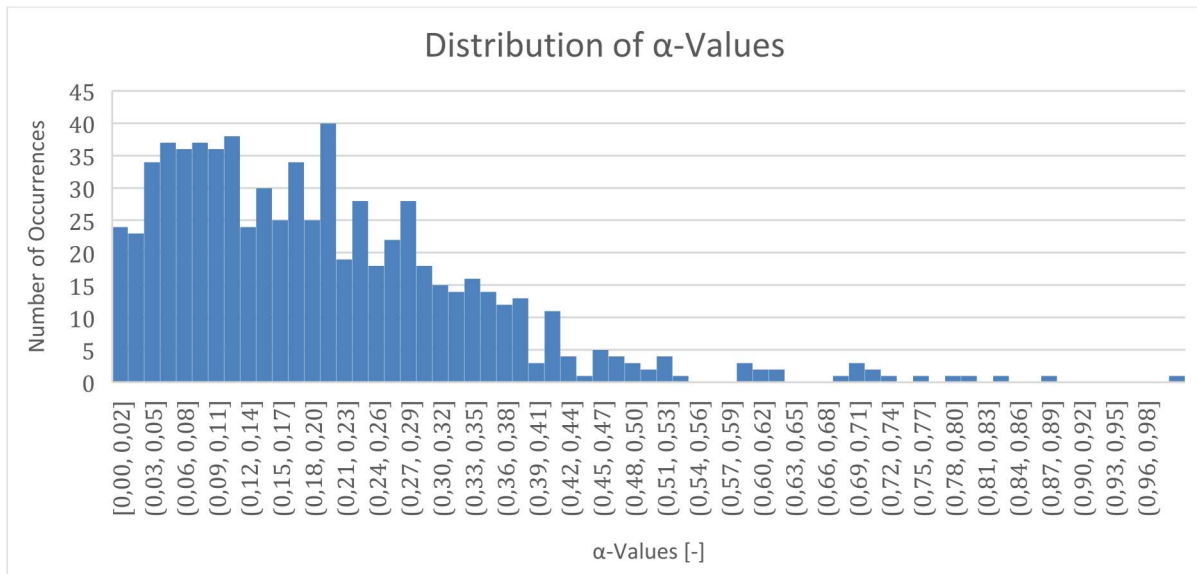


**Figure 24: Distribution of  $\alpha$ -Values from Met Mast Data [25]**

## 4.2 Plausibility of the Experimental Data

After the simulations have finished, the simulations result files are checked for their plausibility. To check the plausibility, certain aspects of the geometry, i.e. the flow over the airfoils, the power generation of the turbine, and the velocity in front of the spinner, are investigated.

### 4.2.1 Power Generation of the Simulated Wind Turbine

One aspect of proving the plausibility of a simulation is to check whether the model geometry behaves and operates as it should under the given initial and boundary conditions. Since the WT is supposed to generate power, and since the WT's power curve is known, as displayed in figure 3 in chapter 1.3, the simulated power can be used to check if the WT operates as it should. The power curve shows that the WT can generate about 200 kW at 4 m/s and 2.5 MW at 12 m/s up to the cut-off wind speed of 25 m/s. The simulated WT generates roughly 200 kW at 4 m/s but the power produced for 12 and 16 m/s is actually less .

Although unlikely, the discrepancy between the simulated and expected power output of the WT for 4 m/s, could be linked to the rpm of 12.5 which have been set too high. For 4 m/s the WT should rotate with 7.5-8 rpm according to the SCADA data. However, this would not explain the discrepancy of the power generated at 12 m/s. As the blades are responsible for the power generation, the blades will be investigated further in chapter 4.2.2.

## 4.2.2 Angle of Attack and Pressure Coefficient over the Blade

As the power output of the simulation does not match the nominal power of the WT, the setup of the DOWEC blade design has to be questioned as the design of the blade is the decisive factor for the power generation. Figure 25 shows the airfoil DU30 at a radius of 19 m. The blue trail visible on the tail of the airfoil shows a separation bubble. A separation bubble is an indication for an incorrectly chosen AoA and therefore an incorrect blade design.

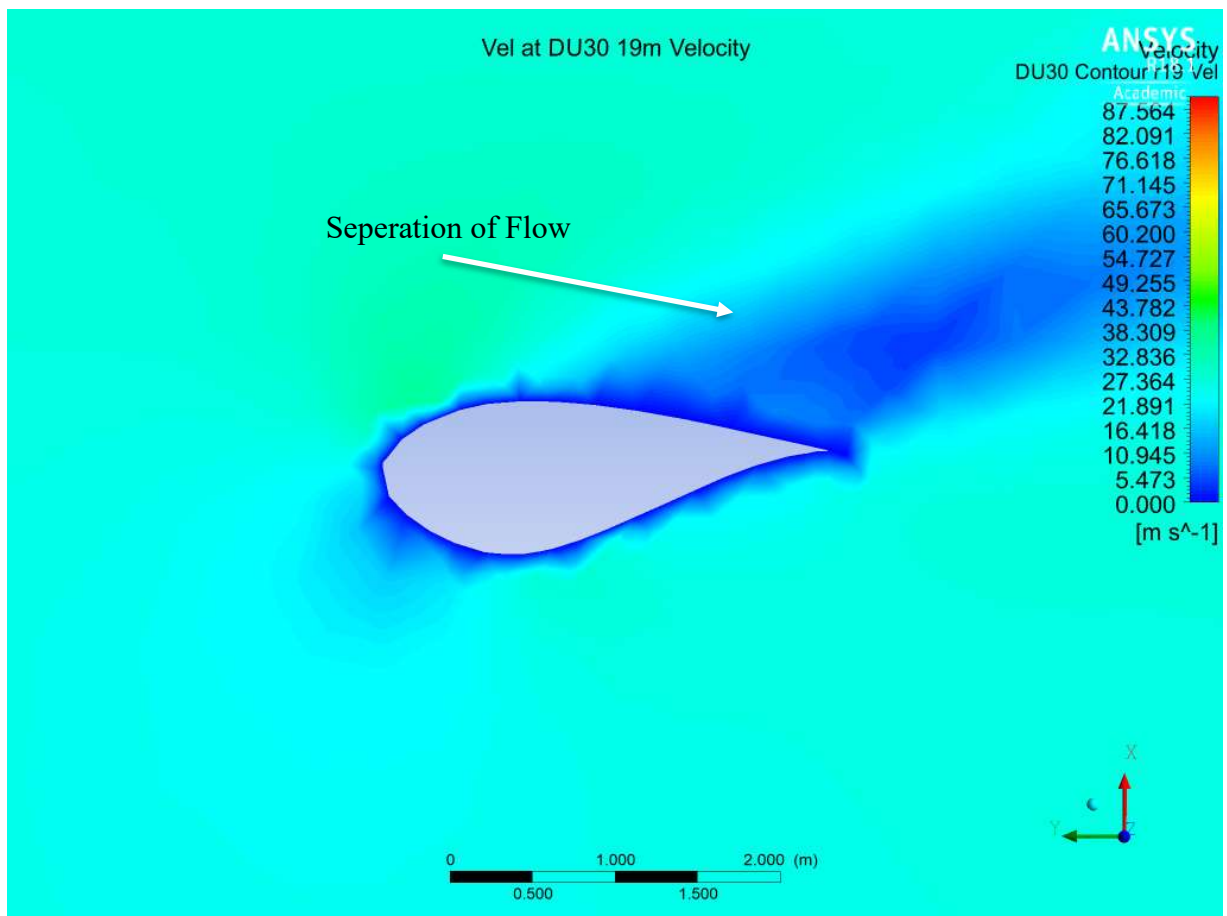


**Figure 25: Separation Bubble at Airfoil DU30 from Simulation [26]**

This can also be observed for the negative pressure coefficient  $C_p$  as displayed in figure 26. The  $C_p$  is a dimensionless value that describes the pressure distribution over an airfoil in a flow [27]. The intersection, circled in figure 26, leads to the conclusion that the airflow is separated from the airfoil and therefore, the simulated WT is not performing as well as it could. Figure 27 shows the negative  $C_p$  of the same airfoil from the DOWEC study project and therefore in a functioning blade design.

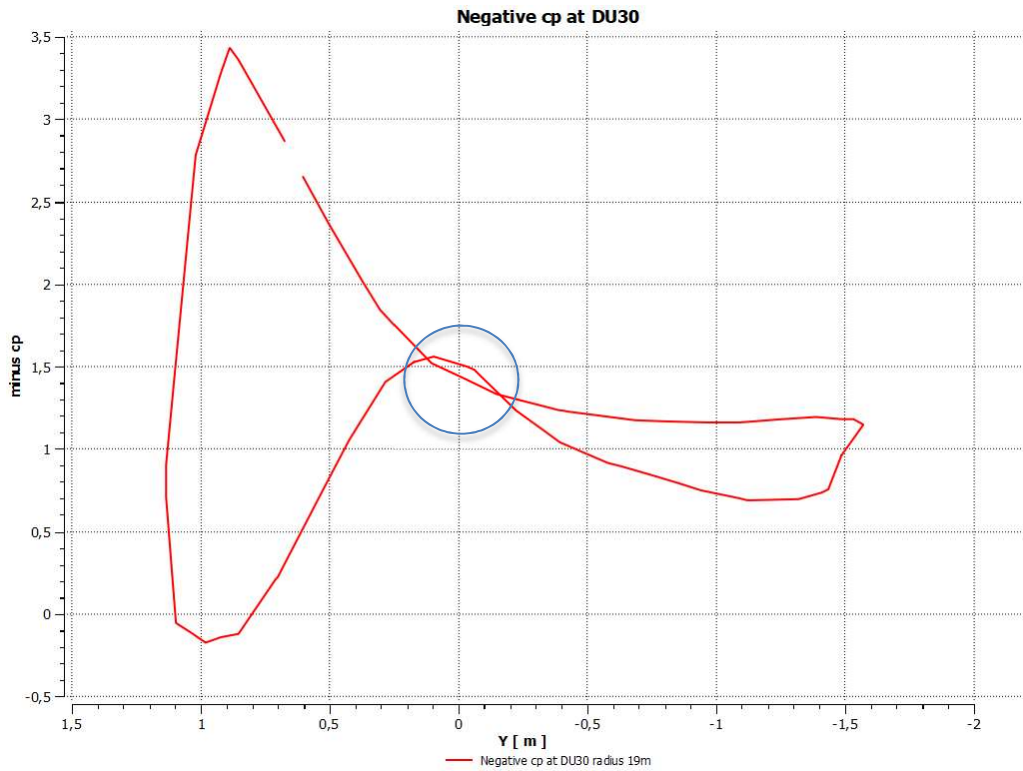


**Figure 26: Pressure Coefficient Cp at Airfoil DU30 from Simulation [26]**

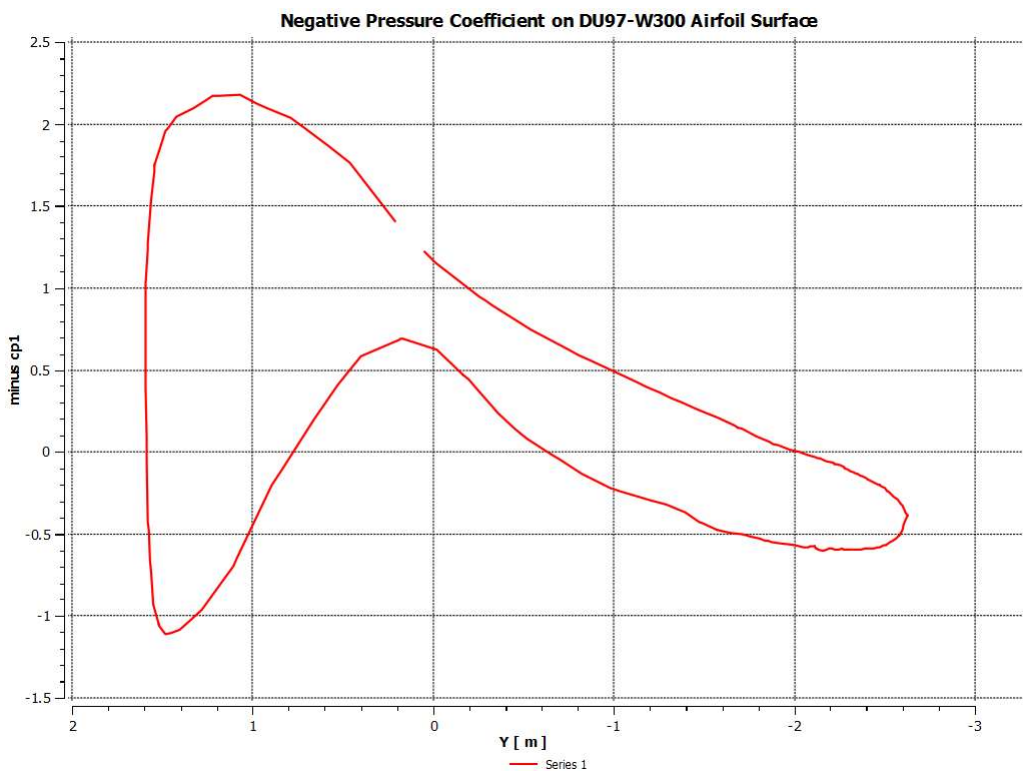
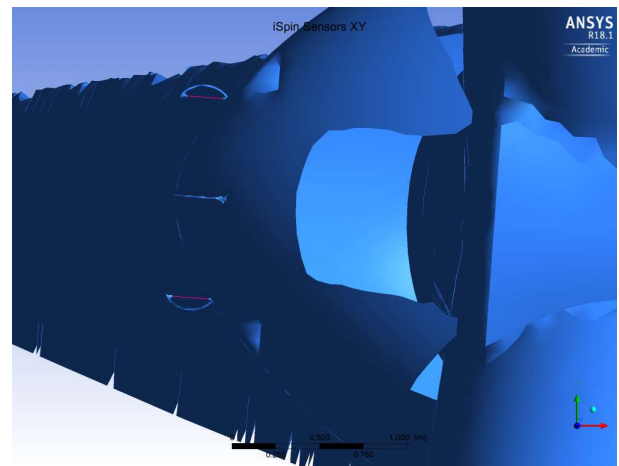
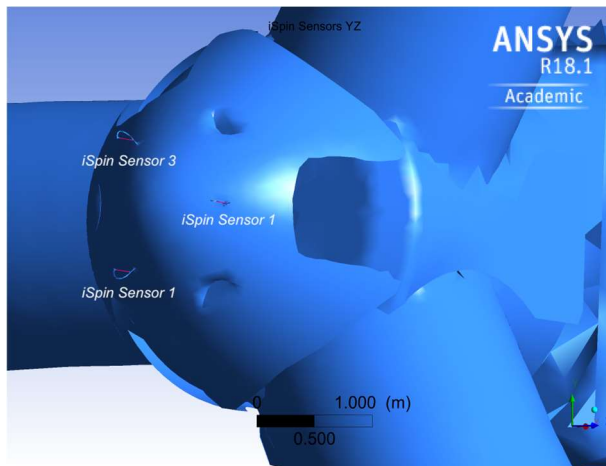


**Figure 27: Pressure Coefficient Cp at Airfoil DU30 from the DOWEC 6 MW Study Project [26]**



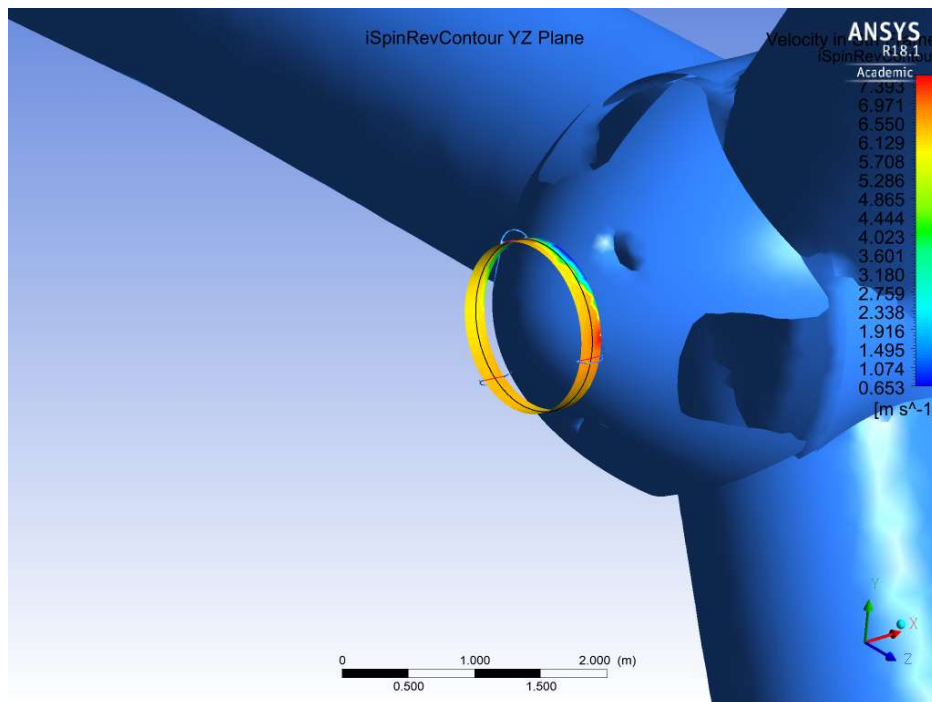
### 4.2.3 Mass Flow Behaviour in Front of the Wind Turbine

Figure 29 and 30 show the position of the iSpin sensors from the YZ- and from the XY-plane. The sensor paths are displayed as thin red lines. These red line, inserted in CFD-Post for post-processing, are called poly lines, which allow to extract values at these positions. The sensor numbering is shown in figure 29. Figure 31 shows the velocity over the surface that is swept by the sensors path. The displayed velocity is in stationary frame.



**Figure 29: Position of the iSpin Sensors – View at YZ Plane from Simulation [26]**

**Figure 30: Position of the iSpin Sensors seen from XY-Plane from Simulation [26]**



**Figure 31: Velocity in Stationary Frame at iSpin Position from Simulation [26]**

Figure 32 shows the spinner of the WT and the distribution of the velocity in stationary frame  $u$  over its surface. As expected, the stagnation point of the incoming air flow is slightly beneath the spinner's middle, since the spinner and the rotational axis are tilted back by four degrees. As the WT is rotating clockwise, the visible velocity distribution between the rotor blades show an increase against the rotational direction. Behind the rotor blade at the 240 degree position, lower velocities can be seen while higher velocities are visible at the front of the blade in 120 degree position.

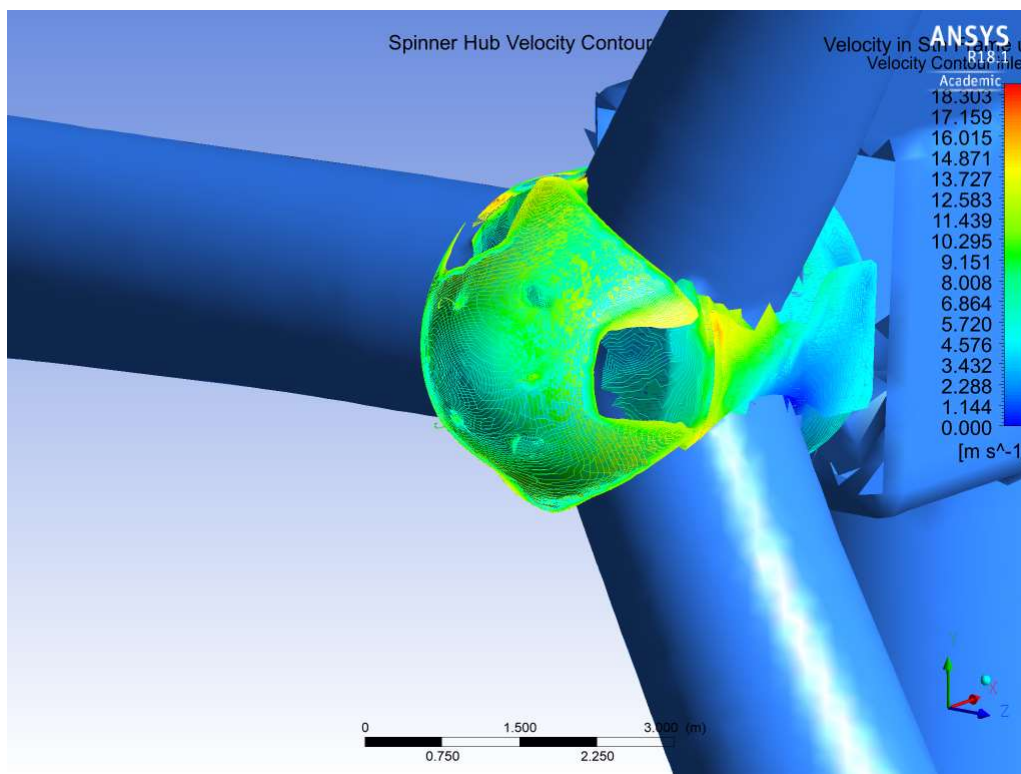


**Figure 32: Velocity over Spinner Surface in Stationary Frame  $u$  from Simulation [26]**

Unexpectedly, the velocities over the spinner's surface are only at about 40 % of the initial velocity. As a small decrease in the wind velocity is to be expected, since the WT presents an obstacle in the winds path, the simulations therefore appear plausible, although the magnitude of the decrease needs to be investigated, which is done during chapter 5.

As the velocity decreases and the energy in the wind must remain the same, the pressure should increase. This can be observed in figures 33 and 34. Especially on the blades in 120 and 240 degree position.

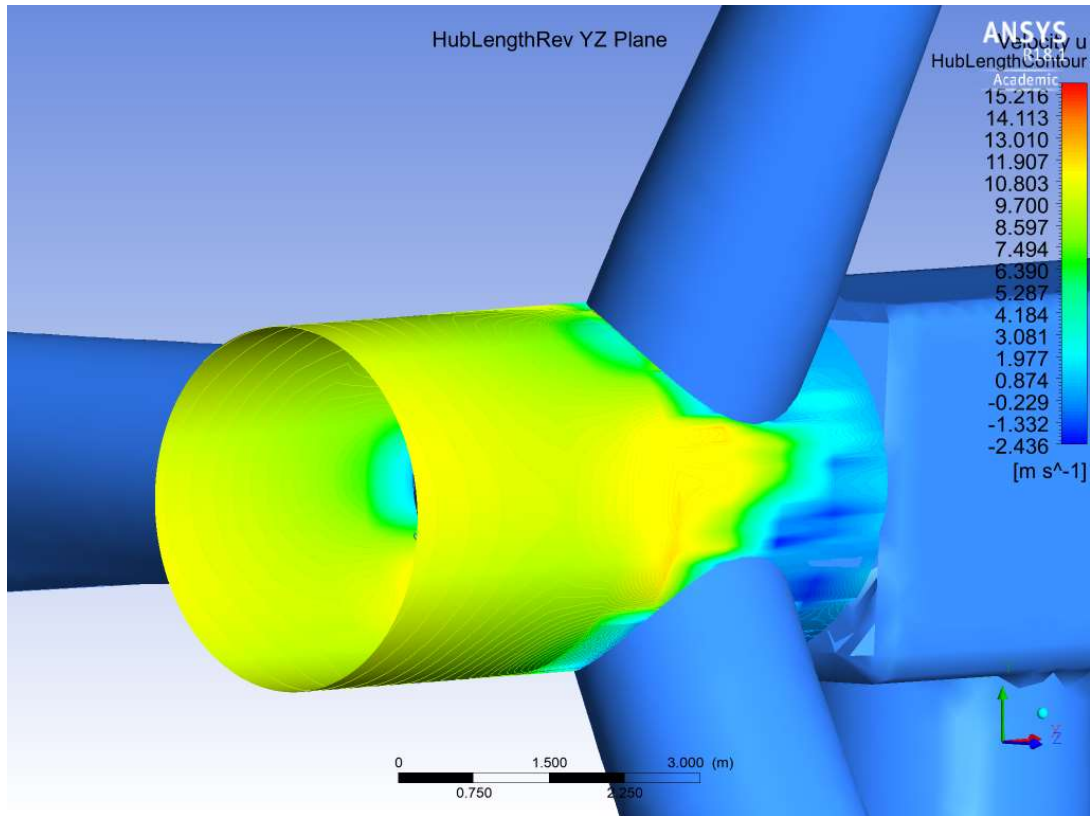


Figure 33: Velocity in Stationary Frame u over Cylindrical Surface at Spinner from Simulation [26]

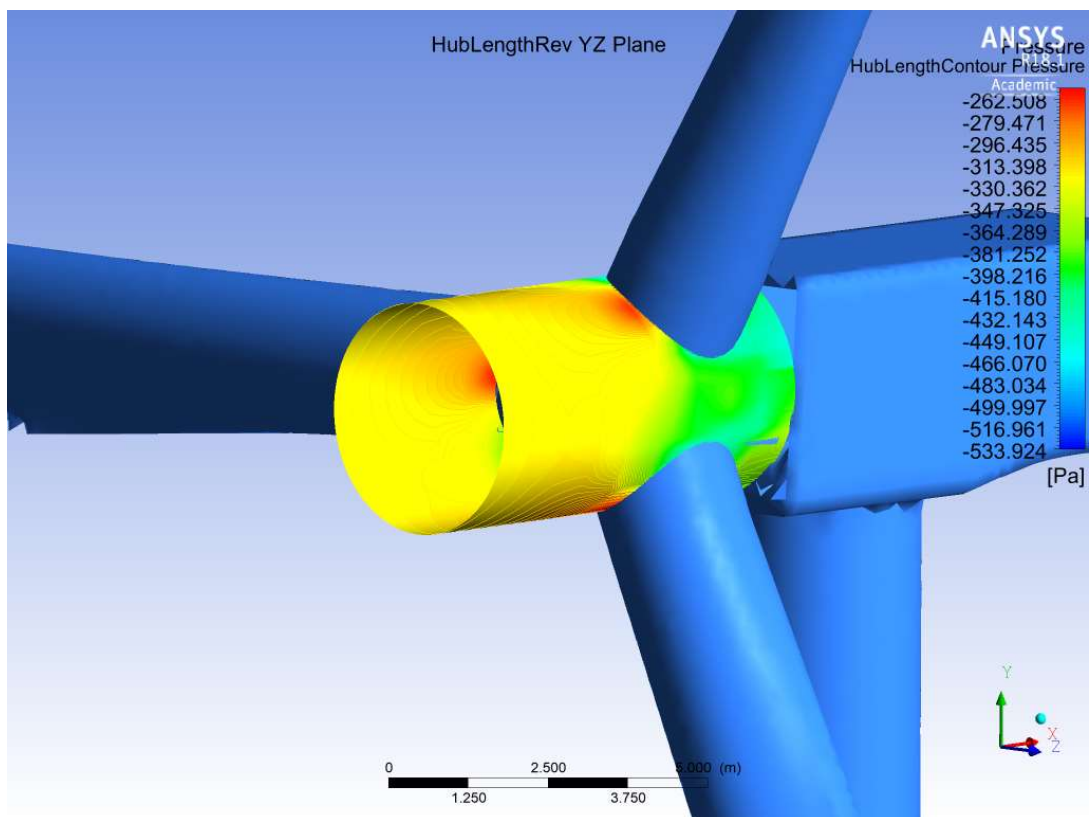


Figure 34: Pressure over Cylindrical Surface at Spinner from Simulation [26]

## 5. Discussion

### 5.1 Velocity Decrease and Air Flow Behaviour

When reviewing the figures and data from post-processing as done in chapter 4.2 “Plausibility of the Experimental Data”, the simulations appears to be plausible concerning the air flow behaviour over the spinner’s surface as well as comparing how pressure and velocity develop with the flow. However, two results are particularly striking: the insufficient power generation and the decrease of velocity that can be observed in front of the spinner for each of the three wind profiles and the respective wind velocities. Although some decrease can be expected when observing an obstacle in a flow field, the magnitude of the decrease was unexpected and will be investigated further.

#### 5.1.1 Velocity Decrease

To investigate the velocity’s decrease further and to observe whether it is located only in front of the spinner, the iSpin poly line of sensor one is elongated to capture the behaviour of the velocity from the inlet to the WT as shown in figure 35.

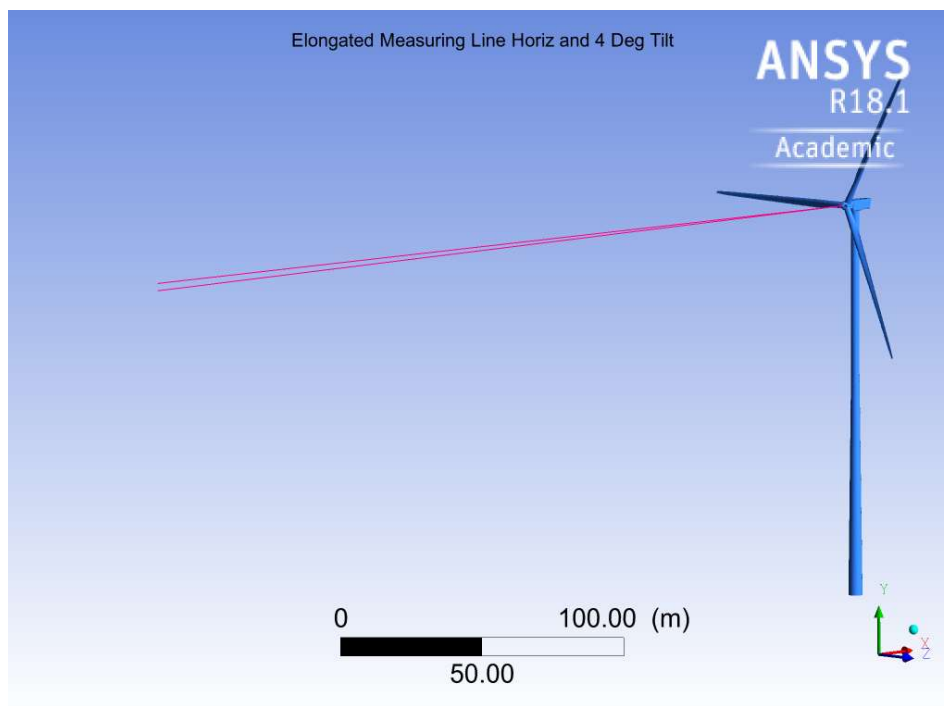


**Figure 35: Elongated Measuring Line for Horizontal Axis and 4 Degree Tilted Rotational Axis from Post-Processing [26]**

The diagram displayed in figure 36 shows the decrease in velocity along the horizontal and the tilted elongated poly lines for the logarithmic wind profile. The decrease starts at roughly 150 m before the spinner and decreases from 12 m to about 5.5 m/s.

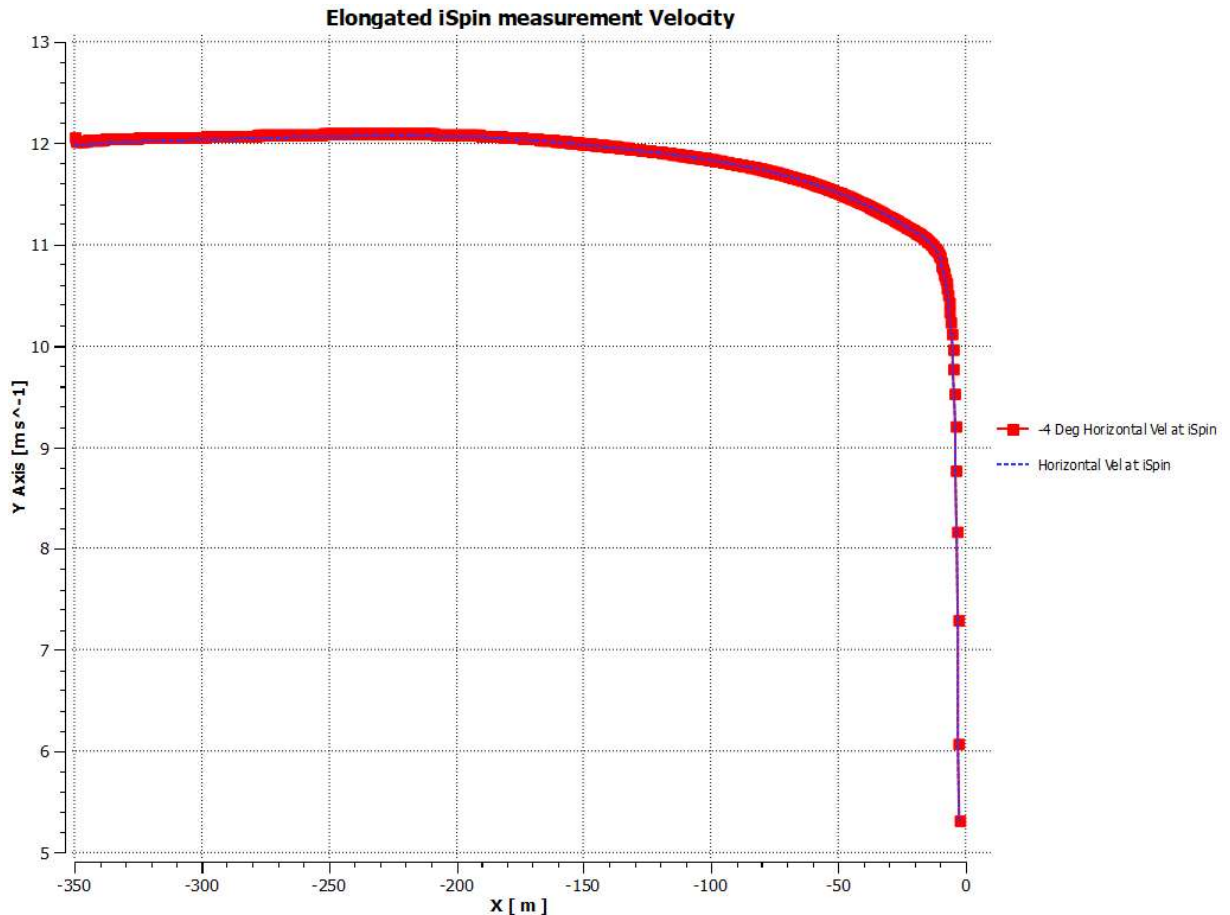


**Figure 36: Velocity Decrease along Elongated iSpin Poly Line from Post-Processing for the Logarithmic Wind Profile 12 m/s [26]**

The velocity decrease of the block profile and the wind profile with inclination angle are similar to the logarithmic wind profile case in figure 36, as the difference is neglectable only the logarithmic wind profile was displayed in this thesis. Only the logarithmic wind profile with inclination angle varies slightly as it decreases to 5.8 m/s, instead of 5.5 m/s. Although the results for the velocity decrease across the three flow profiles are similar, the decrease behaviour changes when the inlet velocity is changed to 4 m/s and 16 m/s. Figures 37 and 38 show the logarithmic wind profile for 4 and 16 m/s.

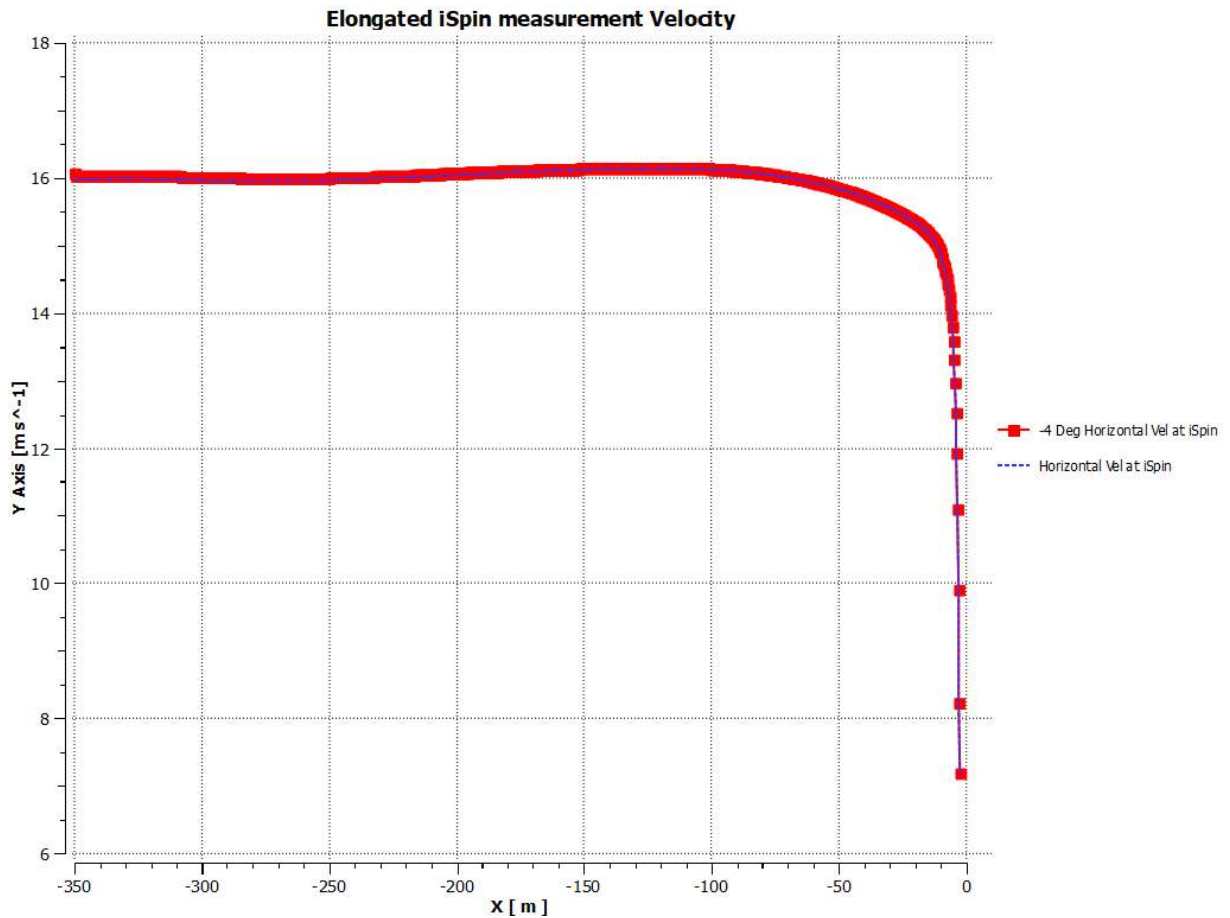


**Figure 37: Velocity Decrease along Elongated iSpin Poly Line from Post-Processing for the Logarithmic Wind Profile 16 m/s [26]**

The velocity decrease for 16 m/s seems to rise slightly at 150 m distance to the WT before the velocity starts to decrease rapidly, 50 m in front of the turbine.

The curve in figure 38 shows the velocity decrease for 4 m/s. The 4 m/s velocity slope for the three wind profile cases also differs from the slopes seen for 12 m/s and 16 m/s. The velocity starts to drop at 250 m with a more gradual slope as seen for 12 and 16 m/s. At 35 m it increases before dropping at around 10 m to its final value of 1.5 m/s just in front of the turbine.

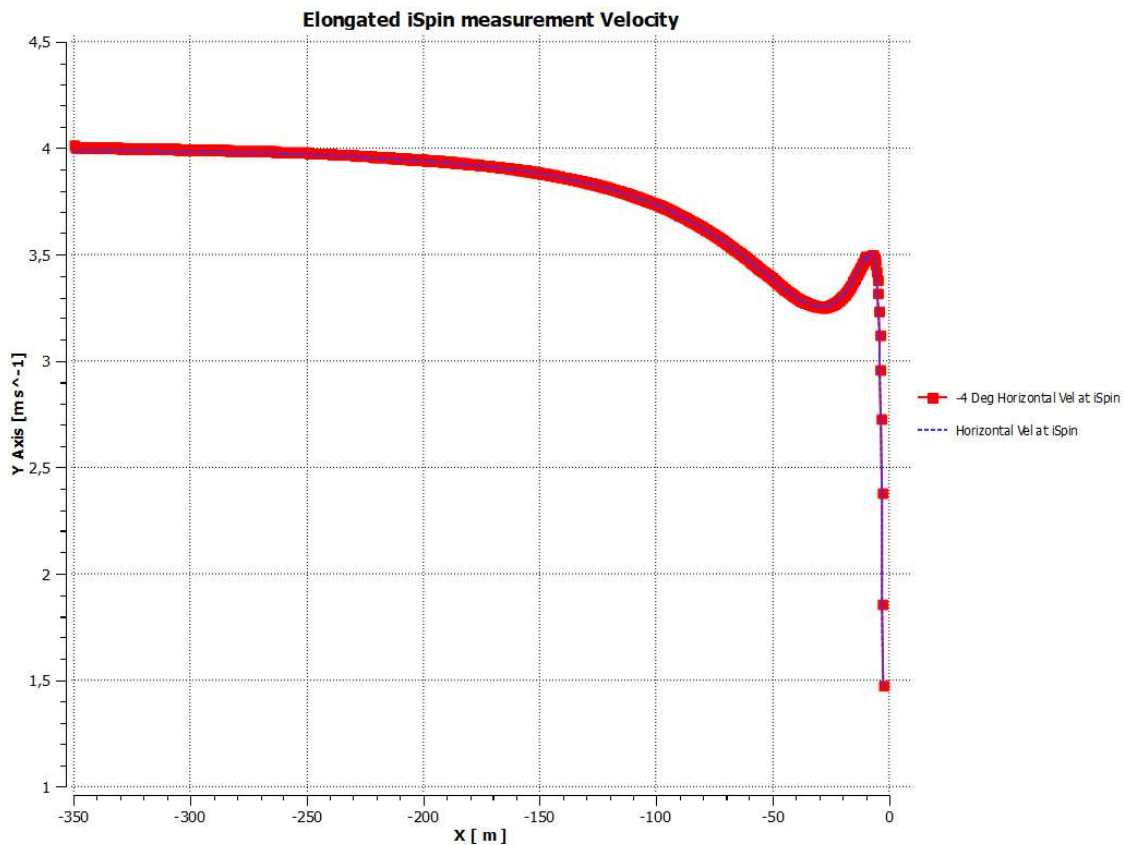


**Figure 38: Velocity Decrease along Elongated iSpin Poly Line from Post-Processing for the Logarithmic Wind Profile 4 m/s [26]**

Since the simulations for 4 m/s are, except for the inlet velocity, identical to the simulations with 12 and 16 m/s, the geometry and boundary conditions cannot be responsible for the behaviour. A possible explanation for the velocity decrease and the different slopes for the three velocity cases could be the power carried by the wind. As the air column in front of the turbine is moved with 4, 12 and 16 m/s, the wind has a different energy level. The wind power is proportional to the wind velocity to the power of three, therefore the 4 m/s case will experience a stronger influence of the wind turbine as an obstacle, than the cases with 12 and 16 m/s.

For further investigation into the velocity decrease, circular planes, or check disks, as shown in figure 39 are positioned in increasing distance from the WT to the inlet. These check disks will provide additional information on whether the decrease is localized for the elongated poly lines or whether the disks also show the decrease. Using the average over surface function from CFD-POST provides the mean velocity over each check disk. If the velocity decrease is only visible at the elongated poly line the mean should not change significantly.

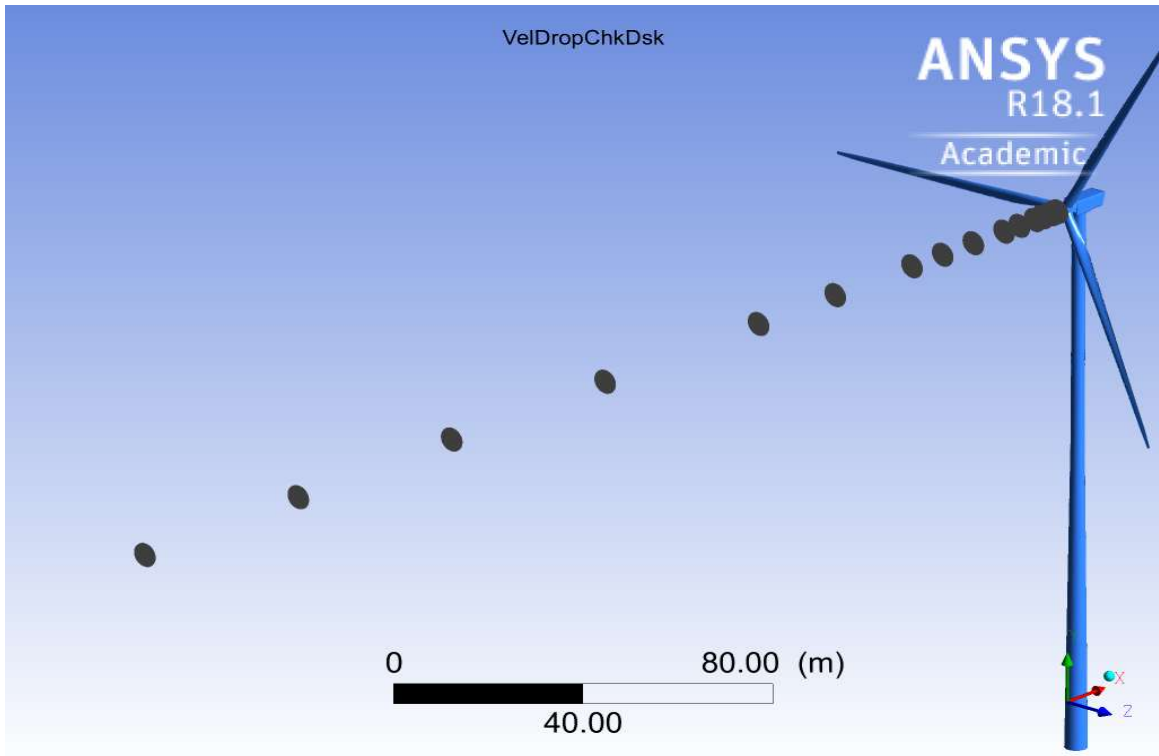


Figure 39: Velocity Decrease Check Disks from Post Processing [26]

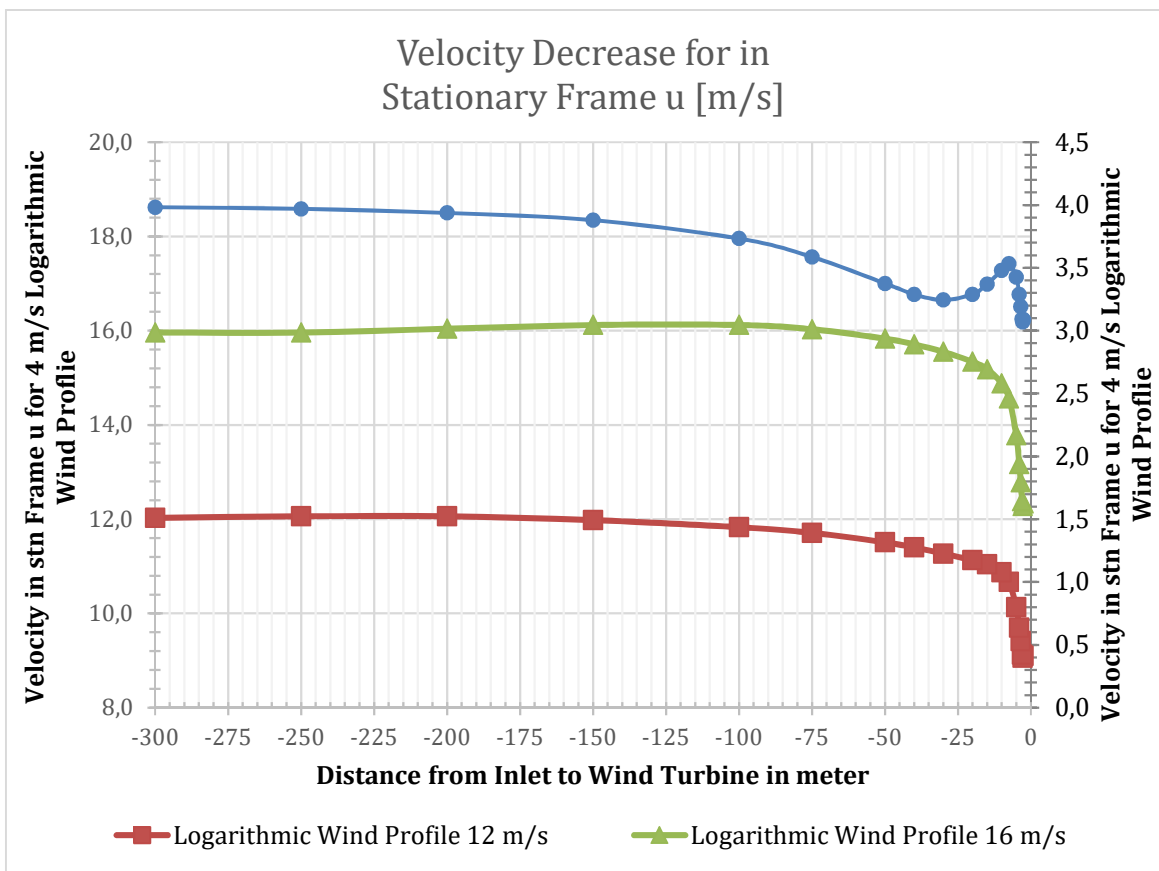


Figure 40: Diagram of Velocity Drop Check Disks [25]

Figure 40 shows the resulting average velocities from the check disks positioned in front of the turbine. The analysis of the velocities with the help of the check disks shows a similar velocity decrease to the one which could be observed with the help of the elongated poly lines. The final velocities, observed with the check disks, is for all three wind profiles 2 m/s higher than the final values from the elongated poly lines. This can be explained with the diameter of the check disks. As they are of a greater diameter than the spinner, the areas between the blades are considered as well, therefore the flow encounters less resistance and the velocity is greater. Since the spinner is a constant obstacle, it slows the air flow continuously, resulting in the lower velocities measured by the elongated poly lines directly in front of the spinner.

The magnitude of the decrease in velocity was surprising. As has been shown, the elongated poly lines delivered a slightly misleading result. When observing the same decrease with the check disk, the slope appears to be similar but the decrease in velocity is put into perspective, as flow between the rotor blades is considered as well.

## 5.1.2 Air Flow Behaviour

Figure 31 in chapter 4.3.3 “Mass Flow Behaviour in Front of the Wind Turbine” shows the velocity distribution over the swept area by the iSpin sensors. Interestingly, the velocity is very low in front of the rotor blade at the position of 120 degree. This could be due to the tilt of the rotational axis: acting as a shield for the upper half of the spinner, the nose might reduce the air flow in that direction. Another explanation for the lower wind speeds on the right side of the spinner’s nose might be a slight misalignment towards the incoming flow. The misalignment could be linked with the rotation during the creation of the WT’s geometry in MATLAB. As this was supposed to be an alignment rotation to match the x-axes of the turbine and the coordinated frame and due to the lack of the exact angle, which could not be determined, a small error in alignment may still be present.

To investigate this theory, another simulation is run in which the rotor is rotated by 180 degrees to check whether this effect is connected to the symmetry of the WT’s geometry or whether it is connected to the model itself. As figure 41 shows, the velocity distribution for the rotated WT looks very similar to the results seen in figure 31.

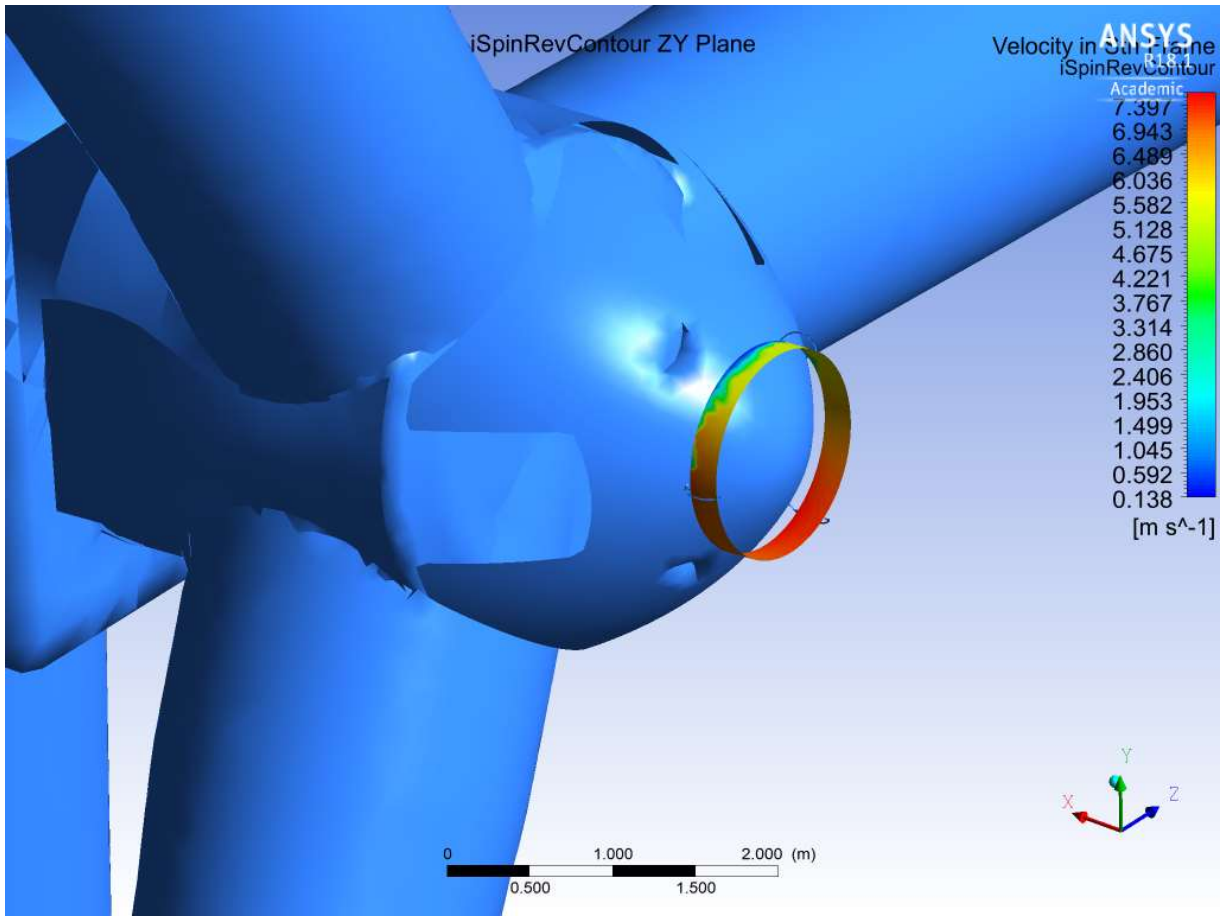


**Figure 41: Velocity in Stationary Frame at iSpin Position from Simulation with Rotated Blade [25]**

If compared directly, we see that a similar low wind speed effect occurs just above the spinner's nose. The left spinner in figure 42 is the rotated spinner from figure 41 while the right spinner is the original one from the logarithmic wind profile run at 12 m/s.

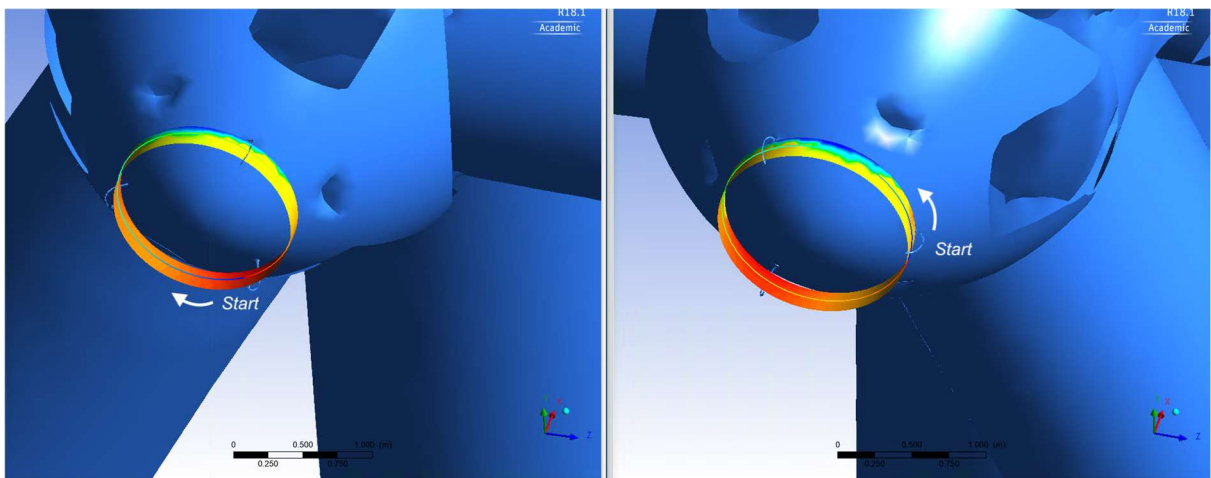


**Figure 42: Rotated and Original Spinner Comparison of the Sensor Path Surface [26]**

The area of low velocities seems less pronounced for the rotated WT in figure 42, But when comparing the rotated WT in figure 41 to the regular WT in figure 42 on the right, the effect looks similar. Therefore, it can be assumed that the WT's geometry is symmetrical, and the low wind speed effect is an issue connected to the WT itself.

The diagram in figure 43 shows the velocity against the angle of rotation with a poly line located in the sensor path's middle. Against the expectation that three peaks in velocity of similar heights could be observed, the velocity curve has one very prominent peak. A smaller peak can be seen at a distance of 120 degree from the high peak. Surprisingly, when progressing another 120 degree to 265 degree, a dip in the velocity is observed. A similar velocity curve is observed when plotting the velocity over rotational angle for the simulation with the rotated geometry. Unfortunately, the poly line for the rotated geometry does not begin at the same starting point as the poly line of the regular WT does. Nor does it progress in the same direction. To display both velocity curves for the regular and the rotated geometry, and to simplify comparability, the data was plotted in reverse. A small offset of about 25 degrees remains, which is caused by the different starting points of the poly lines. As the poly line is generated by CFD-Post at a user specified position, the direction and starting point cannot be changed.

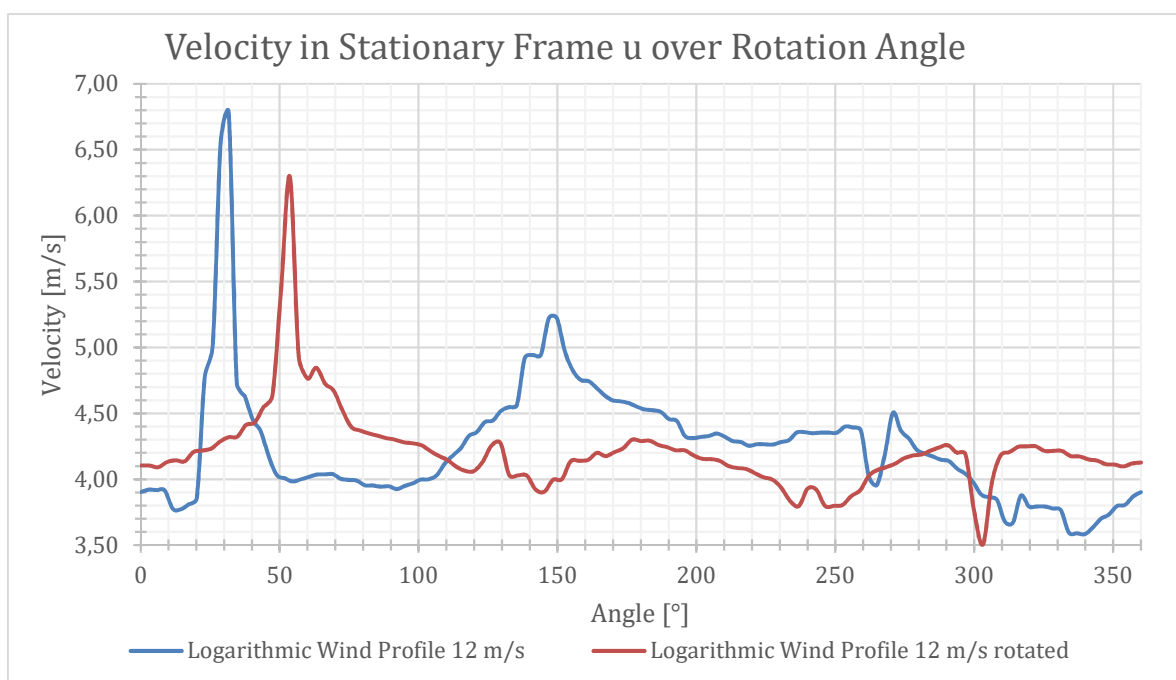


**Figure 43: Velocity in Stationary Frame u over Rotation Angle from Simulation [25]**

In addition to the reverse poly line, CFD-Post recorded less samples for the poly line in the rotated geometry compared to the regular geometry's poly line, which can also not be adjusted. As the algorithm behind CFD-Post's sampling is unknown and cannot be adjusted, there might be some higher values that have not been captured.

**Table 4: 10 Hz Data from iSpin Measurements at Wonnegau [25]**

iSpin 1	iSpin 2	iSpin 3	Time [s]	Angle [°]
10.13	11.19	8.45	0.10	7.31
10.40	10.09	7.97	0.20	14.65
10.83	9.45	8.20	0.30	22.14
11.43	9.70	8.39	0.40	29.67
11.19	10.35	9.84	0.50	37.28
10.65	8.93	10.12	0.60	44.81
10.21	8.50	9.62	0.70	52.43
9.95	9.11	10.4	0.80	60.03
10.42	8.99	10.87	0.90	67.64
10.52	9.36	10.94	1.00	75.18
10.38	9.25	11.05	1.10	82.67
10.66	9.57	11.39	1.20	90.19
10.24	10.09	11.06	1.30	97.55
9.94	10.28	10.65	1.40	104.83
9.98	10.44	10.86	1.50	111.88
9.84	10.50	10.78	1.60	118.91
9.49	9.95	10.66	1.70	125.82
9.32	10.26	10.81	1.80	132.72
9.05	10.35	11.00	1.90	139.64
8.51	10.36	10.69	2.00	146.62
8.40	10.46	10.32	2.10	153.67
8.30	10.26	10.40	2.20	160.66
8.73	10.78	10.21	2.30	167.73
8.78	10.68	9.46	2.40	174.84
8.84	10.61	9.49	2.50	182.20
8.80	11.06	9.47	2.60	189.73
9.04	11.03	9.35	2.70	197.49
9.58	11.04	9.34	2.80	205.40
10.31	11.00	9.34	2.90	213.36
10.20	10.89	9.38	3.00	221.32
10.50	10.73	9.20	3.10	229.28
10.42	10.79	9.06	3.20	237.31
10.43	10.63	8.97	3.30	245.33
10.83	10.41	9.25	3.40	253.32
10.51	9.99	9.38	3.50	261.17
10.55	9.98	9.28	3.60	269.04
10.69	9.99	9.58	3.70	276.76
11.13	9.36	9.14	3.80	284.43
11.41	10.46	10.37	3.90	291.98
10.80	10.35	10.26	4.00	299.56
10.86	9.17	10.15	4.10	307.10
10.84	8.78	10.10	4.20	314.65
10.74	8.51	9.96	4.30	322.19
10.83	8.51	10.11	4.40	329.69
10.65	8.30	10.70	4.50	337.19
10.84	7.75	10.75	4.60	344.61
10.53	7.57	10.57	4.70	352.13
10.75	7.41	11.13	4.80	359.64

As an addition to the rotated geometry and to the diagram “Velocity in Stationary Frame  $u$  over Rotation Angle”, the 10 Hz data from the iSpin sensors, as listed in table 4, are also plotted against the angle of rotation to see if a comparable behaviour can be observed. Since the 10 Hz data was not yet observed, and only 10 minute averages have been used, the behaviour of the iSpin measurement during rotation is of interest. As already mentioned in chapter 1.3.2 “Description of the iSpin Sensors”, during one rotation 48 measurements are taken per sensor. As the count chart for figure two was between 114 and 125, the cumulated measurements of three sensors should provide a sample rate equivalent to the chart count from post-processing.

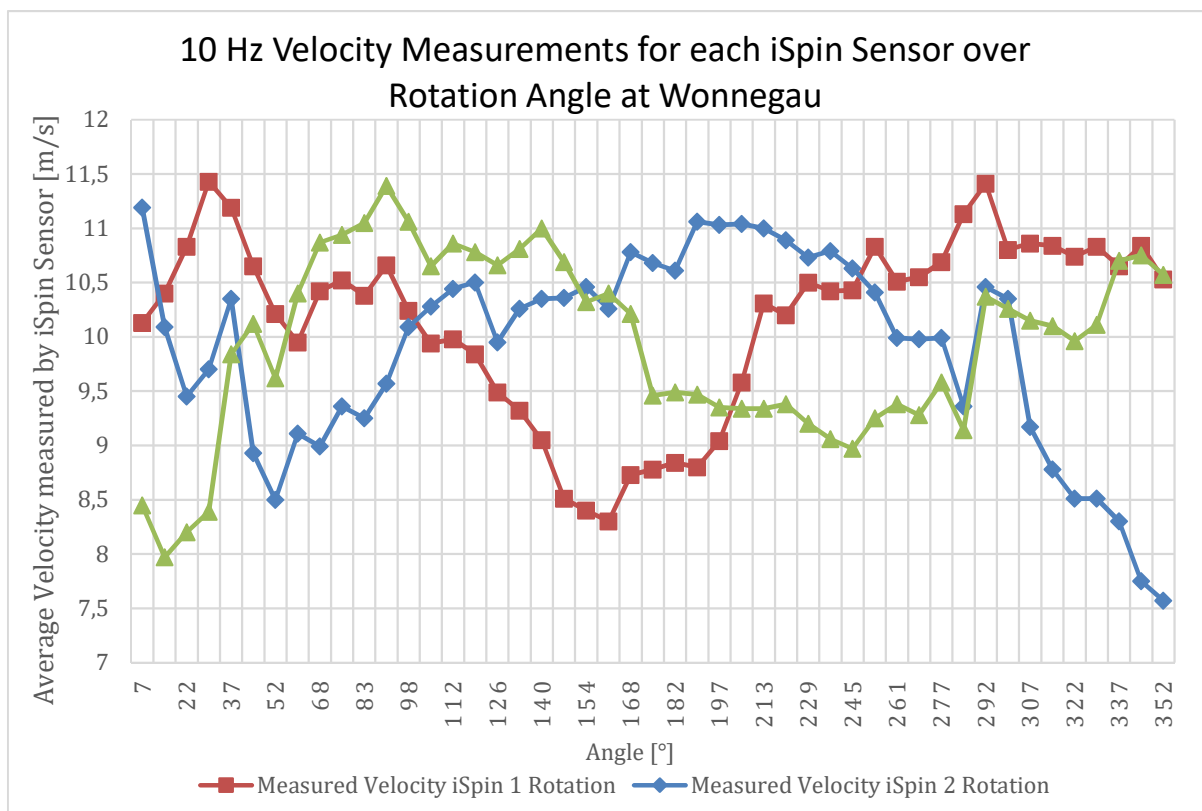


**Figure 44: 10 Hz Velocity Measurement for Individual iSpin Sensors over Rotation Angle at Wonnegau [25]**

The curves displayed in figure 44 represent the individual iSpin sensors’ velocity measurements over the rotation angle. The angles are respective to each sensors path and do not have the 120 degrees offset, which the sensors usually have towards each other. Figure 44 supports the simulation and the results presented in figure 43, as it visualizes the difference in velocity experienced during one rotation. Although it does not show the prominent peak of the simulation, a strong dip in the velocity is present.

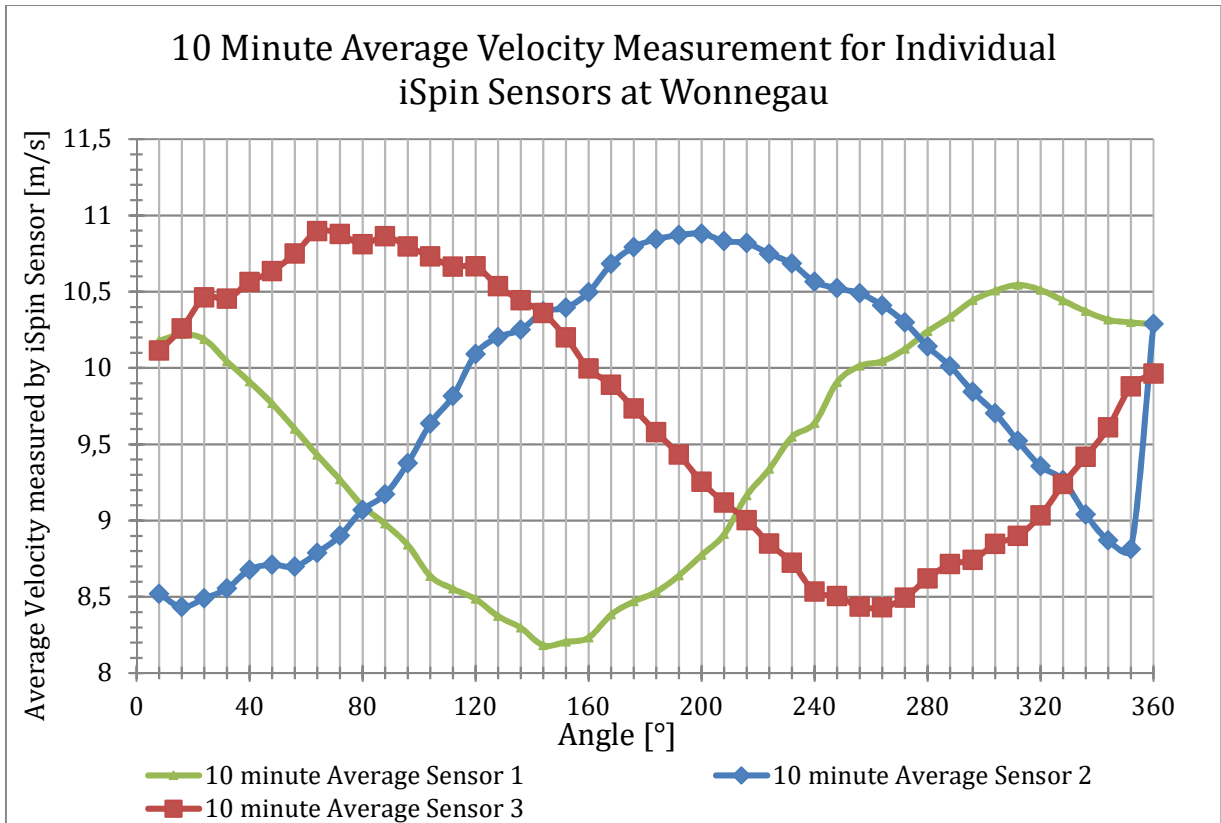


**Figure 45: 10 Minute Average Velocity Measurement for Individual iSpin Sensors at Wonnegau [25]**

The curves presented in figure 45 show the 10 minute velocity averages from the individual sensors indicating that each sensor in fact measures the same value as the others over time as explained during the description of the iSpin sensors in chapter 1.3.2.

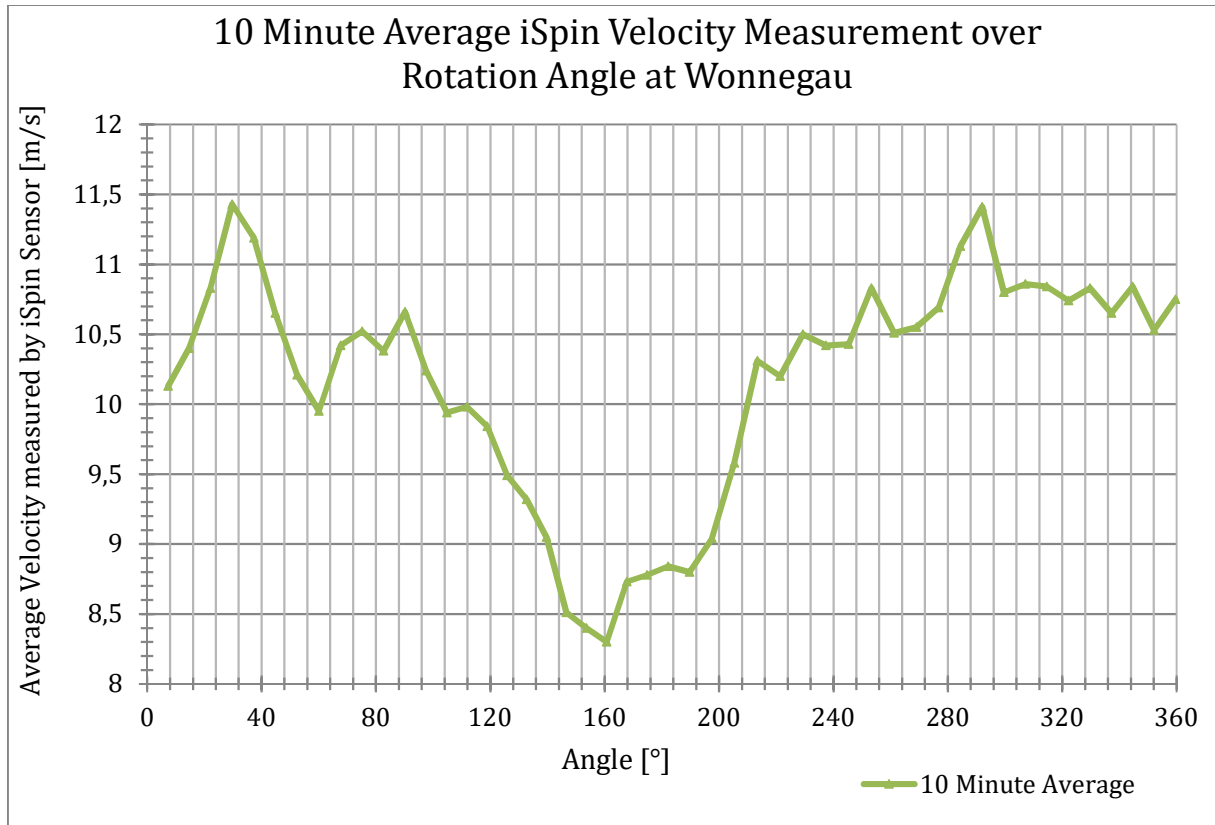


**Figure 46: Average iSpin Velocity Measurement over Rotation Angle at Wonnegau [25]**

The diagram in Figure 46 visualizes the average of the three sensors over the rotation angle. The curve shows a similar behaviour to the one observed in figure 44 and the 43 for the individual sensors, showing one slightly higher peak and one large dip in the measured velocity. Therefore, the iSpin sensors appear to measure similar values over one rotation, as the simulated sensors.

## 5.2 Test and Reference Simulation with the WT from the DOWEC Study Project

A test and reference simulation for the logarithmic wind profile was run with the rotor blade's geometry down scaled from the DOWEC study project and adjusted to the WT's dimensions. It was a first attempt on implementing the logarithmic wind profile on the inlet velocity. As the study project yielded good results, in simulating a matching turbine power output to the nominal output, the results of the test run may be used as a reference for the turbines behaviour.

For simplicity the geometry of the DOWEC study project is kept very simple and the rotational axis is not tilted backwards as for the GE WT. Further, the DOWEC WT rotates faster than the GE WT and experiences a higher velocity at hub height as the rotational axis is at a height of 157.4 m. The spinner is shaped as half a sphere and no recesses or openings are present. Therefore, the airflow over the spinner should be almost symmetrical except for the tower influence. The uniform flow distribution over the spinner and the stagnation point are pictured in figure 47.

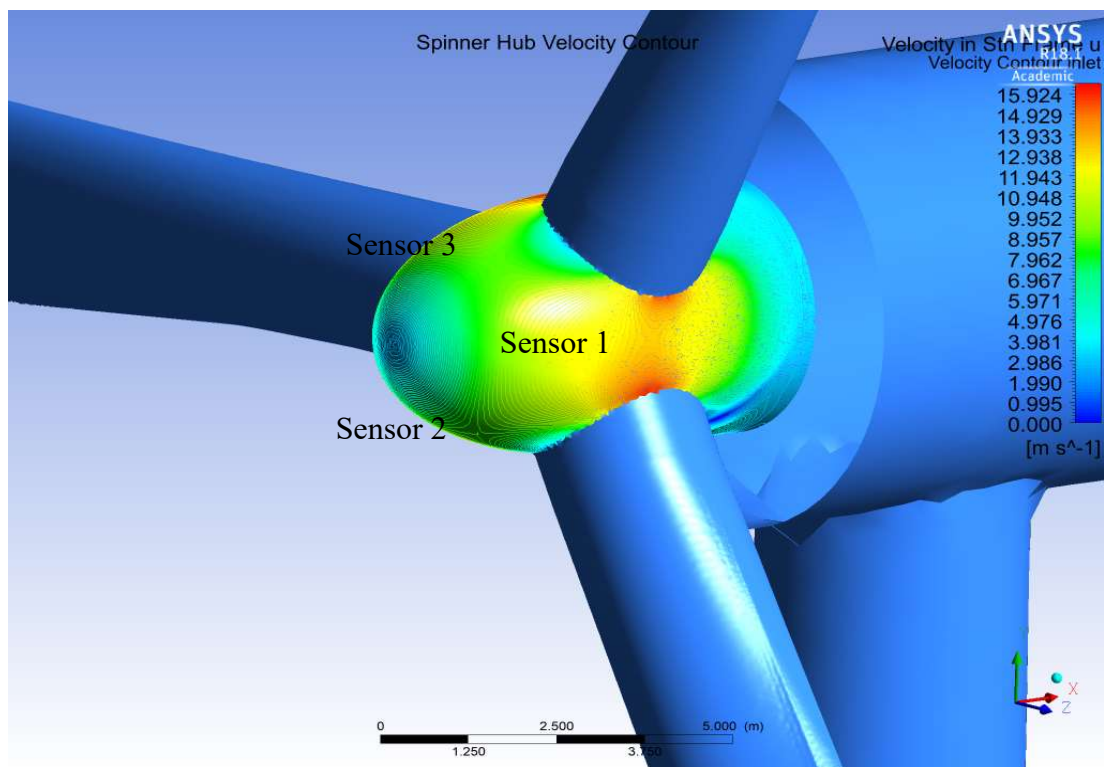
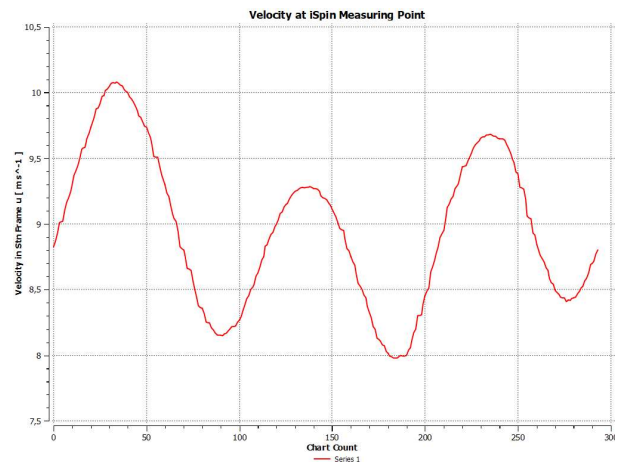
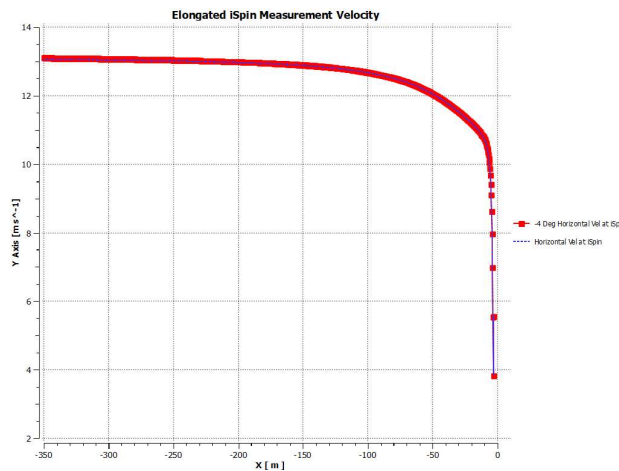


Figure 47: Velocity over Spinner Surface in Stationary Frame u from Simulation for the DOWEC WT [25]



**Figure 48: Velocity Decrease along Elongated iSpin Poly Line from Post Processing for Wind Profile 12 m/s DOWEC WT [26]**

**Figure 49: Velocity in Stationary Frame  $u$  over Angle from Simulation for the DOWEC WT [26]**

The decrease of velocity as visualized in figure 48 shows the same behaviour as for the GE WT. Although at first glance the very low value at the spinner surprises. The low value results from the check disk nearest to the spinner. Since the DOWEC spinner is larger, the check disk is partly engulfed by the geometry, therefore the average mass flow over the disk is lower.

Figure 49 visualises the velocity over the sensor path swept by the iSpin sensors. As expected the velocity over the iSpin sensor path shows a symmetrical pattern, where the iSpin sensor at position one experiences the highest velocity. This is due to the influence of the tower and the blade below iSpin Sensor one, which form a broad obstacle. The additional airflow is directed past sensor one and thus increases the measured velocity. As some of the airflow was displaced by the tower towards sensor one, the velocity experienced by sensor two is the lowest. Sensor three experiences uninterrupted flow and its value lies in between sensor one and two.

The k-factor for the test turbine experiences some influence of the large nacelle, which was not fitted to the smaller spinner and to the smaller blades.

The power generation for the DOWEC WT is around 800 kW. Although the nominal power for the adapted DOWEC geometry is unknown, it is safe to assume that with a fitting blade design the power output would be greater. The difference to the GE WT can be explained by the higher velocity, the more refined mesh and the fact that the rotor blades are not conical. Therefore, the blades sweep a slightly larger area and can generate more energy.

As the reference geometry shows similar velocity behaviour in front of the spinner and over the sensor path, plotted against the rotational angle to the WT geometry's behaviour discussed in chapter 5.1.2, the spinner nose does appear to shield some of the wind, causing the area of low wind speed.

## 5.3 Logarithmic Wind Profile

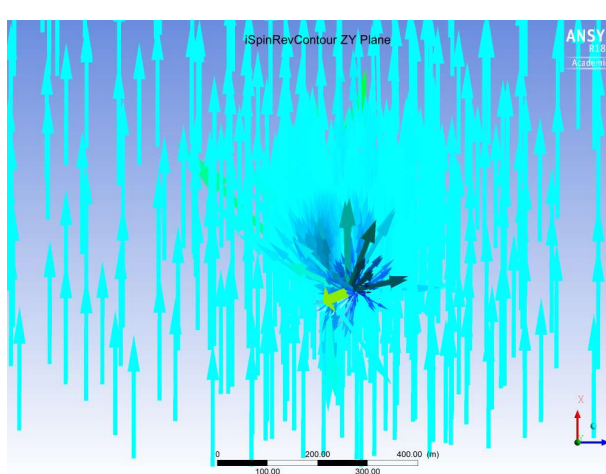


**Figure 50: Wind Profile Inlet Vector from Simulation [26]**

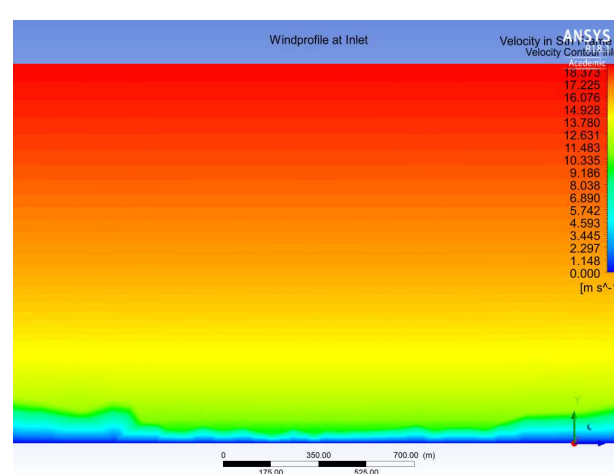


**Figure 51: Logarithmic Wind Profile at Inlet from Simulation [26]**

Figure 50 shows the inlet vectors across the xz-plane. As the inclination angle is set to zero, the vectors are in plane with the x-axis and are in a direct flow towards the WT. When the air flow hits the WT, parts of the flow are deflected, sped up or slowed down. The deflection and velocity change is visible through the vectors as they vary in length and direction. Figure 51 shows the velocity increase with height, due to the implemented logarithmic wind profile. As the mesh near the edges is slightly rougher, some ripples occur in the layer of 0 to 9 m/s which dissolve with increasing height. The distortion from the ripples and their effect on the simulation can be considered as relatively low, as fewer ripples appear in the centre of the wind profile. Therefore, the effects of the distortions are neglected in this thesis.

### 5.3.1 k-Factor for Logarithmic Wind Profile

As the k-factors are created from 10 minute average values based on the 10 Hz measurements, one data point in the met mast data considers 125 rotations. The values from the simulation provide a similar result. The steady state simulation provides a snap shot of the rotor position

during operation and the forces and stresses it experiences. Therefore, taking single values across the sensor’s path will not yield proper results. Further, as the velocities over the iSpin sensor path surface vary, the positioning of the sensors would influence the result’s outcome. Therefore, it is necessary to form an average of the measured velocities in stationary frame  $u$  over the sensor path surface, which is usually done in CFD-Post with the function Ave for average. The average function gives the arithmetic mean. As the Average function is dependent on the mesh, a result which is independent of the mesh is preferred. Due to possible inconsistencies in the mesh, the function massFlowAve is chosen, which is not biased to areas of nodal density [29].

For finer meshes the actual average between the transducers is important, therefore a spatial average should be formed using equation (2):

$$\overline{u_d}(x) = \frac{1}{x_2-x_1} * \left(\frac{1}{t_1} - \frac{1}{t_2}\right) * 0.5 \int_{x_1}^{x_2} x dx \quad (13)$$

to determine the average velocity along the sensor path in post-processing.

As anemometers only measure the velocity parallel to the sensor path, which in this case is the rotational axis, the incoming flow in x-direction for the WT’s geometry coordinate frame, or velocity in stationary frame  $u$  for the velocities in the simulation, needs to be adapted to the four degree tilt. To adapt the velocity in stationary frame  $u$  to the rotational axis, the flow component is divided by the cosine of 4 degrees, resulting in the air flow component parallel to the rotational axis.

Table 5 shows the measured values at the iSpin sensor position in stationary frame, for the sensor path’s surface in stationary frame and for the sensor path in stationary frame in the direction  $u$ .

**Table 5: k-Factors for Logarithmic Wind Profile [25]**

	Logarithmic Wind Profile					
	Velocity in Stationary Frame $u$	Velocity Parallel to Sensor Path	k-factor	Velocity in Stationary Frame	k-factor	Velocity at Inlet
4 m/s	1.812	1.817	0.454	2.580	0.644	4.007
12 m/s	5.074	5.086	0.423	6.516	0.542	12.020
16 m/s	6.875	6.892	0.430	8.845	0.552	16.027
Mean			0.436		0.579	
Standard Deviation			± 0.013		± 0.046	

Additionally, table 5 shows the velocity in stationary frame across the sensor path surface and its corresponding k-factor. When the post-processing was started, the k-factor was estimated with the velocity in stationary frame. The k-factor from the velocity in stationary frame matches the actual k-factor from the met mast data, see chapter 4.1 “Met Mast Data” of 0.532 perfectly. To investigate the unexpectedly good approximation despite the compromises on mesh fineness and on the fit of the blade, the previously mentioned additional simulation with cylindrical blades is initiated. This will help to appraise the influence of the blade’s geometry on the k-factor.

Since, according to ultrasonic anemometry, the iSpin measurement only considers the velocity in plane to the sensor path, the transformed velocity in stationary frame  $u$  must be considered instead of the velocity in stationary frame, therefore the k-factor described above is neglected. The k-factor, according to the iSpin measurement, is therefore  $0.436 \pm 0.013$  for the logarithmic wind profile. The k-factor for the logarithmic wind profile differs by a factor of 18.05 % from the k-factor estimated from the met mast data. Interestingly, the k-factor for 4 m/s is noticeably higher than the k-factors for the higher velocities. This might be connected to the fact that 4 m/s is the only velocity investigated in this thesis, which experiences rotor induction for this type of WT.

## 5.4 Block Profile

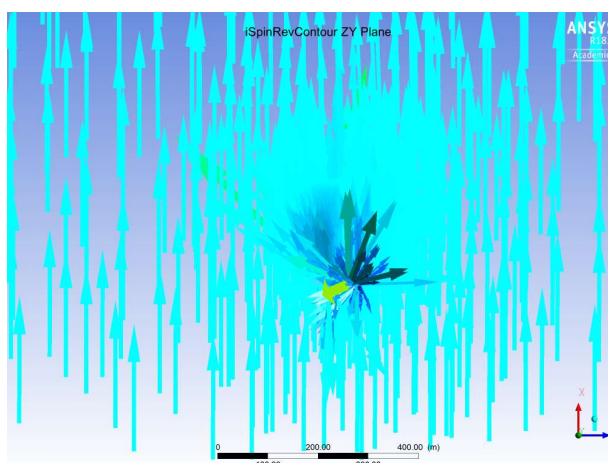


**Figure 52: Block Profile Inlet Vector with Inclination Angle  $\phi=0^\circ$  from Simulation [26]**

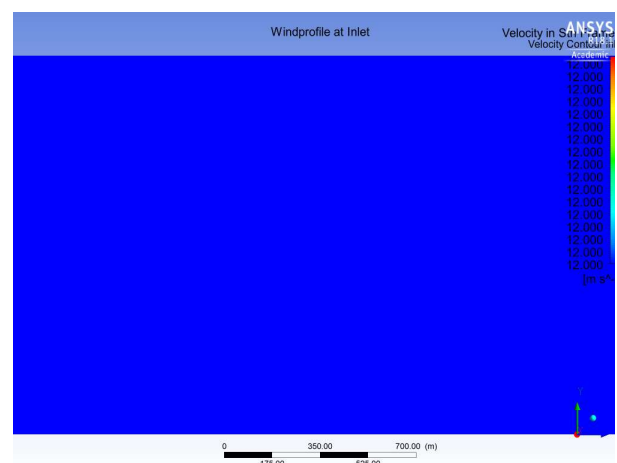


**Figure 53: Block Profile at Inlet from Simulation [26]**

Similar to what could be witnessed when examining the logarithmic wind profile, the block profile, visualized in figure 52, shows wind vectors perpendicular to the rotor area. Figure 53 on the other hand shows the xz-plane the distribution of the inlet velocity in respect to height for the block profile. As the velocity of the block profile does not vary with increasing height only, a single velocity value is plotted, represented in blue in figure 52.

Having the same velocity over the area swept by the WT could influence the velocity measured at the spinner for the block profile, as some influences of the higher velocities experienced below the rotational axis might occur compared to the lower velocities experienced with the logarithmic wind profile. Although the difference in velocity between block and logarithmic wind profile is only around 1.4 m/s from the tip of the blades at its lowest point, 79 m, to the hub at 139 m, it might still be enough to change the resulting k-factor.

### 5.4.1 k-Factor for Block Profile

**Table 6: k-Factors for Block Profile [25]**

	Block Profile					
	Velocity in Stationary Frame u	Velocity Parallel to Sensor Path	k-factor	Velocity in Stationary Frame	k-factor	Velocity at Inlet
4 m/s	1.831	1.836	0.459	2.641	0.660	4.000
12 m/s	5.039	5.051	0.421	6.485	0.540	12.000
16 m/s	6.763	6.780	0.424	8.720	0.545	16.000
Mean			0.435		0.582	
Standard Deviation			± 0.017		± 0,055	

The resulting k-factor for the block wind profile, as listed in table 6, is slightly smaller than the k-factor for the logarithmic wind profile, therefore it can be concluded that the uniform velocity distribution, which is experienced in the block profile, does not seem to have a strong influence on the k-factor. This can be explained, by the fact that the WT in the logarithmic wind profile experiences higher velocities above the hub height, thus cancelling most of the effect of higher velocities below hub height with a uniform velocity distribution.

## 5.5 Logarithmic Wind Profile with 5 Degree Inclination

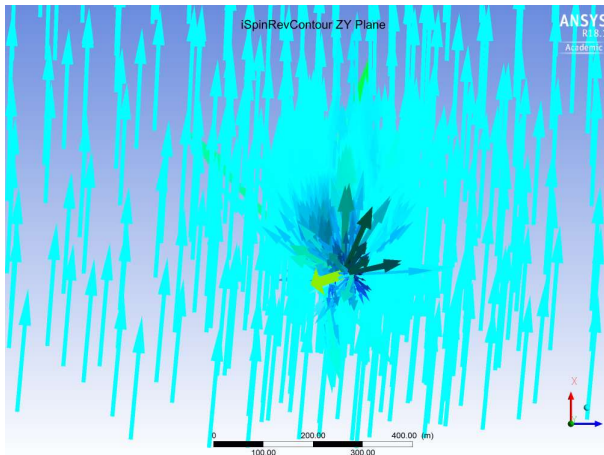


**Figure 54: Wind Profile Inlet Vector with Inclination Angle  $\phi=5^\circ$  from Simulation [25]**

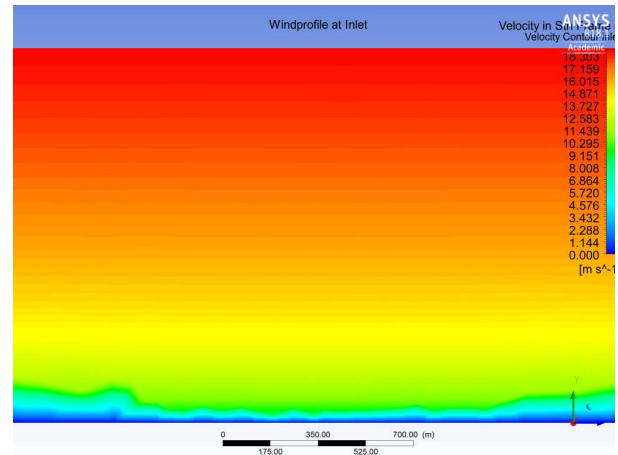


**Figure 55: Logarithmic Wind Profile with Inclination Angle at Inlet from Simulation [25]**

Figure 54 shows the inlet vectors on the xz-plane with a 5 degree inclination. The 5 degree inclination does not visibly influence the velocity distribution in respect to height when comparing the logarithmic wind profile with inclination in figure 55 to figure 51 which shows the logarithmic wind profile without inclination angle. While investigating the power generation of the geometry for the different wind profiles and velocities, the blades worked better in the inclined air flow, compared to a direct flow. This might also influence the k-factor estimation.

Further, some differences compared to the logarithmic wind profile are to be expected, as the w- or z-component of the wind increase, thus decreasing the u- or x-component. Therefore, a slight decrease in the measurements is to be expected as the iSpin sensors measure only the wind in stationary frame u.

## 5.5.1 k-Factor for Logarithmic Wind Profile with 5 Degree Inclination

**Table 7: k-Factors for Logarithmic Wind Profile with 5 Degree Inclination Angle [25]**

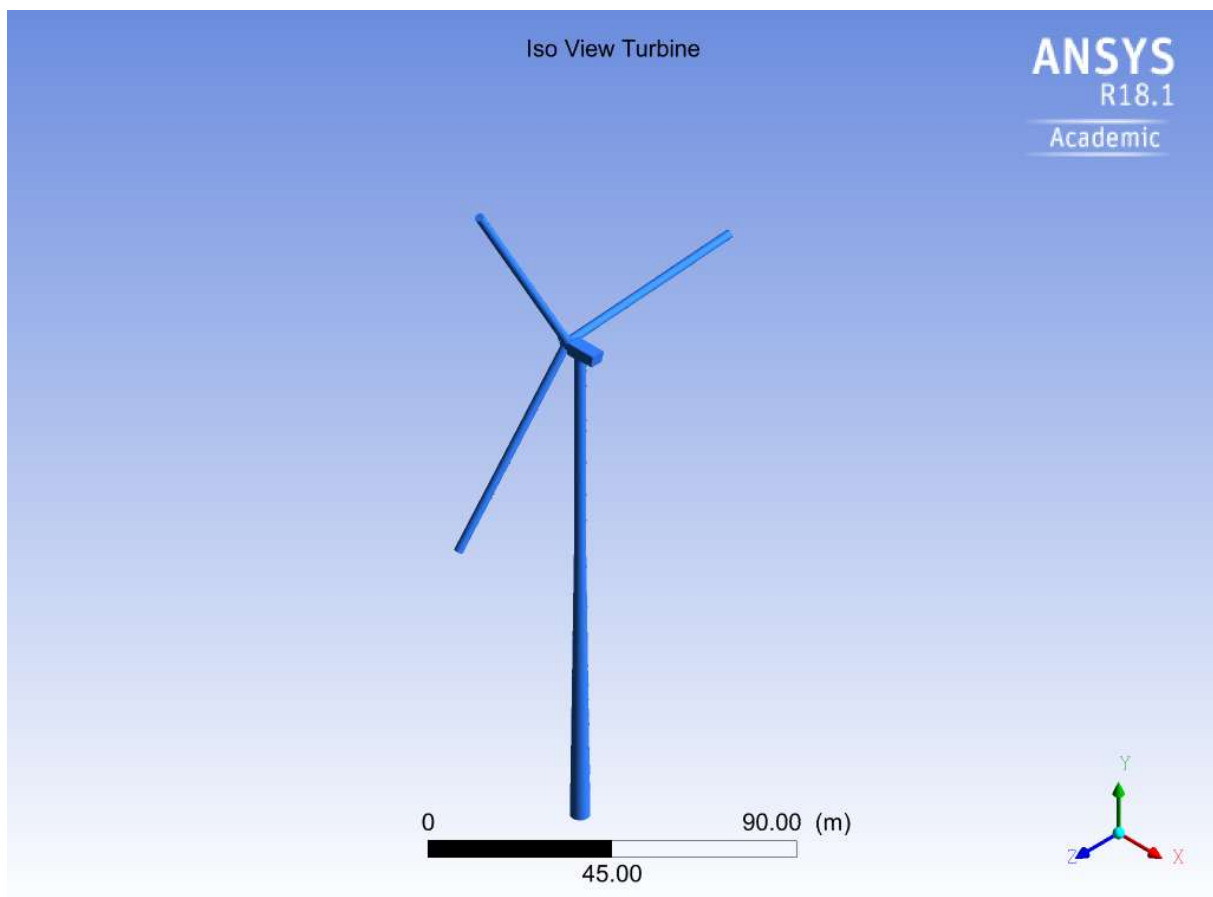
Logarithmic Wind Profile with 5 Degree Inclination Angle						
	Velocity in Stationary Frame u	Velocity Parallel to Sensor Path	k-factor	Velocity in Stationary Frame	k-factor	Velocity at Inlet
4 m/s	1.871	1.875	0.470	2.810	0.704	3.991
12 m/s	5.040	5.052	0.422	6.498	0.543	11.974
16 m/s	6.725	6.741	0.422	8.619	0.540	15.966
Mean			0.438		0.596	
Standard Deviation			± 0.022		± 0.077	

Table 7 displays the measured velocities and the respectively calculated k-factors for the logarithmic wind profile with inclination angle. The measured difference in velocities compared to the logarithmic wind profile without inclination is less significant than expected. Also, the k-factor is slightly higher compared to the logarithmic profile but still varies from the met mast k-factor by 17,67 %. Due to the lower inlet velocity, the higher k-factor can be explained, as it is formed by the ratio of the two velocities.

## 5.6 Influence of Blades and Spinner on the k-Factor

As the k-factors for the velocity in stationary frame have yielded good results despite the compromises made on mesh fineness and on the blades, the question arose in how far the design of the rotor blade influences the k-factor, or whether the spinner geometry is more influential.

As the rotor blade geometry changes, the old mesh needs to be replaced by a new one. To maintain comparability between the simulations with the DOWEC blades and the cylinder, the node count for the mesh should be close to the initial node count.



**Figure 56: Iso View of the WT with Cylindrical Blades [26]**

Figure 56 shows the resulting cylindrical blades, implemented in the WT's geometry. For the initial conditions, the logarithmic wind profile without inclination and an inlet velocity of 12 m/s was selected, as the average k-factor for the logarithmic wind profile is almost identical to the average k-factor for all cases. The inlet velocity was selected, as it is in between 4 and 16 m/s. No further changes were made.

**Table 8: Influence of Blade Shape on the k-Factor [25]**

	Logarithmic Wind Profile 12 [m/s]					
Cylinder	5.301 m/s	5.314 m/s	0.442	6.794 m/s	0.565	12.021
DOWEC	5.074 m/s	5.086 m/s	0.423	6.516 m/s	0.542	12.020
Difference			4.479%			4.263%

The influence of the blade shape on the k-factor is analysed in table 8. The difference on the k-factor between the DOWEC and the cylindrical blade in this case is 4.479 %. Therefore, the influence of the blade appears less significant than the shape of the spinner and the blade roots. The influence of spinner and blade roots is also mentioned in the paper by G. Demurtas ‘New method to calibrate a spinner anemometer’, which states that the k-factor is most influenced by the spinner shape and the blade roots [9, p.1].

## 5.7 k-Factor Estimate for all Cases

**Table 9: k-Factor Estimation of all Wind Profiles [25]**

	k-Factor over all Wind Profiles	
	k-Factor Mean [-]	Standard Deviation [-]
Logarithmic Wind Profile	0.436	± 0.013
Block Profile	0.435	± 0.017
Logarithmic Wind Profile with Inclination Angle of 5°	0.438	± 0.022
	0.436	±0.018

The simulations conducted for this thesis allow to estimate the k-factor for the WT type investigated. When observing the estimated k-factor for the three wind profiles with a wind velocity of 12 m/s, the k-factor does not vary much and remains around 0.422. The k-factors estimated for the three wind profiles with 16 m/s as inlet velocity, vary slightly more, from 0.422 to 0.430. But for 4 m/s the estimated k-factor’s variation is even more pronounced, as they vary from 0.454 to 0.470. This might also be connected to the unexpected slope discussed in chapter 5.1.1.

Table 9 lists the k-factors from the previous chapters and their average. The average k-factor formed over all of the previously discussed wind profiles and velocities, is  $0.436 \pm 0.018$ , this is 18.05 % below the k-factor from the met mast data estimation of 0.532.

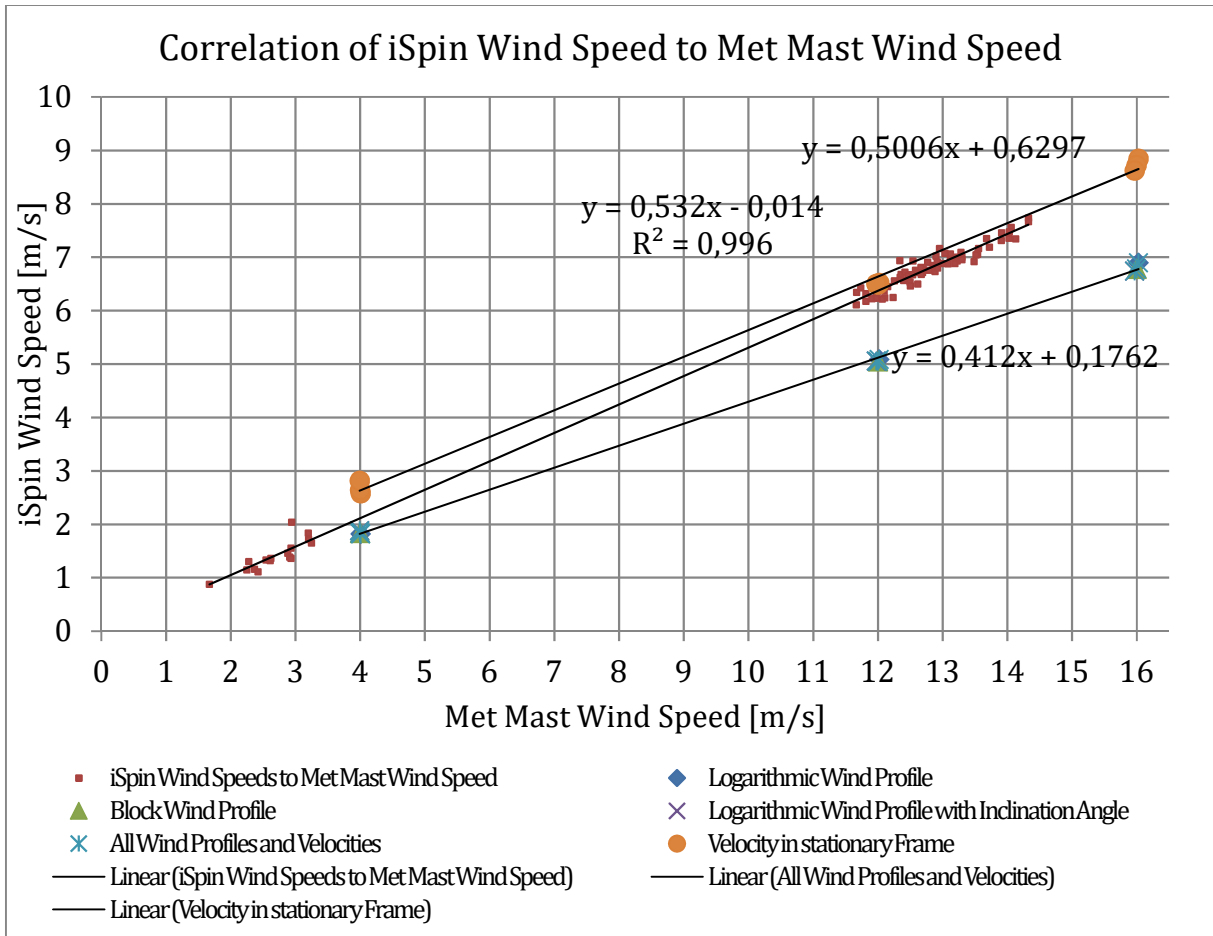


**Figure 57: k-Factor from Met Mast Data and k-Factor Estimate from Simulations [25]**

Figure 57 shows the met mast data and the corresponding linear regression line as well as the estimated k-factors from the simulation with the corresponding linear regression line. The values simulated for the velocity in stationary frame are also plotted, and they seem to have a slight offset to the k-factor of the met mast.

## 6. Conclusion

The iSpin anemometer is a relatively new method of determining wind velocity, direction and temperature. Since the iSpin sensors are installed on the spinner, unlike conventional anemometers, which are installed behind the rotor blades, the air flow they experience is undisturbed by the rotor blades. When the iSpin sensors are installed they need to be calibrated to accommodate to the wind turbine's geometry; this will ensure that their velocity measurements are correct. For the calibration of the sensors the calibration factors  $k_1$  and  $k_\alpha$  must be determined. The calibration is usually realized during operation or while the turbine is at a standstill. A meteorological measurement tower provides the actual wind speed and direction at three to four rotor diameters distance, in front of the wind turbine. The erection of the measurement tower and the usual calibration process are expensive and take time. To reduce costs, simulating the geometry in a flow field with computational fluid dynamics is investigated as an alternative for determining the  $k_1$ -factor.

During this thesis, the geometry for a GE 2.5 -120 wind turbine was reconstructed from a point cloud. This point cloud was generated via photogrammetry from pictures of a wind turbine taken by a drone. The point cloud is formatted with a MATLAB script, allowing ANSYS ICEM to import the formatted point cloud to generate the wind turbine's geometry. As the drone did not record the rotor blades, a substitute blade was incorporated, which stems from a study project, investigating a blade from the DOWEC project was scaled down from 129 m in diameter to fit the wind turbine dimension specifications of 120 m in diameter. The GE wind turbine geometry was used as a basis for a series of simulations. The simulations include three different wind profiles: a block profile with a constant velocity over height and two logarithmic wind profiles whose velocity increase with height. One of the logarithmic wind profiles has a horizontal inclination angle of 5 degrees, the other logarithmic wind profile flows directly towards the turbine. Each of the wind profiles was simulated for three inlet velocities: 4, 12 and 16 m/s, to observe the simulated model's behaviour compared to the actual turbine under similar conditions. The logarithmic wind profile with 12 m/s was tested on a reference turbine geometry from the DOWEC study project, as the simulations yielded results close to the design and the geometry, besides the blades, was kept simple. Two additional simulations with logarithmic wind profiles were conducted: in one the rotor is rotated to verify whether the spinner's geometry is rotationally symmetric; in the other the

blades were replaced by cylinders to assess the blades' influence on the  $k_1$ -factor.

To ensure that the simulations carried out are plausible, the general flow over the spinner was observed. The flow over the spinner appeared to develop as expected, although the velocities measured at the iSpin sensors appeared smaller than expected. Further, the simulated power output of the turbine was compared to the nominal power of the GE 2.5-120. This deviated strongly from the expected values, as of the 2.5 MW nominal power only up to 200 kW were simulated. The reason for this was found in the down scaled rotor blade, as the blade design and the positioning of the airfoils depend on the radius. Since the radius and the resulting airfoil angles did not match, the blade was not able to generate as much power as intended.

The low velocities in front of the spinner were investigated and their decrease from inlet to spinner was plotted. As the met mast data shows a similar decrease when compared, the general decrease is valid. The resulting curves differ in their development depending on their inlet velocity, whereby only the decrease in velocity for 4 m/s is unexpected. Further, an unexpected area of low wind speed was located over the iSpin's sensor path, which was investigated by checking the spinner's geometry for symmetry by rotating the blade and spinner. The simulation with the rotated blade showed a similar effect to the original simulation and therefore the low wind speed was concluded to be connected to the model's tilted rotational axis. When comparing the simulated velocities over the iSpin sensor path to the 10 Hz measurement against the rotational angle, it can be observed that both show significant variations in velocity over one rotation, this further verified the connection between the actual turbine and the simulation.

The ratio of simulated velocity to inlet velocity determines the  $k_1$ -factor. The  $k_1$ -factor for the GE 2.5-120 was 0.532. The average  $k_1$ -factor for the velocities of the logarithmic wind profile was  $0.436 \pm 0.013$ . The block profile simulations produced a factor of  $0.435 \pm 0.015$  and the logarithmic wind profile with inclination angle a factor of  $0.438 \pm 0.022$ . Therefore, the average  $k_1$ -factor over all cases and velocities was calculated at  $0.436 \pm 0.018$ .

The influence of the rotor blades was found to be small when compared to the influence of the spinner and blade root geometry. The  $k_1$ -factor simulated for the turbine geometry with the DOWEC blades at 12 m/s was 0.423 while the  $k_1$ -factor for the cylindrical blade was 0.442. The difference being relatively low with 4.49 % showed, that the blade design is less important than the spinners.

The difference between the simulated  $k_1$ -factor and the actually measured one may seem high and may seem to speak against the validity of using computational fluid dynamics for simulations replacing the conventional method via met mast. However, as discussed, some compromises were made in the creation of the geometry and during simulations. The influence of those trade-offs need to be investigated further in order to approach the point at which computational fluid dynamics becomes a viable and more economic option for evaluation the k-factors. The present thesis has presented a vital starting point in that direction.

## 7. Outlook

Although the k-factor estimated in this thesis varies significantly from the actual k-factor for the wind turbine and the process can still be improved, the results still show that the k-factor estimation for new turbine types can be done using CFD. However, in order to incorporate CFD into the calibration process, some adjustments need to be considered.

As the geometry creation via photogrammetry was a very lengthy process, it is advisable for other wind turbine types to find a quicker, more precise way of capturing and modelling their geometry. The method of photogrammetry used in this thesis might be a powerful tool under laboratory conditions, but if used for reflective surfaces on objects outdoors, other techniques should be preferred, as translating a 3D object to a 2D image with a normal camera will result in loss of depth perception. Other methods such as laser scanning should be considered, since they provide a higher resolution and can capture the geometry more completely and more precisely. Further, getting the correct format for the data is also crucial, as time must be invested to translate and adapt the data to fit the requirements of the CFD program.

One of the biggest limitations during this thesis may have been the use of the steady state model instead of a transient model, since some flow interdependencies cannot be simulated between the geometry's interfaces with a steady state model. Therefore, a transient run in which the geometry rotates should be conducted. This will allow visualizing the flow transitions between the steady and rotating interfaces better. Further a transient model would have made rotationally symmetry checks redundant and would have allowed following the iSpin sensor's measurements individually comparing each sensor to its corresponding 10 Hz sensor.

The wrong blade design was another drawback during this thesis, even though the influence of the blades' shape on the k-factor is small, a simulation with a blade design that fits the required radius and specifications for the turbine type could improve the accuracy of the results. As the blade's influence should then be the same as in the actual turbine, it would allow to determine the influences of the blade's pitch angle on the k-factor, which was not considered during this thesis. Further, a finer mesh should be used, as the mesh used in this thesis was very coarse. Mesh refinement should be investigated to eliminate possible interfering notches in the mesh.

Also, the simulated turbine in this thesis operated at 12.5 rpm for all wind velocities. For velocities between 3-6 m/s, the GE 2.5-120 should operate with 7.5 rpm. This would exclude the rotational velocity as a possible cause for errors, as the SCADA data and the simulation settings would be more in sync.

When comparing the actual  $k_1$ -factor with the simulated  $k_1$ -factor for the velocity in stationary frame, including all wind components, the very exact fit surprises. Therefore, another setup for the experiment could be thought of where the rotational axis is in plane with the x-axis of the coordinate frame, tilting the rest of the geometry. This should validate the velocities translated for the rotational axis.

Further, the effect of the openings in the spinner's surface have been neglected so far as well. Since the spinner's geometry has the biggest effect on the k-factor changing its geometry would also give more insights into the k-factors that can be expected for a spinner shape, which in turn can be used during calibration as a default value.

As this thesis only considered the  $k_1$ -factor, a set of simulations for the  $k_\alpha$ -value could be devised in which the turbine is yawed in and out of the incoming airflow several times. With the  $k_1$ - and  $k_\alpha$ -factors estimated, the  $k_2$ -factor could also be determined faster, further reducing the time needed for the calibration.

As previously stated, this thesis has presented a vital starting point in incorporating CFD in the k-factor calibration for spinner anemometers. And as CFD is also an iterative process, each iteration will bring new insights to improve the process, and therefore the results.

## 8. References

- [1] Figure taken from Inventor Fusion 360 during creating the geometry for this thesis
- [2] General Electric, GE 2.5 – 120, 2014, <https://www.en.wind-turbine-models.com/turbines/310-general-electric-ge-2.5-120> (25.11.2017)
- [3] LM Wind Power, LM 58.7, <https://www.lmwindpower.com/en/products-and-services/blade-types/2-comma-5-to-3-comma-3-mw> (25.11.2017)
- [4] T.F. Pedersen, H.A. Madsen, R. Møller, M. Courtney, N. sørensen, P. Envoldsen, P. Egedal, “Spinner Anemometry – An Innovative Wind Measurement Concept”, 2006, Risø, Wind Energy Department, Roskilde
- [5] A. Cuerva, A. sanz-Andrés, s. Franchini, P. Eecen, P. Busche, T.F. Pedersen, F. Mouzakis, "ACCUWIND, Accurate Wind Measurements in Wind Energy, Task 2, Improve the Accuracy of sonic Anemometers", EU-FP6 project report, June 2006
- [6] B. Tammelin, A. Heimo, M. Leroy, "Ice-free sensors - The EUMETNET sWS II project", Finnish Meteorological Institute, Helsinki
- [7] “Time of Flight theory”, Gill Instruments, (25.11.2017)  
<http://gillinstruments.com/products/anemometer/principleofoperation2.html/>
- [8] VDI 3786 Blatt 12 Entwurf, Verein Deutscher Ingenieure e.V. Düsseldorf, 2017
- [9] G. Demurtas, T.F. Pedersen, “New method to calibrate a spinner anemometer”, DTU Wind Energy, In Proceedings of EWEA 2014 European Wind Energy Association (EWEA), 2014
- [10] IEC 61400-12-2, Power performance of electricity producing wind turbines based on nacelle anemometry, Annex D – Nacelle wind speed transfer function measurement procedure, 2013
- [11] IEC 61400-12-1, Power performance measurements of electricity producing wind turbines, Chapter 5, 2005
- [12] Figures and pictures generated with Lidarview or from drone pictures during creating the geometry for this thesis
- [13] R. Kickingereder, Optische Vermessung partiell reflektierender Oberflächen, Universität Passau, Fakultät für Informatik und Mathematik, 11.2006
- [14] Script and Figures generated in MATLAB during creating the geometry for this thesis
- [15] Figure taken from ANSYS ICEM during creating the geometry for this thesis

- [16] H.J.Z. Kooilman, C.Lindenburg, D.Winkelaar, E.L. van der Hooft, „DOWEC 6 MW PRE-DESIGN, Aero-elastic modelling of the DOWEC 6 MW pre-design in PHATAS“, 09.2003, [https://www.ecn.nl/fileadmin/ecn/units/wind/docs/dowec/10046\\_009.pdf](https://www.ecn.nl/fileadmin/ecn/units/wind/docs/dowec/10046_009.pdf), 04.05.2017
- [17] R. schwarze, “CFD-Modellierung”, 2013, springer-Verlag Berlin Heidelberg, 2013
- [18] D. Ryan, J. Hofinger, “ANSYS ICEM CFD and ANSYS CFX Introductory Training Course”, <https://intranet.birmingham.ac.uk/collaboration/hpresearch/documents/public/cfd/CFD-intro-course-notes.pdf>, (04.12.2017)
- [19] “ANSYS CFX-Solver Modeling Guide”, Release 14.0, ANSYS, Inc., Canonsburg, 2011
- [20] R. Smith, “Moving Reference Frame for Computational Fluid Dynamics”, 24.06.2013, <http://www.symscape.com/blog/moving-reference-frame-for-cfd/>, (13.12.2017)
- [21] P. Mendis, T. Ngo, N. Haritos, A. Hira, B. Samali, J. Cheung, “Wind Loading on Tall Buildings”, EJSE special Issue: Loading on structures (2007)
- [22] Emeis s., Turk M. (2007) Comparison of Logarithmic Wind Profiles and Power Law Wind Profiles and their Applicability for Offshore Wind Profiles. In: Peinke J., Schaumann P., Barth s. (eds) Wind Energy. Springer, Berlin, Heidelberg”
- [23] 14.2.2, Boundary Details Tab, [https://www.sharcnet.ca/Software/Ansys/16.2.3/en-us/help/cfx\\_mod/CHDIGAAJ.html](https://www.sharcnet.ca/Software/Ansys/16.2.3/en-us/help/cfx_mod/CHDIGAAJ.html) (26.12.2017)
- [24] Installation Report of the Measurement System in the GE Wind Energy GmbH GE 2.5 – 120 [WT1] located at Offenbach an der Queich II
- [25] Figure or Table from Excel during post processing
- [26] Figure taken from CFD-Post during post processing for this thesis
- [27] H. Sigloch, Technische Fluidmechanik, Technik, Einsatz, Wirtschaftlichkeit, 10. Auflage, 2017, Springer Verlag
- [28] E. Hau, Windkraftanlagen Grundlagen, Technik, Einsatz, Wirtschaftlichkeit, 6. Auflage, 2016, Springer Verlag
- [29] 15.5.4 ave, Release 16.2, [https://www.sharcnet.ca/Software/Ansys/16.2.3/en-us/help/cfx\\_ref/i1308506.html](https://www.sharcnet.ca/Software/Ansys/16.2.3/en-us/help/cfx_ref/i1308506.html), (14.12.2017)

## 9. Appendix

### 9.1 MATLAB script for the Edge Transformation

```

%% Edge Definition

bild=rgb2gray(imread('F:\WP Offenbach a.d. Queich_GE2.5-120\Photography\DSC09238.JPG'));
edges = edge(bild, 'canny', 0.2);

bild = rgb2gray(imread('F:\WP Offenbach a.d. Queich_GE2.5-120\Photography\DSC09022bb.JPG'));
edgesfront = edge(bild, 'canny', 0.2);

edgesfront2=edgesfront(1:end,475:2650); % cutting of the unnecessary part
figure(1);
imagesc(edgesfront2);

edges2=edges(700:3000,1000:5000); % cutting of the unnecessary part
figure(2);
imagesc(edges2);

%% Reconfiguration of matrix

j=1;

while j<=4001
i=1;
while i<=2301

if edges2(i,j)==1
edges2trans(i,j)=i; %transformation of matrix edges to y-values
end
i=i+1;
end

j=j+1;
end

j=1;
while j<=2176
i=1;
while i<=2201

if edgesfront2(i,j)==1
edgesfront2trans(i,j)=i; %transformation of matrix edges to y-values
end
i=i+1;
end

j=j+1;
end

%% sorting of matrix into xy-coordinates

```

```

j=1;k=0;x=[];y=[];z=[];t=0; % index for sorting loop
while j<=4001
i=1;

while i<=2301

if edges2trans(i,j)>1

x=[x;edges2trans(i,j)];
y=[y;k];
z=[z;t];
end
i=i+1;

end
j=j+1;
k=k+1;

end

Res=[x,y,z];

dlmwrite('PNTS_EdgeTransform_Top.out',Res, ' ') % writing to ascii

j=1;k=0;x2=[];y2=[];z2=[];t=0; % index for sorting loop
while j<=2176
i=1;

while i<=2201

if edgesfront2trans(i,j)>1

x2=[x2;edgesfront2trans(i,j)];
y2=[y2;k];
z2=[z2;t];
end
i=i+1;

end
j=j+1;
k=k+1;

end

Res2=[x2,y2,z2];
dlmwrite('PNTS_EdgeTransform_Front.out',Res2, ' ') % writing to ascii

```

## 9.2 MATLAB script for the Point Cloud Transformation

```

%% Point Cloud Transformation

%% Input of XYZ-Files
XYZ=dlmread('romowind_w2_sorted.txt');

%% seperation of coordinates

xyz1=XYZ(1:end,4:end);

xyz2=XYZ(1:end,1:3);

%%
close all;
format long;

n=length(XYZ(1:end,1));
i=1;
x1=[];
y1=[];
z1=[];

while n>=i

    x1=[x1,xyz2(i,1)];
    y1=[y1,xyz2(i,2)];
    z1=[z1,xyz2(i,3)];

    i=i+10; %reducing number of points by 10
end

%Reducing number of points by 100
x=(x1)/100;
y=(y1)/100;
z=(z1)/100;

figure(1)
    subplot(1,3,1)
    plot3(x,y,z, '.');

%Coordinate Transformation
xt=(x*cos(40))+(y*sin(40));
yt=(-x*sin(40))+(y*cos(40));
zt=z;

figure(1)
    subplot(1,3,2)
    plot3(xt,yt,zt, '.');

t=length(xt);
j=1;

xx=[];
yx=[];
zx=[];

```

```

x_mean=mean(xt);
y_mean=mean(yt);
z_mean=mean(zt);

while t>=j
%removing points from plot not associated to Turbine, needs to be
%adjusted for other point clouds

    if xt(1,j)>=3.8054159e+04 && xt(1,j)<=3.8054185e+04 && yt(1,j)>=-3.99966e+04 && yt(1,j)<=-
    3.999645e+04 && zt(1,j)<=4.7500

        xx=[xx,x_mean-xt(1,j)];
        yx=[yx,y_mean-yt(1,j)];
        zx=[zx,z_mean-zt(1,j)];

    end

    j=j+1;
end

subplot(1,2,3)
plot3(xx,yx,zx,'.');

%% Writing .out-file / .txt-file

fid=fopen('ReducedPointcloud.txt','wt');
fprintf(fid, '%f %f %f \n\r', [x;y;z]);
fclose(fid);

fid2=fopen('PointCloudCoordinateTransformation.txt','wt');
fprintf(fid2, '%4.8f %4.8f %4.8f \n\r', [xt;yt;zt]);
fclose(fid2);

fid3=fopen('FormattedPointCloud.txt','wt');
fprintf(fid3, '%4.10d %4.10s %4.10s \n\r', [xx;yx;zx]);
fclose(fid3);

```

### 9.3 Ansys ICEM Global Mesh Setup

**Part Mesh Setup**

Part	Prism	Hexa-core	Maximum size	Height	Height ratio	Num layers	Tetra size ratio	Tetra width	Min size limit	Max deviation	Internal wall	Split wall
AIRFOIL_BODY	<input type="checkbox"/>	<input type="checkbox"/>										
BLADE/LEADING_EDGE/ADJ_DU_35	<input type="checkbox"/>	<input type="checkbox"/>	0.08	30	1.1	4	1.2	0	0	0		
BLADE/LEADING_EDGE/ADJ_DU_4050	<input type="checkbox"/>	<input type="checkbox"/>	0.08	30	1.1	4	1.2	0	0	0		
BLADE/LEADING_EDGE/BLADE_ROOTS	<input type="checkbox"/>	<input type="checkbox"/>	0.04	6	1.1	4	1.2	0	0	0		
BLADE/LEADING_EDGE/CYLINDER1	<input type="checkbox"/>	<input type="checkbox"/>	0.08	0	0	0	0	0	0	0		
BLADE/LEADING_EDGE/CYLINDER2BLAU	<input type="checkbox"/>	<input type="checkbox"/>	0.08	30	1.1	4	1.2	0	0	0		
BLADE/LEADING_EDGE/DU_91_W225C	<input type="checkbox"/>	<input type="checkbox"/>	0.08	30	1.1	4	1.2	0	0	0		
BLADE/LEADING_EDGE/DU_93_W210	<input type="checkbox"/>	<input type="checkbox"/>	0.08	30	1.1	4	1.2	0	0	0		
BLADE/LEADING_EDGE/DU_97_W300	<input type="checkbox"/>	<input type="checkbox"/>	0.08	30	1.1	4	1.2	0	0	0		
BLADE/LEADING_EDGE/NACA_64-618	<input type="checkbox"/>	<input type="checkbox"/>	0.08	30	1.1	4	1.2	0	0	0		
BLADE/LEADING_EDGE/TIP	<input type="checkbox"/>	<input type="checkbox"/>	0.08	30	1.1	4	1.2	0	0	0		
BLADE/TRAILING_EDGE/ADJ_DU_35	<input type="checkbox"/>	<input type="checkbox"/>	0.04	6	1.1	4	1.2	0	0	0		
BLADE/TRAILING_EDGE/ADJ_DU_405C	<input type="checkbox"/>	<input type="checkbox"/>	0.04	6	1.1	4	1.2	0	0	0		
BLADE/TRAILING_EDGE/CYLINDER2BLAU	<input type="checkbox"/>	<input type="checkbox"/>	0.04	6	1.1	4	1.2	0	0	0		
BLADE/TRAILING_EDGE/DU_91_W225C	<input type="checkbox"/>	<input type="checkbox"/>	0.04	6	1.1	4	1.2	0	0	0		
BLADE/TRAILING_EDGE/DU_93_W210	<input type="checkbox"/>	<input type="checkbox"/>	0.04	6	1.1	4	1.2	0	0	0		
BLADE/TRAILING_EDGE/DU_97_W300	<input type="checkbox"/>	<input type="checkbox"/>	0.04	6	1.1	4	1.2	0	0	0		
BLADE/TRAILING_EDGE/NACA_64-618	<input type="checkbox"/>	<input type="checkbox"/>	0.04	6	1.1	4	1.2	0	0	0		
BLADE/TRAILING_EDGE/TIP	<input type="checkbox"/>	<input type="checkbox"/>	0	0	0	0	1.2	0	0	0		
GEOM	<input type="checkbox"/>	<input type="checkbox"/>	0	0	0	0						
GEOM/GEOM.1	<input type="checkbox"/>	<input type="checkbox"/>	0	0	0	0						
GEOM/GEOM.1/GEOM.1	<input type="checkbox"/>	<input type="checkbox"/>	0	0	0	0						
GEOM/GEOM.1/MIDDLE	<input type="checkbox"/>	<input type="checkbox"/>										
GEOM/GEOM.1/STAGGER	<input type="checkbox"/>	<input type="checkbox"/>										
GEOM/INTERSECTION	<input type="checkbox"/>	<input type="checkbox"/>	0	30	1.1	4	1.2	0	0	0		
GEOM/PNTS	<input type="checkbox"/>	<input type="checkbox"/>										
GEOM/PNTS_ASM/PNTS	<input type="checkbox"/>	<input type="checkbox"/>										
GEOM/PNTS_ASM/PNTS_BLADE2	<input type="checkbox"/>	<input type="checkbox"/>										
GEOM/PNTS_ASM/PNTS_HOOKS	<input type="checkbox"/>	<input type="checkbox"/>										
GEOM/PNTS_ASM/PNTS_MOUNTING_BRAC	<input type="checkbox"/>	<input type="checkbox"/>										
GEOM/PNTS_ASM/PNTS_NACELLE	<input type="checkbox"/>	<input type="checkbox"/>										
GEOM/PNTS_ASM/PNTS_SPINNER	<input type="checkbox"/>	<input type="checkbox"/>										
GEOM/PNTS_ASM/PNTS_TOWER	<input type="checkbox"/>	<input type="checkbox"/>										
HUB/BLADE_CONNECTOR	<input type="checkbox"/>	<input type="checkbox"/>	0.08	6	1.1	4	1.2	0	0	0		
HUB/BLADE_FLATES	<input type="checkbox"/>	<input type="checkbox"/>	0.08	6	1.1	4	1.2	0	0	0		
HUB/SPIN_V3	<input type="checkbox"/>	<input type="checkbox"/>	0.005	6	1.1	4	1.2	0	0	0		
HUB/SPINNER2	<input type="checkbox"/>	<input type="checkbox"/>	0.01	6	1.1	4	1.2	0	0	0		
INTERFACES/CIRCUMFERENCE	<input type="checkbox"/>	<input type="checkbox"/>	1	30	1.1	4	1.2	0	0	0		
INTERFACES/IN	<input type="checkbox"/>	<input type="checkbox"/>	1	30	1.1	4	1.2	0	0	0		
INTERFACES/OUT	<input type="checkbox"/>	<input type="checkbox"/>	1	30	1.1	4	0	0	0	0		
SURROUNDING/BOTTOM	<input type="checkbox"/>	<input type="checkbox"/>	25	30	1.1	4	1.2	0	0	0		
SURROUNDING/INLET	<input type="checkbox"/>	<input type="checkbox"/>	25	30	1.1	4	1.2	0	0	0		
SURROUNDING/NACELLE	<input type="checkbox"/>	<input type="checkbox"/>	0.08	6	1.1	4	1.2	0	0	0		
SURROUNDING/OUTLET	<input type="checkbox"/>	<input type="checkbox"/>	25	30	1.1	4	1.2	0	0	0		
SURROUNDING/SIDES	<input type="checkbox"/>	<input type="checkbox"/>	25	30	1.1	4	1.2	0	0	0		
SURROUNDING/TOP	<input type="checkbox"/>	<input type="checkbox"/>	25	30	1.1	4	1.2	0	0	0		
SURROUNDING/TOWER	<input type="checkbox"/>	<input type="checkbox"/>	1	30	1.1	4	1.2	0	0	0		
SURROUNDING_BODY	<input type="checkbox"/>	<input type="checkbox"/>	0									

Show size params using scale factor  
 Apply inflation parameters to curves  
 Remove inflation parameters from curves  
 Highlighted parts have at least one blank field because not all entities in that part have identical parameters

Apply Dismiss

## 9.4 Global Mesh Parameters

The screenshot displays the 'Global Mesh Setup' dialog box, which is organized into several sections for configuring meshing parameters:

- Global Mesh Parameters (Top):** Includes 'Growth law' (exponential), 'Initial height' (0), 'Height ratio' (1.2), 'Number of layers' (3), and 'Total height' (0). It also features a 'Compute params' button and a 'Fix matching direction' checkbox.
- Prism Meshing Parameters (Middle-Left):** Contains 'Min prism quality' (0.008968688), 'Offset weight' (0.50), 'Fillet ratio' (0.1), 'Max prism angle' (180), 'Max height over base', and 'Prism height limit factor' (0). It includes 'Ratio multipliers' for 'New volume part', 'Side part', and 'Top part', and a 'Fix matching direction' checkbox.
- Volume Meshing Parameters (Middle-Right):** Shows 'Mesh Type' (Tetra/Mixed), 'Mesh Method' (Robust (Dcree)), and 'Edge extension' (0.07500003). It includes checkboxes for 'Run as batch process', 'Fast transition', 'Define thin cuts', 'Smooth mesh', 'Smooth neighbors' (5), 'Min quality' (0.4), 'Coarsen mesh', and 'Worst aspect ratio' (0.2). There are also checkboxes for 'Fix Non-manifold', 'Close Edges', 'Fix Holes', and 'Use active local coordinate system'.
- Global Mesh Size (Bottom-Left):** Includes 'Scale factor' (1), 'Global Element Scale Factor', 'Global Element Seed Size' (Max element: 4000), and 'Curvature/Proximally Based Refinement' (Enabled, Min size limit: 0.02, Elements in gap: 3, Refinement: 43, Ignore Wall Thickness).
- Global Mesh Setup (Bottom-Right):** Includes 'Scale factor' (1), 'Global Element Scale Factor', 'Global Element Seed Size' (Max element: 4000), and 'Curvature/Proximally Based Refinement' (Enabled, Min size limit: 0.02, Elements in gap: 3, Refinement: 43, Ignore Wall Thickness).
- Smoothing Options (Bottom):** Contains 'Number of surface smoothing steps' (5), 'Triangle quality type', 'Number of volume smoothing steps' (10), 'Max directional smoothing steps' (12), and 'First layer smoothing steps' (1). It also includes a 'Read a Prism Parameters File' button.

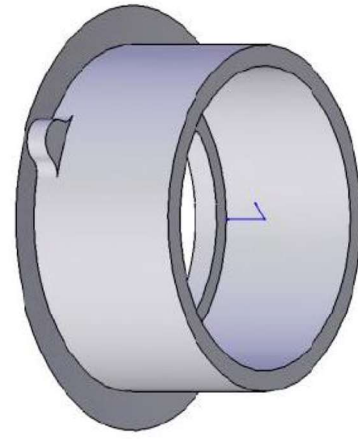
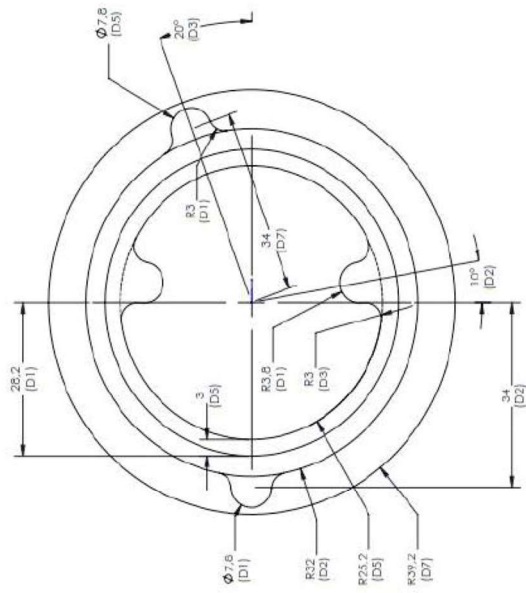
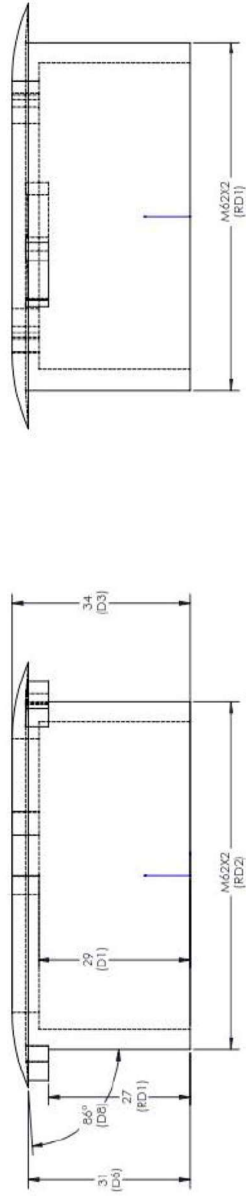
At the bottom of the dialog, there are 'Apply', 'OK', and 'Dismiss' buttons.

The displayed settings are for a finer mesh. The mesh used for the thesis can be achieved by setting the global element scale factor to

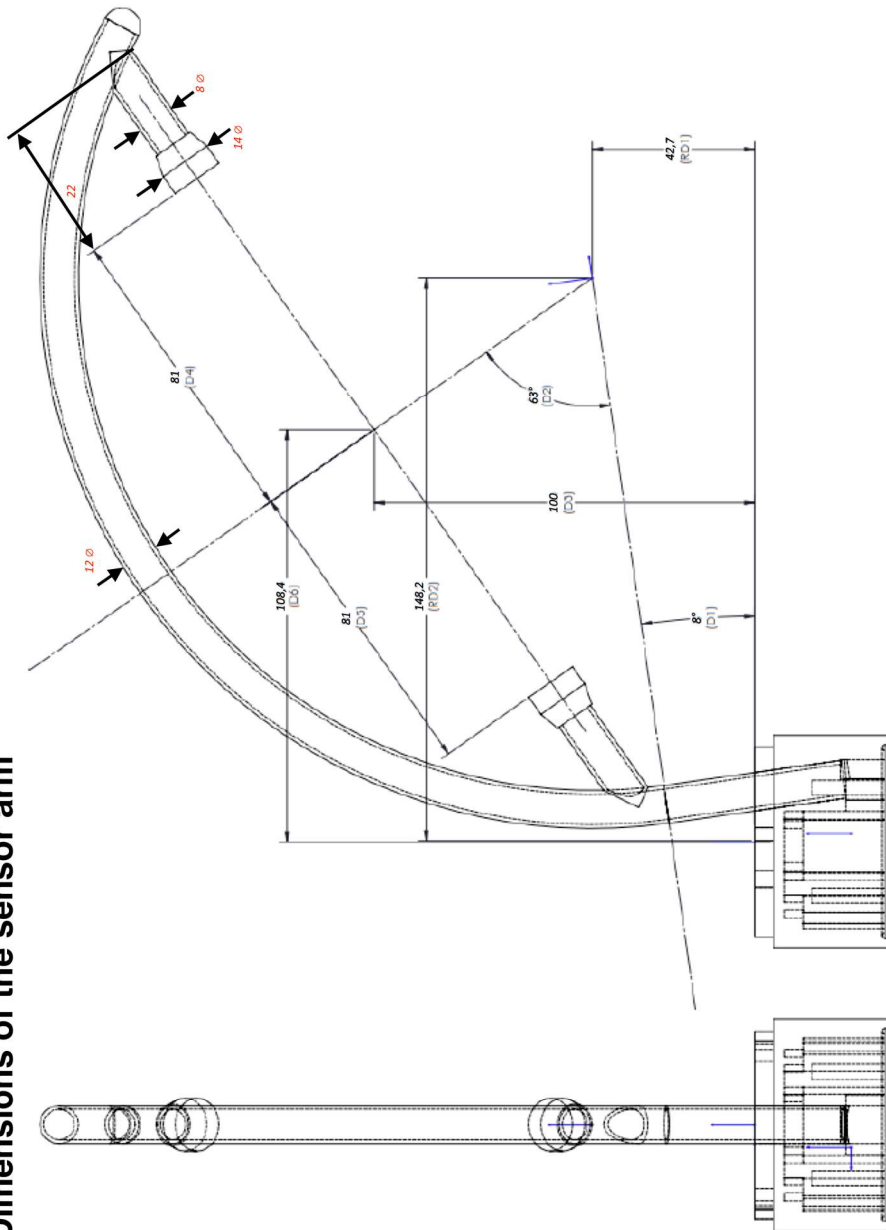
## 9.5 iSpin Dimensions for the Technical Drawing

**ROMO WIND** WIND KNOWLEDGE IS WIND POWER  
**iSpin v3**  
Dimensions of iSpin Components

**Dimensions of the bushing**



### Dimensions of the sensor arm



iSpin v3 Dimensions

*The values in red were added with the help of a calliper. The quality of the PDF didn't show the given dimensions properly, therefore the numbers are reprinted.*

## **Statutory Declaration**

I hereby declare that I am the author of the Master Thesis presented as applied for previously unassisted by others, using only the sources and references stated in the text.

Hamburg, den 27.12.2017

Luka Raulf